

**TRUCK CRASHWORTHINESS SIMULATION USING
ANSYS**



UNIVERSITI TEKNIKAL MALAYSIA MELAKA

**TRUCK CRASHWORTHINESS SIMULATION USING
ANSYS**

MOHD SHAZLI AMER

**A report submitted in partial fulfilment of the requirements for the degree of
Bachelor of Mechanical Engineering**



Faculty of Mechanical Engineering

UNIVERSITI TEKNIKAL MALAYSIA MELAKA

2022

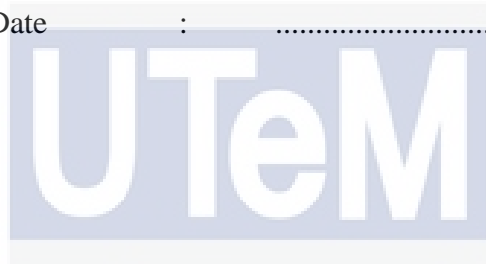
DECLARATION

I declare that this project report entitled “Truck Crashworthiness Simulation Using ANSYS”
is the result of my work except as cited in the references

Signature :

Name :

Date :



اونيورسيتي تيكنيكل مليسيا ملاك

UNIVERSITI TEKNIKAL MALAYSIA MELAKA

APPROVAL

I hereby declare that I have read this project report, and in my opinion, this report is sufficient in terms of scope and quality for the award of Bachelor of Mechanical Engineering.

Signature :

Name : *DR. SHAMSUL ANUAR
BIN SHAMSUDIN*

Date : *07-02-2022*



اونيورسيتي تيكنيكل مليسيا ملاك

UNIVERSITI TEKNIKAL MALAYSIA MELAKA

DEDICATION

My dissertation is dedicated to my family and lots of friends. An extraordinary sense of thanks goes out to my devoted parents, Sakka bin Matta and Raminah binti Kybe. Their words of support and prodding for persistence still ring in my ears. My siblings and friends have never left me and are exceptional.



ABSTRACT

Hundreds of people die in collisions between vehicles and large trucks each year. The greatest danger in the event of a collision between a car and a heavy vehicle is the invasion of the passengers' compartment under the heavy truck's rear underride, which might result in a fatal injury to passengers. The purpose of this paper is to examine, simulate, and analyse a Rear Under Run Protection (RUPD) system in a crashing state. The primary goal of creating the RUPD is to increase the vehicle's safety and occupants. This research aims to improve crashworthiness by creating a new rear underride protection device (RUPD) following FMVSS 223/224 rules. The material selection and structural design are the two primary determinants of impact energy absorption during a crash. This research focuses on the RUPD and the three factors that influence it: type of beam, angle of support, and material. Finite element simulation is utilised for performance analysis of the RUPD in ANSYS by static structural analysis and explicit dynamic analysis with different load distributions at various locations on the RUPD. The legal requirements for an RUPD are specified in regulation FMVSS 223/224 in the United States of America, CMVSS 223 in Canada, and ECE R 58 in Europe, which establishes stringent requirements for the device's design and behaviour under load that the device must meet in order to be approved for commercial vehicles. The results showed that the new RUPD design enhanced the energy absorption and was able to fulfil the standard requirement of crashworthiness.

UNIVERSITI TEKNIKAL MALAYSIA MELAKA

ABSTRAK

Beratus-ratus orang maut dalam pelanggaran antara kenderaan dan trak besar setiap tahun. Implikasi sekiranya berlaku pelanggaran antara kereta dan kenderaan berat ialah pencerobohan ruang penumpang di bawah bahagian bawah belakang trak berat, yang mungkin mengakibatkan kecederaan maut kepada penumpang. Tujuan kajian ini adalah untuk meneliti, mensimulasikan dan menganalisis sistem Rear Underrun Protection Device (RUPD) berdasarkan situasi pelanggaran. Matlamat utama mewujudkan RUPD adalah untuk meningkatkan keselamatan dan penghuni kenderaan. Penyelidikan ini bertujuan untuk mencipta peranti perlindungan (RUPD) baharu mengikut peraturan FMVSS 223/224 untuk meningkatkan kelayakan kemalangan. Pemilihan bahan dan reka bentuk struktur ialah dua penentu utama penyerapan tenaga hentaman semasa kemalangan. Penyelidikan ini memberi tumpuan kepada tiga faktor yang mempengaruhinya: jenis rasuk, sudut sokongan dan bahan. Simulasi digunakan untuk analisis prestasi RUPD dalam ANSYS oleh analisis struktur statik dan analisis dinamik eksplisit dengan beban yang berbeza-beza di pelbagai lokasi pada RUPD. Keperluan undang-undang untuk RUPD dinyatakan dalam peraturan FMVSS 223/224 di Amerika Syarikat, CMVSS 223 di Kanada dan ECE R 58 di Eropah, yang menetapkan keperluan ketat untuk reka bentuk dan tindak balas RUPD terhadap hentakan yang mesti dipenuhi oleh peranti untuk diluluskan bagi kenderaan komersial. Keputusan menunjukkan bahawa reka bentuk RUPD baharu telah meningkatkan penyerapan tenaga dan mampu memenuhi keperluan piawai pelanggaran.

UNIVERSITI TEKNIKAL MALAYSIA MELAKA

ACKNOWLEDGEMENTS

First, I want to express my gratitude and thankfulness to God, the Almighty, for His showers of blessings during my project work, which allowed me to finish the project successfully. I want to convey my profound gratitude to my research supervisor, Dr Shamsul Anuar Bin Shamsudin, Senior Lecturer in the Faculty of Mechanical at Universiti Teknikal Malaysia Melaka (UTeM) for allowing me to work on this project and offering vital advice during its completion. His vigour, vision, sincerity, and drive have all made a profound impression on me. He demonstrated how to perform the research and provide the data in the most straightforward manner possible. It was an incredible joy and honour to work and learn under his leadership. I owe him all he has given me. Additionally, I want to convey my appreciation for his friendship, compassion, and fantastic sense of humour.

Additionally, I want to express my deepest gratitude to my examiners, Ir. Dr Mohd Shukri Bin Yob and Dr Mohd Nizam Bin Sudin for their helpful comments and viewpoints on completing this study. I am grateful to my parents for their love, prayers, worry, and sacrifices in teaching and preparing me for the future. I owe a debt of gratitude to my family and friends for their love, understanding, prayers, and unwavering support as I work to accomplish this research endeavour.

Finally, I want to convey my appreciation to everyone who assisted me, directly or indirectly, in finishing the research job.

TABLE OF CONTENTS

CONTENTS	PAGE
ABSTRACT	i
ABSTRAK	ii
ACKNOWLEDGEMENTS	iii
TABLE OF CONTENTS	iv
LIST OF TABLES	vi
LIST OF FIGURES	vii
CHAPTER 1	
INTRODUCTION	1
1.1 Background	1
1.2 Problem Statement	5
1.3 Objectives	8
1.4 Scope of Project	8
CHAPTER 2	
LITERATURE REVIEW	10
2.1 Introduction of Under-ride Protection Device (UPD)	10
2.2 Rear Under-ride Protection Device (RUPD)	12
2.2.1 Design Regulation	12
2.2.2 Dimension of RUPD	13
2.2.3 Material Details and Element Criteria	16
2.2.4 Effect of support structure angle	17
2.2.5 Effect of the separation distance between support structures	18
2.2.6 Simulation Condition	20
CHAPTER 3	
METHODOLOGY	25
3.1 Overview of Methodology	25
3.2 Specification of Research	25
3.2.1 Type of Heavy Truck	25
3.2.2 Dimension of RUPD	27

3.2.3	Analysis Condition of RUPD	27
3.3	Flow Chart	28
3.3.1	Research study	29
3.3.2	Concept Design	29
3.3.3	Drawing using software CATIA	30
3.3.4	Material Selection	30
3.3.5	Analysis and Validation	30
3.3.6	Detail Drawing	31
3.4	Design Process	31
3.4.1	House of Quality	31
3.4.2	Morphological Chart	33
3.4.3	Design Concept	34
3.4.4	Concept Selection	34
3.4.5	Modelling of UPD	34
CHAPTER 4		
RESULTS AND DISCUSSION		35
4.0	Analysis of RUPD	35
4.1	Static Structural Analysis	35
4.1.1	Beams Impact Analysis	36
4.1.2	Angle of Support Analysis	67
4.1.3	Analysis Type of Beams Used for Support UPD	90
4.2	Explicit Dynamic Analysis	100
4.2.1	Analysis Material of UPD	100
4.2.2	Discussion on Material Analysis	105
4.3	Final Design	106
CHAPTER 5		
CONCLUSION AND RECOMMENDATION		108
5.1	Conclusion	108
5.2	Recommendations	109
REFERENCES		110
APPENDICES		116

LIST OF TABLES

TABLE	TITLE	PAGE
Table 1.1. 1	Disease burden (DALYs lost) for ten leading causes by (Smart Driving Research Center (SDRC))	2
Table 1.2. 1	Total motor vehicles involved in road accidents by type of vehicle, Malaysia 2009-2018	6
Table 1.2.1	Morphological Chart of RUPD	33
Table 4.1. 1	Type of forces on impact beams.	40
Table 4.1. 2	Static Structural Analysis Data for Types of Beams	62
Table 4.1. 3	Static Structural Analysis Data for Types of Beams	63
Table 4.1. 4	Data Analysis of Support Structure by Using Circular Hollow Beam	86
Table 4.1. 5	Data Analysis of Support Structure by Using W-Beam	86
Table 4.1. 6	Data Analysis of Support Structure by Using Rectangular Hollow Beam	87
Table 4.1. 7	Data Analysis of Support Structure by Using Square Hollow Beam	87
Table 4.1. 8	Comparison of total deformation type of beam used for RUPD	98
Table 4.1. 9	Comparison data of maximum stress von Mises for the type of beam used for RUPD	99
Table 4.1. 10	Comparison data of maximum stress von Mises for the type of beam used for RUPD	99

LIST OF FIGURES

TABLE	TITLE	PAGE
Figure 1.1. 1	Number of fatal road accidents and death involving HGV by Polis Diraja Malaysia 2016 Royal Malaysia Police Annual Report, 2016 (Kuala Lumpur, Malaysia: PDRM	3
Figure 1.1. 2	A protection device that is being studied.	5
Figure 1.2. 1	Rear impact without RnSUPD	7
Figure 1.2. 2	Side impact without RnSUPD	7
Figure 2.1. 1	Simulation rear impact without RUPD	11
Figure 2.1. 2	Distribution of points of impact	12
Figure 2.2. 1	Dimensional limit of an RUPD (49 CFR § 571.224 - Standard No. 224; Rear impact protection)	14
Figure 2.2. 2	Configuration requirements for underride guard (FMVSS 224).	14
Figure 2.2. 3	Design and Mountings of RUPD Model	15
Figure 2.2. 4	Rear views of the device (Belair, 2014).	16
Figure 2.2. 5	(a) Internal energy for 15, 30, 45, 60 degree, (b) Internal energy for 15, 20, 25, 30 degree.	18
Figure 2.2. 6	(a) Internal energy for 15, 30, 45, 60 degree, (b) Internal energy for 15, 20, 25, 30 degree.	18
Figure 2.2. 7	The distance between support structures of (a) legal separation (b) wide separation.	19
Figure 2.2. 8	Demonstrate RUPD Different Angle	19
Figure 2.2. 9	Strength test and energy absorption test locations (FMVSS 223).	21
Figure 2.2. 10	Indian Standard of RUPD (IS 14812-2005)	23
Figure 2.2. 11	Loading Device Mechanisms	24
Figure 3.2. 1	FUSO 16 000kg trucks.	26

Figure 3.2. 2	Dimension FUSO truck.	26
Figure 3.2. 3	Dimension of RUPD based on the FUSO truck.	27
Figure 3.3. 1	Flow Chart of Project	29
Figure 3.4. 1	House of Quality	32
Figure 4.0. 1	Condition of simulation RUPD (a) Material properties (b) Impact loading condition	35
Figure 4.1. 1	Condition of Analysis of Impact Beam	40
Figure 4.1. 2	Cylindrical hollow beam properties	41
Figure 4.1. 3	FBD for P1 at Cylindrical Hollow Beam	42
Figure 4.1. 4	FBD for P2 at Cylindrical Hollow Beam	43
Figure 4.1. 5	FBD for P3 at Cylindrical Hollow Beam	45
Figure 4.1. 6	Properties of Rectangular Hollow Beam	47
Figure 4.1. 7	FBD for P1 at Rectangular Hollow Beam	48
Figure 4.1. 8	FBD for P2 at Rectangular Hollow Beam	49
Figure 4.1. 9	FBD for P3 at Rectangular Hollow Beam	51
Figure 4.1. 10	Properties of Square Hollow Beam	52
Figure 4.1. 11	FBD for P1 at Square Hollow Beam	53
Figure 4.1. 12	FBD for P2 at Square Hollow Beam	54
Figure 4.1. 13	FBD for P3 at Square Hollow Beam	56
Figure 4.1. 14	Properties of W-Beam	57
Figure 4.1. 15	FBD for P1 at W-Beam	58
Figure 4.1. 16	FBD for P2 at W-Beam	59
Figure 4.1. 17	FBD for P3 at W-Beam	61
Figure 4.1. 18	Graph Comparison ANSYS and Manual Stress Von Mises of Cylindrical Hollow Beam	63
Figure 4.1. 19	Graph Comparison ANSYS and Manual Stress Von Mises of Rectangular Hollow Beam	64
Figure 4.1. 20	Comparison ANSYS and Manual Stress Von Mises of Square Hollow Beam	64
Figure 4.1. 21	Graph Comparison ANSYS and Manual Stress Von Mises of W-shaped Beam	65
Figure 4.1. 22	Graph Comparison Manual Stress Von Mises of Four Types of Beams	65

Figure 4.1. 23	Graph Comparison ANSYS Von Mises of Four Types of Beams	66
Figure 4.1. 24	Graph Comparison Total deformation of ANSYS for Four Types of Beams	66
Figure 4.1. 25	Analysis P1 of Circular beam with 15-degree angles (a) Total Deformation (b) Maximum Stress Von Mises (c) Strain Energy (d) Factor of Safety	68
Figure 4.1. 26	Analysis P2 of Circular beam with 15-degree angles (a) Total Deformation (b) Maximum Stress Von Mises (c) Strain Energy (d) Factor of Safety	68
Figure 4.1. 27	Analysis P3 of Circular beam with 15-degree angle (a) Total Deformation (b) Maximum Stress Von Mises (c) Strain Energy (d) Factor of Safety	69
Figure 4.1. 28	Analysis P1 of Circular beam with 25-degree angles (a) Total Deformation (b) Maximum Stress Von Mises (c) Strain Energy (d) Factor of Safety	69
Figure 4.1. 29	Analysis P2 of Circular beam with 25-degree angle (a) Total Deformation (b) Maximum Stress Von Mises (c) Strain Energy (d) Factor of Safety	70
Figure 4.1. 30	Analysis P3 of Circular beam with 25-degree angle (a) Total Deformation (b) Maximum Stress Von Mises (c) Strain Energy (d) Factor of Safety	70
Figure 4.1. 31	Analysis P1 of Circular beam with 45-degree angle (a) Total Deformation (b) Maximum Stress Von Mises (c) Strain Energy (d) Factor of Safety	71
Figure 4.1. 32	Analysis P2 of Circular beam with 45-degree angle (a) Total Deformation (b) Maximum Stress Von Mises (c) Strain Energy (d) Factor of Safety	71
Figure 4.1. 33	Analysis P3 of Circular beam with 45-degree angle (a) Total Deformation (b) Maximum Stress Von Mises (c) Strain Energy (d) Factor of Safety	72
Figure 4.1. 34	Analysis P1 of W-beam with 15-degree angle (a) Total Deformation (b) Maximum Stress Von Mises (c) Strain Energy (d) Factor of Safety	72

Figure 4.1. 35	Analysis P2 of W-beam with 15-degree angle (a) Total Deformation (b) Maximum Stress Von Mises (c) Strain Energy (d) Factor of Safety	73
Figure 4.1. 36	Analysis P3 of W-beam with 15-degree angle (a) Total Deformation (b) Maximum Stress Von Mises (c) Strain Energy (d) Factor of Safety	73
Figure 4.1. 37	Analysis P1 of W-beam with 25-degree angle (a) Total Deformation (b) Maximum Stress Von Mises (c) Strain Energy (d) Factor of Safety	74
Figure 4.1. 38	Analysis P2 of W-beam with 25-degree angle (a) Total Deformation (b) Maximum Stress Von Mises (c) Strain Energy (d) Factor of Safety	74
Figure 4.1. 39	Analysis P3 of W-beam with 25-degree angle (a) Total Deformation (b) Maximum Stress Von Mises (c) Strain Energy (d) Factor of Safety	75
Figure 4.1. 40	Analysis P1 of W-beam with 45-degree angle (a) Total Deformation (b) Maximum Stress Von Mises (c) Strain Energy (d) Factor of Safety	75
Figure 4.1. 41	Analysis P2 of W-beam with 45-degree angle (a) Total Deformation (b) Maximum Stress Von Mises (c) Strain Energy (d) Factor of Safety	76
Figure 4.1. 42	Analysis P3 of W-beam with 45-degree angle (a) Total Deformation (b) Maximum Stress Von Mises (c) Strain Energy (d) Factor of Safety	76
Figure 4.1. 43	Analysis P1 of Rectangular Hollow beam with 15-degree angle (a) Total Deformation (b) Maximum Stress Von Mises (c) Strain Energy (d) Factor of Safety	77
Figure 4.1. 44	Analysis P2 of Rectangular Hollow beam with 15-degree angle (a) Total Deformation (b) Maximum Stress Von Mises (c) Strain Energy (d) Factor of Safety	77
Figure 4.1. 45	Analysis P3 of Rectangular Hollow beam with 15-degree angle (a) Total Deformation (b) Maximum Stress Von Mises (c) Strain Energy (d) Factor of Safety	78

Figure 4.1. 46	Analysis P1 of Rectangular Hollow beam with 25-degree angle (a) Total Deformation (b) Maximum Stress Von Mises (c) Strain Energy (d) Factor of Safety	78
Figure 4.1. 47	Analysis P2 of Rectangular Hollow beam with 25-degree angle (a) Total Deformation (b) Maximum Stress Von Mises (c) Strain Energy (d) Factor of Safety	79
Figure 4.1. 48	Analysis P3 of Rectangular Hollow beam with 25-degree angle (a) Total Deformation (b) Maximum Stress Von Mises (c) Strain Energy (d) Factor of Safety	79
Figure 4.1. 49	Analysis P1 of Rectangular Hollow beam with 45-degree angle (a) Total Deformation (b) Maximum Stress Von Mises (c) Strain Energy (d) Factor of Safety	80
Figure 4.1. 50	Analysis P2 of Rectangular Hollow beam with 45-degree angle (a) Total Deformation (b) Maximum Stress Von Mises (c) Strain Energy (d) Factor of Safety	80
Figure 4.1. 51	Analysis P3 of Rectangular Hollow beam with 45-degree angle (a) Total Deformation (b) Maximum Stress Von Mises (c) Strain Energy (d) Factor of Safety	81
Figure 4.1. 52	Analysis P1 of Square Hollow beam with 15-degree angle (a) Total Deformation (b) Maximum Stress Von Mises (c) Strain Energy (d) Factor of Safety	81
Figure 4.1. 53	Analysis P2 of Square Hollow beam with 15-degree angle (a) Total Deformation (b) Maximum Stress Von Mises (c) Strain Energy (d) Factor of Safety	82
Figure 4.1. 54	Analysis P3 of Square Hollow beam with 15-degree angle (a) Total Deformation (b) Maximum Stress Von Mises (c) Strain Energy (d) Factor of Safety	82
Figure 4.1. 55	Analysis P1 of Square Hollow beam with 25-degree angle (a) Total Deformation (b) Maximum Stress Von Mises (c) Strain Energy (d) Factor of Safety	83
Figure 4.1. 56	Analysis P2 of Square Hollow beam with 25-degree angle (a) Total Deformation (b) Maximum Stress Von Mises (c) Strain Energy (d) Factor of Safety	83

Figure 4.1. 57	Analysis P3 of Square Hollow beam with 25-degree angle (a) Total Deformation (b) Maximum Stress Von Mises (c) Strain Energy (d) Factor of Safety	84
Figure 4.1. 58	Analysis P1 of Square Hollow beam with 45-degree angle (a) Total Deformation (b) Maximum Stress Von Mises (c) Strain Energy (d) Factor of Safety	84
Figure 4.1. 59	Analysis P2 of Square Hollow beam with 45-degree angle (a) Total Deformation (b) Maximum Stress Von Mises (c) Strain Energy (d) Factor of Safety	85
Figure 4.1. 60	Analysis P3 of Square Hollow beam with 45-degree angle (a) Total Deformation (b) Maximum Stress Von Mises (c) Strain Energy (d) Factor of Safety	85
Figure 4.1. 61	Graph comparison total deformation vs angle of the support structure by using (a) Circular Hollow Beam (b) W-Beam (c) Rectangular Hollow Beam (d) Square Hollow Beam	88
Figure 4.1. 62	Graph comparison strain energy vs angle of the support structure by using (a) Circular Hollow Beam (b) W-Beam (c) Rectangular Hollow Beam (d) Square Hollow Beam	89
Figure 4.1. 63	Support structure using circular hollow beam	90
Figure 4.1. 64	P1 analysis angle of support structure using the circular hollow beam.	91
Figure 4.1. 65	P2 analysis angle of support structure using the circular hollow beam.	91
Figure 4.1. 66	P3 analysis angle of support structure using the circular hollow beam.	92
Figure 4.1. 67	Support structure using W-beam.	92
Figure 4.1. 68	P1 analysis angle of support structure using W-beam.	93
Figure 4.1. 69	P2 analysis angle of support structure using W-beam.	93
Figure 4.1. 70	P3 analysis angle of support structure using W-beam	94
Figure 4.1. 71	Support structure using the rectangular hollow beam.	94
Figure 4.1. 72	P1 analysis angle of support structure using the rectangular hollow beam.	95

Figure 4.1. 73	P2 analysis angle of support structure using the rectangular hollow beam.	95
Figure 4.1. 74	P3 analysis angle of support structure using the rectangular hollow beam.	96
Figure 4.1. 75	Support structure using the square hollow beam.	96
Figure 4.1. 76	P1 analysis angle of support structure using the square hollow beam.	97
Figure 4.1. 77	P2 analysis angle of support structure using the square hollow beam.	97
Figure 4.1. 78	P3 analysis angle of support structure using the square hollow beam.	98
Figure 4.1. 79	Graph comparison of total deformation vs force for type of beam used for RUPD.	98
Figure 4.1. 80	Graph comparison of stress von Mises vs force for type of beam used for RUPD.	99
Figure 4.1. 81	Graph comparison of strain energy vs force for type of beam used for RUPD.	99
Figure 4.2. 1	Condition of RUPD for explicit dynamic analysis.	101
Figure 4.2. 2	Analysis results of RUPD for steel material (a) Total Deformation (b) Directional Deformation (c) Equivalent Elastic Strain (d) Equivalent Stress (e) Energy Conservation (f) Energy Summary	102
Figure 4.2. 3	Analysis results of RUPD for aluminium material (a) Total Deformation (b) Directional Deformation (c) Equivalent Elastic Strain (d) Equivalent Stress (e) Energy Conservation (f) Energy Summary	103
Figure 4.2. 4	Analysis results of RUPD for magnesium material (a) Total Deformation (b) Directional Deformation (c) Equivalent Elastic Strain (d) Equivalent Stress (e) Energy Conservation (f) Energy Summary	104
Figure 4.2. 5	Analysis results of RUPD for polyethylene material (a) Total Deformation (b) Directional Deformation (c) Equivalent Elastic	105

Strain (d) Equivalent Stress (e) Energy Conservation (f) Energy
Summary

Figure 4.3. 1	Final Design of RUPD Structure	107
Figure 4.3. 2	Final Design of RUPD Structure on Lorry	107



LIST OF ABBREVIATION

FMVSS	Federal Motor Vehicle Safety Standards
CMVSS	Canada Motor Vehicle Safety Standard
ECE	Economic Commission for Europe of the United Nations
UTeM	Universiti Teknikal Malaysia Melaka
DALYs	Disability-Adjusted Life Years
SDRC	Smart Driving Research Center
HGV	Heavy Good Vehicles
RTA	Roads and Transport Authority
WHO	World Health Organization
DOSM	Department of Statistic, Malaysia
HVNL	Heavy Vehicle National Law
GVM	Gross Vehicle Mass
ATM	Aggregate Trailer Mass
PDRM	Polis Diraja Malaysia
EMR	Eastern Mediterranean Region
RnSUPD	Rear and Side Underride Protection Device
RUPD	Rear Underride Protection Device
UPD	Underride Protection Device
CAD	Computer-Aided Design
HOQ	House Of Quality
FBD	Free Body Diagram
P1	Force at Point 1
P2	Force at Point 2
P3	Force at Pointe 3

LIST OF SYMBOL

σ_x	=	Stress x-direction (Pa)
σ_y	=	Stress y-direction (Pa)
σ_{ave}	=	Stress Average (Pa)
P	=	Force (N)
A	=	Area (m ²)
M	=	Moment (Nm)
I	=	First Moment of Inertia (m ³)
τ_{xy}	=	Shear stress xy plane (Pa)
τ_{max}	=	Shear stress maximum (Pa)
R	=	Radius Mohr's Circle (Pa)
V	=	Shear Force (Pa)
Q	=	The First Moment of the Portion of the Area (m ²)
t	=	Thickness (m)
F.S.	=	Factor of Safety
S_{ut}	=	Ultimate Tensile Strength (Pa)
C	=	Radius (m)
σ'	=	Maximum Stress Von Mises (Pa)
δ_T	=	Total Deformation (m)
U	=	Strain Energy (J)

CHAPTER 1

INTRODUCTION

1.1 Background

Among all traffic accidents, road traffic accidents take the most lives and are the most severe issue worldwide. The number of people killed in traffic collisions worldwide has increased dramatically (RTA), with 1.24 million deaths predicted each year. Road traffic fatalities are the leading cause of death for young people and the eighth leading cause of death worldwide (Elvik, 2013; Kaygisiz et al., 2015). Developing countries account for roughly 85% of all deaths. Males, especially those between the ages of 15 and 44, are disproportionately affected by traffic accidents. Countries spend 1 to 2 per cent of their gross national product on traffic incidents (Elvik, 2013). Although developing countries account for only 52 per cent of all vehicles on the road, they are responsible for 80% of all traffic fatalities. (WHO, 2013). In reality, as shown in Table 1.1.1, road traffic Disability-Adjusted Life Years (DALYs) loss will change from the ninth essential cause of DALYs in 1999 to the third necessary cause by 2020, as predicted by the WHO (Mohammed et al., 2019).

Table 1.1. 1: Disease burden (DALYs lost) for ten leading causes by (Smart Driving Research Center (SDRC)).

S.No	1998 Disease or Injury	2020 Disease or Injury
1	Lower respiratory contaminations	Ischaemic heart disease
2	HIV/AIDS	Unipolar major depression
3	Perinatal conditions	Road traffic injuries
4	Diarrhoeal diseases	Cerebrovascular disease
5	Unipolar major depression	Chronic obstructive pulmonary disease
6	Ischaemic heart disease	Lower respiratory infections
7	Cerebrovascular disease	Tuberculosis
8	Malaria	War
9	Road traffic injuries	Diarrheal diseases
10	Chronic obstructive pulmonary disease	HIV/AIDS

According to the Department of Statistics, Malaysia (DOSM), in 2018, new registrations of motor vehicles increased by 8.2% to 1,218,662 compared to 1,125,900 in 2017. Public transportation (48.0%), commercial vehicles (15.3%), and motorcycles (15.3%) all contributed to the rise (11.5 per cent). This study will be focused on commercial vehicles crash with a heavy vehicle type. A heavy vehicle is defined by the Heavy Vehicle National Law (HVNL) as one that has a gross vehicle mass (GVM) or aggregate trailer mass (ATM) of greater than 4.5 tonnes. Heavy vehicles include semi-trailers, B-double freight trucks, road trains, commuter buses, vehicle carriers, livestock and agricultural equipment, mobile cranes, and other specialised vehicles. By comparison, heavy goods vehicles (HGVs) are huge trucks used to transport products across the land. In Malaysia, HGVs are classified as trailers (articulated lorries), rigid lorries (two or more axles with a gross weight higher than 2.5 tonnes), and tiny trucks (2 axles small lorry or pick-up with gross weight less than 2.5 tonnes).

The Malaysian HGV fleet consists of nearly a million units (data from 2016), covering a total of 200 kilometres of travel per day and an average annual VKT (AAKT) of about 70,000 kilometres (Jamaluddin et al., 2021). The distance travelled by HGV is

expected to increase with the growth of Malaysia’s e-commerce industry. In Malaysia, the evolution of HGV incidents has shown a consistent up-and-down pattern. Figure 1.1.1 (sources of Polis Diraja Malaysia 2016 Royal Malaysia Police Annual Report, 2016 (Kuala Lumpur, Malaysia: PDRM) depicts the five-year way of HGV-related road accidents in Malaysia. Even though HGVs account for a small percentage of traffic, accidents involving HGVs result in over 1000 deaths per year in Malaysia. The involvement of an HGV in an accident is responsible for more than 80% of second-vehicle fatalities. It demonstrates that HGV accidents significantly affect other road users’ welfare (Hamidun et al., 2019).

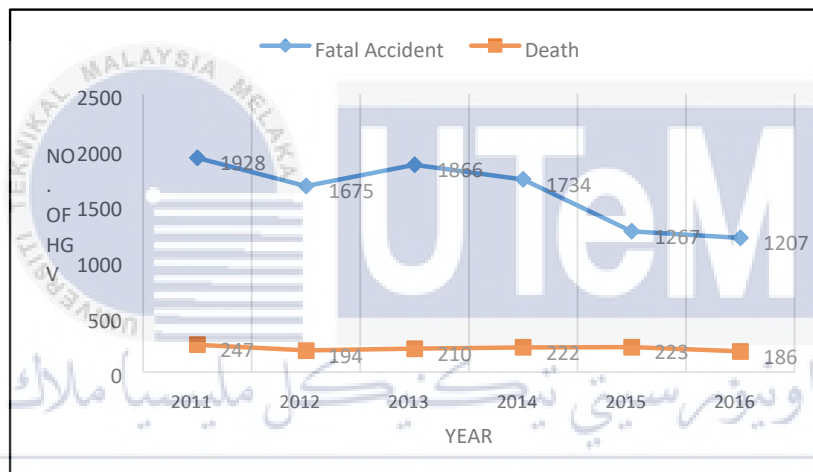


Figure 1.1. 1: Number of fatal road accidents and death involving HGV by Polis Diraja Malaysia 2016 Royal Malaysia Police Annual Report, 2016 (Kuala Lumpur, Malaysia: PDRM).

Over a year, medico-legal autopsies were done on 950 instances of fatal road traffic accidents at the SRN Hospital, MLN Medical College, Allahabad. The male to female ratio was 3:1, and 33.68 per cent of patients were between the ages of 25 and 44 (Kual et al., 2005). The most vulnerable were pedestrians, who accounted for 35.79 per cent of all deaths, followed by motorised two-wheelers, which accounted for 30.53 per cent. Heavy vehicles were found to be involved in 58.52 per cent of incidents, with highways accounting for 83.05 per cent of all collisions. In most cases, multiple injuries were suffered for heavy vehicles.

Heavy vehicles (trucks, oil tankers, buses and more) are more often involved in fatal RTAs than light vehicles (taxi, car, jeep, van and more) due to their higher speeds, more significant momentum, the availability of single-lane highways, overtaking, traffic volume, and others (Kual et al., 2005).

HGV accidents killed 4,500 people in Europe in 2013, accounting for around 18% of all road fatalities (*THE INJURY CHART BOOK A Graphical Overview of the Global Burden of Injuries Department of Injuries and Violence Prevention Noncommunicable Diseases and Mental Health Cluster WHO*, 2002). In Sweden, HGV-related road accident fatalities have also become a problem, as they account for half of all car occupant deaths (Odero et al., 1997). In terms of fatality risk, a study conducted by Buddhavarapu, Banerjee, and Prozzi (2013) found that locations with a higher percentage of truck traffic have a higher risk of fatal accidents. These HGVs' broad dimensions and mass significantly contribute to their collisions with other vehicles involved in road accidents (WHO, 2002). Since HGVs often travel at lower speeds than other vehicles, the speed differential can result in rear-end collisions (Jacobs & Astrop, 1999). Due to their large size, HGVs have operational disadvantages such as large blind spots, long stopping distances, and restricted manoeuvrability, necessitating extra caution from other vehicles.

Due to the high number of HGVs involved in fatal accidents, there is a pressing need to understand better how this vehicle category affects other road users. The bottom of a truck is higher than the car's bumper due to the truck's design. As a result, there is little for the car's bumper to crash with, and the windshield becomes the first point of contact. The vehicle collides with the truck, striking the windscreen and crashing into the passenger compartment. Heavy cars are responsible for the most significant number of fatalities. Changes in heavy vehicles' design and safety features are needed to prevent this from worsening. In this scenario, a safety under-ride guard must be designed. The basic concept behind an under-

ride guard for heavy vehicles is to prevent small passenger cars from passing underneath them. As a result, this research aims is to create a design and simulation analysis for the rear underside of an HGV to reduce the impact of a collision. The findings of this study will help safety planners prepare HGV transport safety equipment.



Figure 1.1. 2: Protection device that is being studied.

1.2 Problem Statement

Due to a developing pattern of freight road traffic, over a thousand fatal incidents involving heavy goods trucks (HGV) occur in Malaysia every year. More than 80% of fatal collisions involving HGVs resulted in the death of other road users. This condition necessitates a greater understanding of the accident characteristics of this vehicle class. This research examined the factors associated with HGV incidents that resulted in casualties using five years of historical accident data from 2011 to 2015. According to the binary logistic regression results, smaller vehicles have a substantially higher risk of a fatal outcome. Compared to the bus, the fatality odds ratios for cars, motorcycles, and bicycles are 1.929, 2.423, and 3.626, respectively. The straight road is more likely to become deadly in an HGV

collision than the T/Y junction or others (interchange & roundabout). Compared to other road hierarchies, accidents involving HGVs on expressways had higher chances.

Table 1.2. 1: Total motor vehicles involved in road accidents by type of vehicle, Malaysia 2009-2018.

TAHUN Year	MOTOSIKAL Motorcycle	MOTOKAR Motocar	VAN Van	BAS Bus	LORI Lorry	PEMACU 4 RODA Four Wheel Drive	TEKSI Taxi	BASIKAL Bicycle	LAIN-LAIN Others	JUMLAH Total
2009	113,962	472,307	19,220	9,380	46,724	23,581	8,669	2,486	9,294	705,623
2010	120,156	511,861	18,788	9,580	50,438	25,777	9,899	2,178	11,756	760,433
2011	129,017	546,702	17,916	9,986	53,078	30,828	11,197	2,033	16,394	817,151
2012	130,080	655,813	15,143	10,617	42,158	32,891	11,680	1,310	21,540	921,232
2013	121,700	632,602	17,148	10,123	39,276	52,512	11,651	1,370	15,441	901,823
2014	125,712	617,578	15,041	9,193	37,481	41,464	10,856	1,275	27,743	886,343
2015	123,408	625,758	14,565	8,804	34,942	46,163	9,591	1,119	29,924	894,274
2016	135,181	670,935	14,470	9,462	35,064	48,907	8,399	1,318	36,833	960,569
2017	108,221	564,491	13,347	7,258	34,747	44,297	5,328	787	24,047	802,523
2018	113,288	591,399	17,226	7,328	36,915	45,757	3,912	727	21,143	837,695

SUMBER: JABATAN SIASATAN DAN PENGUATKUASAAN TRAFIK BUKIT AMAN
Source: Bukit Aman Traffic Investigation and Enforcement Department

Suppose a car collides with another vehicle, a pedestrian, an animal, a road barrier, or any stationary obstacle such as a tree or a utility pole. In that case, it is called a traffic accident. Injury, death, automobile loss, and possession damage are possible outcomes of traffic collisions. Motor vehicle crashes result in death, injury, and financial hardship. Traffic collisions result in several casualties, including human life, property damage, and resource loss. Indeed, in countries where conflict is a factor, such as Afghanistan, Libya, Pakistan, and Yemen, road traffic accidents are the leading cause of fatal injuries, accounting for two to eight times as many deaths as war and lawful mediation. According to the World Health Organization (WHO), the Eastern Mediterranean Region (EMR) has the second-highest rate of traffic fatalities worldwide, after the African region, and includes a few other countries in the area.

When a small passenger vehicle passes under a heavy goods vehicle from the front, rear, or side, this is known as underride. During such collisions, the small vehicle's passenger

compartment collides with the heavy vehicle's chassis, causing severe injury to the passengers of the smaller vehicle. Front, back, and side underride accidents are the three forms of underride accidents. A heavy goods vehicle must be equipped with an underrun system that protects the occupant of the small vehicle from fatal injury to avoid such collisions. Without the RnSUPD (Rear and Side Under-Run Protection Device), all energy will be concentrated on the car's foundations, which will not withstand the impact. Figure 1.2.1 and Figure 1.2.2 depicts the damage to a small passenger vehicle caused by a rear and side underride collision. The whole vehicle has gone underneath the truck, and the car's entire frame has crumbled because of the sudden impact load.



Figure 1.2. 1: Rear impact without RnSUPD.



Figure 1.2. 2: Side impact without RnSUPD.

The figure above clearly shows that in a collision without the RnSUPD, the truck's effect is on the passenger compartment due to the car underrunning the car. A high-energy

crash would result in more casualties since there is not enough energy absorption until the vehicle collides with the passenger seat. However, in the next instance, RnSUPD, energy absorption occurs in the car's bonnet before the effect occurs in the passenger compartment. As a result, there are fewer deaths in this situation. Energy-absorbing front, back, and side under-run safety has been estimated to minimise casualties in car-lorry collisions by around 12% (Joseph et al., 2013).

1.3 Objectives

The following are the project's objectives:

- 1.3.1 To design underrun safety devices at the rear for heavy vehicles that fulfil the standard requirement of the regulation.
- 1.3.2 This research aimed to see how the rear under-run protection devices of heavy vehicles affected the design in three factors: beam types, angle of support, and material of underrun when force was applied by observing the deformation and energy absorption.
- 1.3.3 To validate the shape of data analysis of underrun by using manual calculation or comparison shape of data from other resources.

1.4 Scope of Project

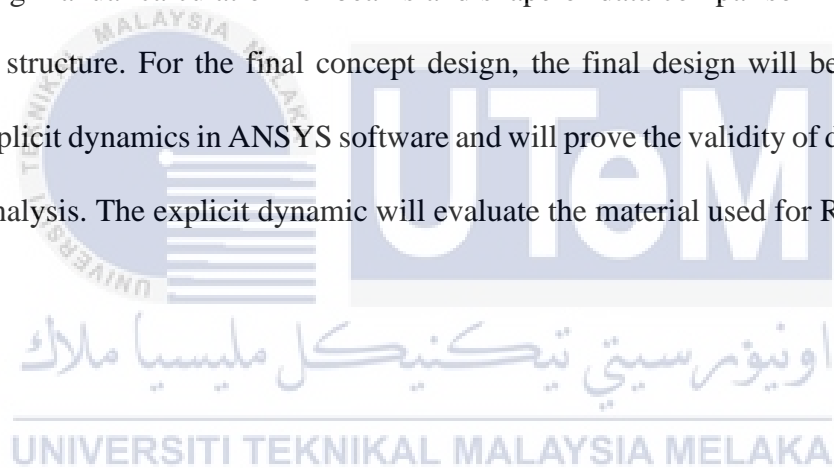
The following are the scope of the project:

- 1.4.1 The concept design of RUPD is built by using CATIA V5R21 software.
- 1.4.2 The design will be evaluated using ANSYS software using static structural analysis and explicit dynamic to gain the final concept design.

1.4.3 ANSYS 16.1 software is used to perform a finite element analysis and crashworthiness simulation.

1.4.4 Data will be validated using manual calculation or comparing data and explicit dynamics.

The project's scope will outline the subjects that will be discussed. First, this project examines the concept design of an RUPD to prevent cars or motorcycles from underride accident impact. CATIA V5R21 will be used for the CAD and analysed using static structural in ANSYS for this section. The shape of the design concept data will be evaluated by comparing manual calculation for beams and shape of data comparison for the angle of the support structure. For the final concept design, the final design will be simulated by applying explicit dynamics in ANSYS software and will prove the validity of data from static structural analysis. The explicit dynamic will evaluate the material used for RUPD.



CHAPTER 2

LITERATURE REVIEW

2.1 Introduction of Under-ride Protection Device (UPD)

According to studies, passenger vehicles may survive a frontal truck accident with a relative speed of 75 km/h, provided the truck has an underrun protection system that absorbs energy. The use of energy-absorbing front, rear, and side under-run protection have been estimated to reduce mortality in car-truck crashes by around 12%. In 2000, an EU requirement based on ECE Regulation 93 was implemented, requiring rigid front underrun protection for vehicles with a gross weight of more than 3.5 tons. Furthermore, these technologies could avoid roughly 1176 deaths and 23660 badly injured car occupants in Europe per year. (Mohod, 2017)

Figure 2.1.1 clearly shows that in a crash without the RUPD, the truck's impact is on the passenger compartment due to the automobile underrunning the truck. Because there is not enough energy absorption before the truck collides with the passenger compartment, there will be a high-energy crash, resulting in more fatalities. However, in the next instance, RUPD, energy absorption occurs in the car's bonnet before the impact occurs in the passenger compartment. As a result, there are fewer fatalities in this situation.

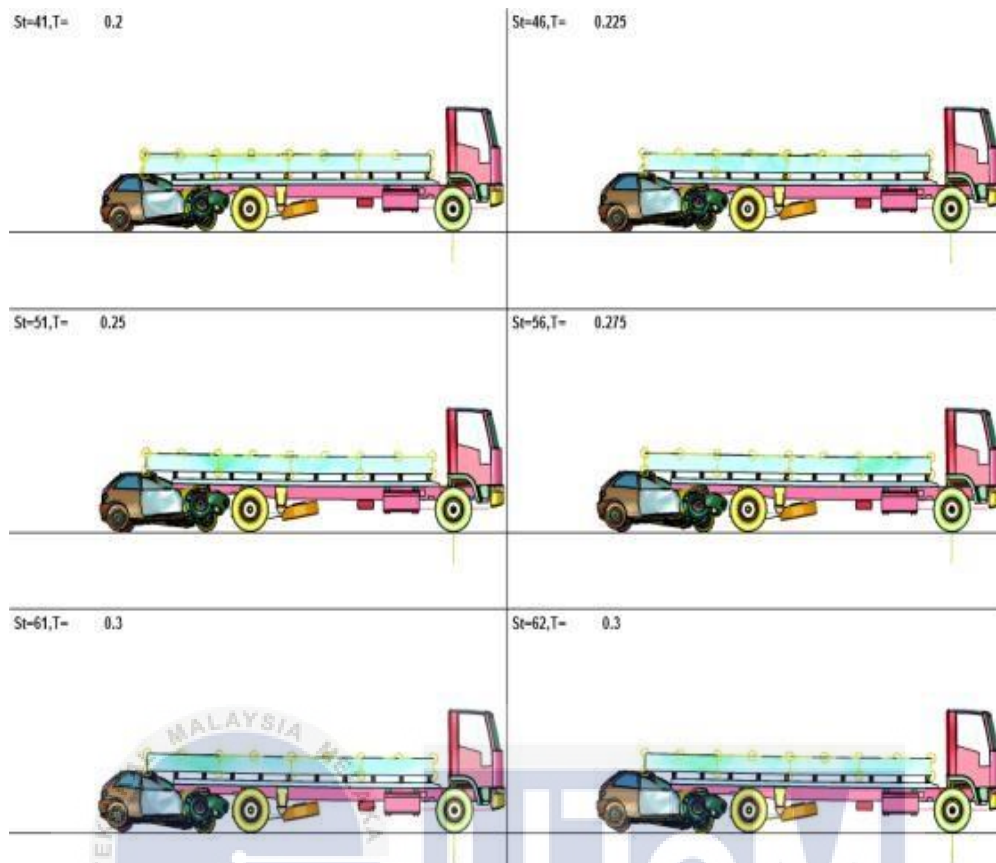


Figure 2.1. 1: Simulation rear impact without RUPD.

ECE Regulation 58, which went into effect in 2005, makes installing the Rear Under-Run Protection Device mandatory for all vehicles weighing more than 3.5 tonnes. (Mohod et al., 2017)

The 1977 study paper “Car-Truck Fatal Accidents in Michigan and Texas” was published by the University of Michigan’s Highway Safety Research Institute (HSRI). US Department of Commerce PB-27-I-111. A study of car-into-truck and car-into-trailer collisions was done. The researchers estimated that there would be 261 fatal rear-end underride car-to-truck crashes every year and 195 fatal side underride car-to-truck incidents. The distribution of impact locations in 181 fatal car-truck/trailer collisions was depicted in this extract illustration from the HSRI study. The research highlights not just the high number and proportion (almost half) of side and side-angular accidents. It says that the

majority (65 of 87) travelled at 30 to 50 mph speeds. Moreover, the angle of impact from 90 degrees is the critical angle of the crash (Figure 2.1.2).

**Figure 1. DISTRIBUTION OF POINTS OF IMPACT
181 CAR - TRUCK / TRAILER FATAL CRASHES**

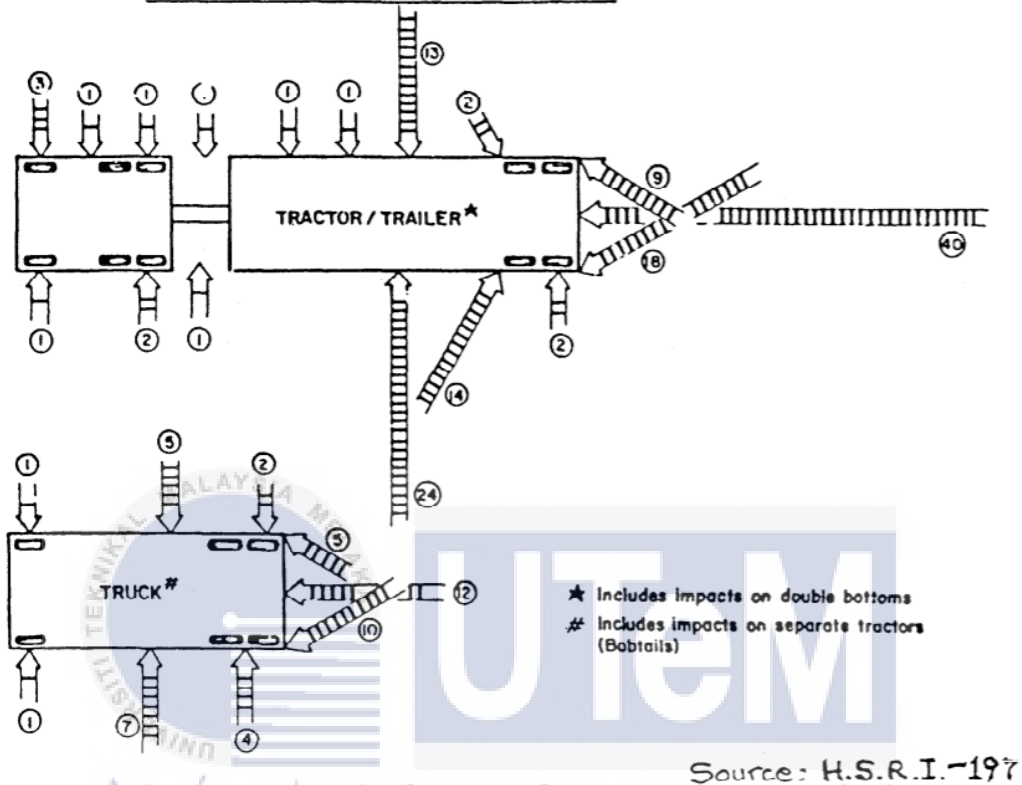


Figure 2.1. 2: Distribution of points of impact.

2.2 Rear Under-ride Protection Device (RUPD)

2.2.1 Design Regulation

The size and height disparity between passenger cars and trucks can cause the vehicle to underride in a rear-end accident, causing the entire vehicle to go underneath the truck. The crumpled passenger compartment absorbs impact energy. This type of collision causes severe harm and death to passengers. According to estimates, energy-absorbing front, rear, and side under-ride protection could cut fatalities in car-truck collisions by roughly 12% (Albahash & Ansari, 2017). For testing the RUPD's potential to safeguard underride crashes

between vehicles and trucks rear-end, the UNECE R58 and FMVSS 223 standards were employed as a reference. The static test is performed on each point of the Rear Underrun Protection surfaces according to the UNECE R58 and FMVSS 223 regulations. The deflection distance on the Rear Underrun Protection surfaces is the topic of the UNECE R58 (United Nations Regulations, 2017) standard. The FMVSS 223 standard, however, is concerned with the deflection distance and energy absorption on the Rear Underrun Protection surfaces. The UNECE R58 and FMVSS 223 standards have the same goal. The Rear Underrun Protection must be strong enough to prevent the automobile from sliding under the truck and enable the automobile's crumple zone to absorb collapse energy. The influence of RUPD support structures is investigated by examining the angle and separation distance of support structures to determine the right design for the safer RUPD support structures.

2.2.2 Dimension of RUPD

The primary needs of rear underrun safety systems are essentially two: preventing the automobile from under riding and absorbing the enormous amount of energy to minimise deceleration peaks and, as a result, passenger injuries. It is also vital to observe the legislation controlling the usage of a new device while creating or redesigning it. The regulation in FMVSS 223 (Federal Motor Vehicle Safety Standards, 2004) requires that (as illustrated in Figure 2.2.1):

- When measured at each support to which the horizontal member is attached, the ground clearance of the horizontal member must not exceed 560 mm.
- The distance between the RUPD and the tail end must be less than 305 mm.
- On each side of the truck, the length of the RUPD shall not exceed 100 mm.
- The cross-sectional guard must be at least 100 mm wide.

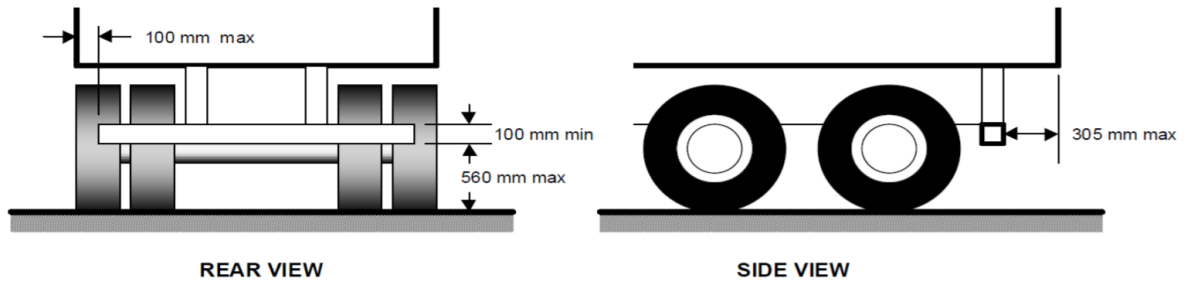


Figure 2.2. 1: Dimensional limit of an RUPD (49 CFR § 571.224 - Standard No. 224; Rear impact protection).

The guards' size criteria (Code of Federal Regulations, Title 49, Parts 571.223 and 571.224) are defined by FMVSS No. 224 (Figure 2.2.1).

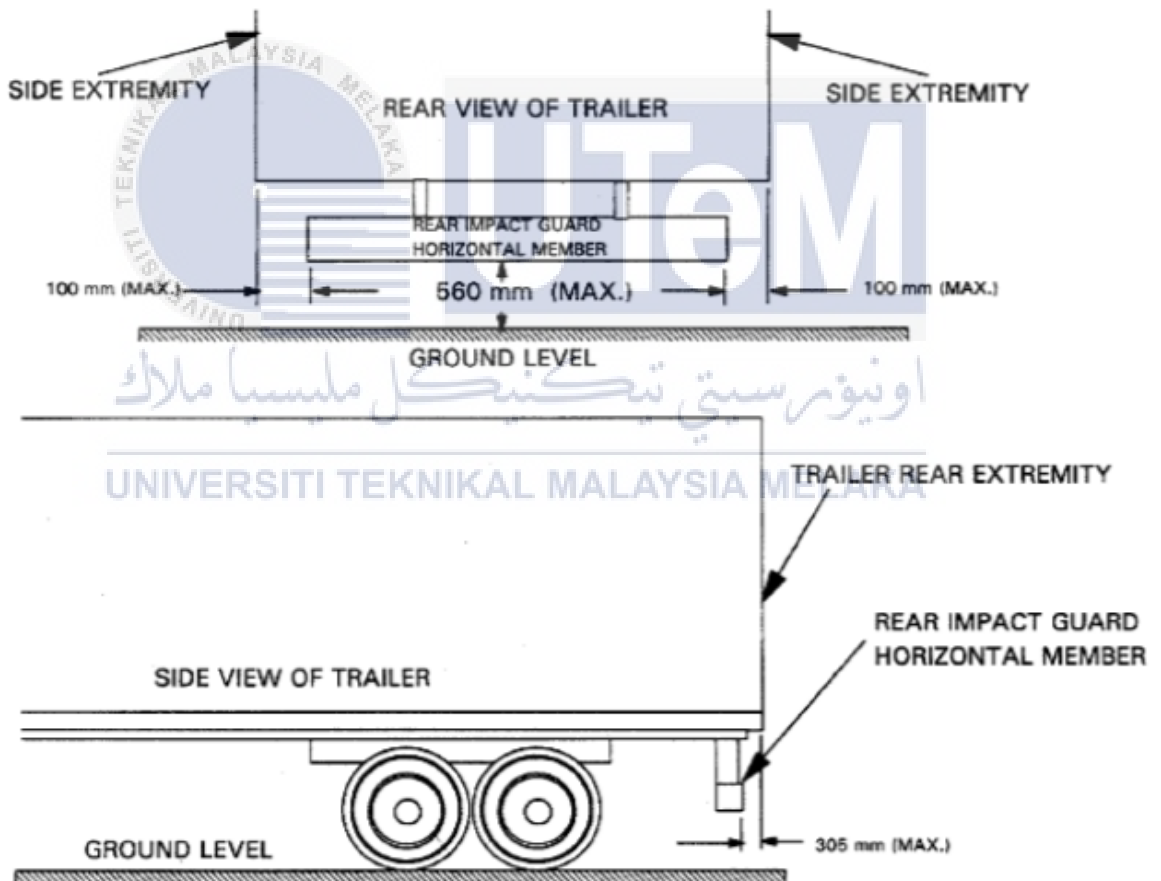


Figure 2.2. 2: Configuration requirements for underride guard (FMVSS 224).

The dimensional requirements of the underride guard are the following (Figure 2.2.2):

- Maximum height above ground: 560 mm. (22 inches)
- Maximum distance from side extremities: 100 mm. (4 inches).
- Maximum offset from the rear plane of trailer: 305 mm. (12 inches)

Additionally, Liu states that the distance between the RUPD and the vehicle's chassis should not exceed 450 mm (Side View). The RUPD requires a minimum ground clearance of 550 mm. It should be capable of supporting a substantial amount of weight and must remain in place through the impact. The transverse profile of the device must not be less than 100 mm in height. The side margins of this profile should not be curled back and should not have any sharp edges (Liu et al., 2010).

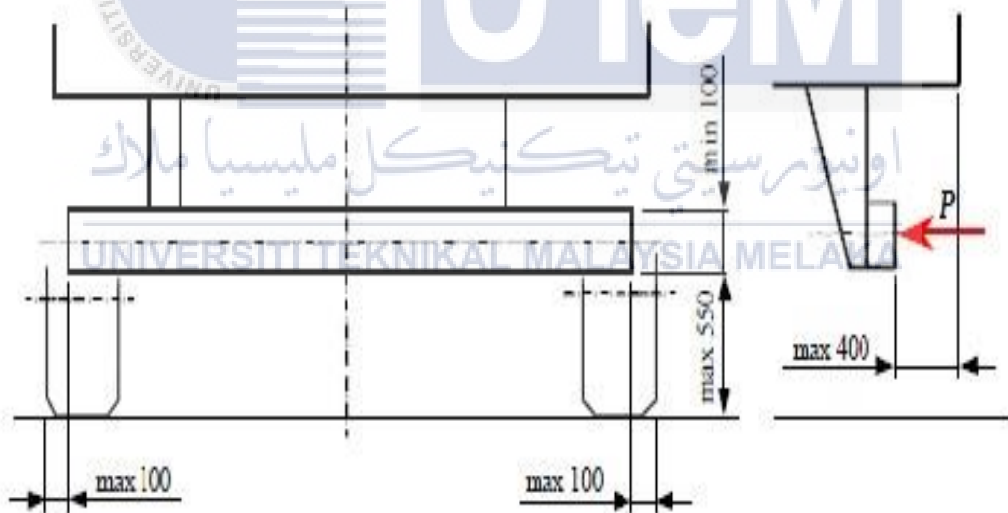


Figure 2.2. 3: Design and Mountings of RUPD Model

The RUPD below contains the regulations governing rear under-ride protection devices in the United States of America.

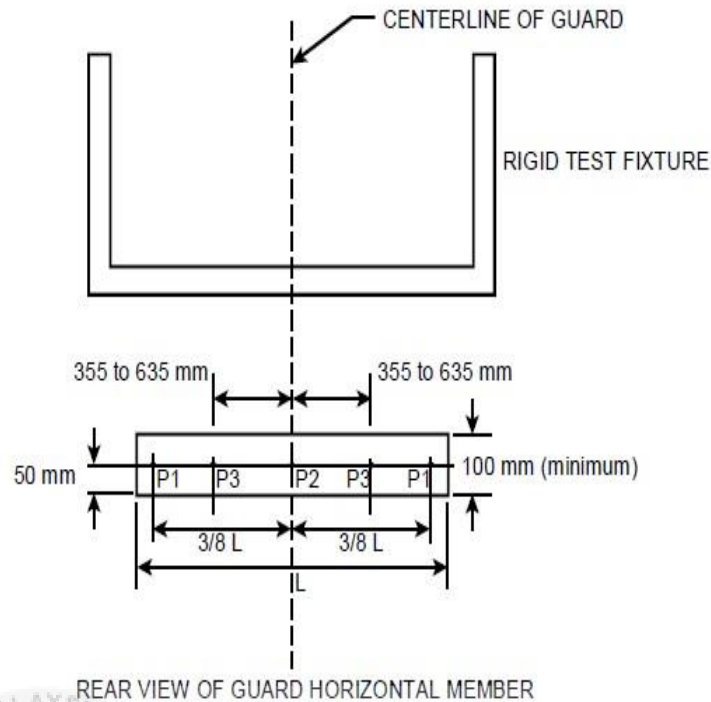


Figure 2.2. 4: Rear views of the device (Belair, 2014).

As seen above, the guards must have a minimum cross-section of at least 100 mm at any point on guard and must pass severe strength testing. The maximum permissible deflection of the guard during these tests is 125 mm.

UNIVERSITI TEKNIKAL MALAYSIA MELAKA

2.2.3 Material Details and Element Criteria

2.2.3.1 Steel

For more than a century, steel sheets have been employed in vehicle structures. Numerous researchers have examined its crashworthiness and discovered a higher energy absorption capacity.

2.2.3.2 Aluminium

Due to aluminium's low density and excellent energy absorption capability, it have been used in various automotive structures. A comprehensive experimental and numerical

study of the crash behaviour of circular aluminium tubes subjected to axial compressive loading was conducted by several researchers. Non-linear FE studies are performed to simulate quasi-static and dynamic test circumstances. The crushing force and fold formation predicted numerically are in good agreement with the experimental data.

2.2.3.3 Magnesium

Magnesium has recently garnered considerable attention from the automobile sector, owing to its appealing low density. It is the lightest structural metal available (78 per cent lighter than Steel and 35 per cent lighter than aluminium). Additionally, it is a plentiful structural substance in the Earth's crust and saltwater. It has been employed in various automobile components due to its superior casting qualities.

2.2.3.4 Polyethylene

Polyethylene is one of the essential polymer kinds for studying non-linear deformation under flexural loading circumstances.

2.2.4 Effect of support structure angle

Figures 2.2.5 and 2.2.6 illustrate the internal energy and displacement of the proposed RUPD at various support angles. In the initial stage of inquiry, the support structure angle is defined as 15, 30, 45, and 60 degrees, as illustrated in Figures 2.2.5 (a) and 2.2.6 (a), to determine the amount of energy absorbed by the device and the amount of bending displacement in each support structure during auto collisions. The figures indicate that the support structure at a 15-degree angle has the best energy absorption capacity while requiring the least bending displacement. The second stage established the support structure angles of 15, 20, 25, and 30 degrees for further examination. The findings shown in Figures 2.2.5 (b) and 2.2.6 (b) indicate that the energy absorbed by the support structure at an angle of 20 degrees is nearly equal to that at a 15-degree angle.

Additionally, the displacement of the support structure at a 20-degree angle is similar to that at a 15-degree angle and is less than that at a 25 or 30-degree angle. As a result, the safer RUPD's 20-degree support structure has been defined. (Pooudom et al., 2019)

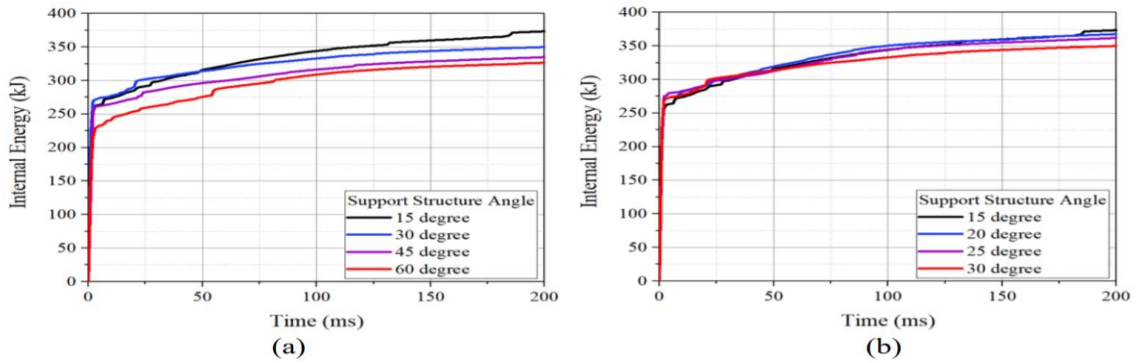


Figure 2.2. 5: (a) Internal energy for 15, 30, 45, 60 degree, (b) Internal energy for 15, 20, 25, 30 degree.

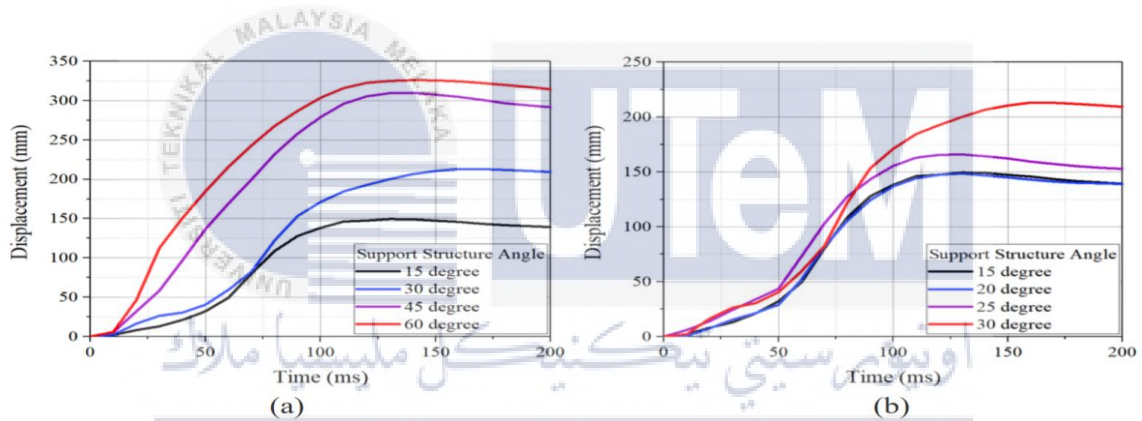


Figure 2.2. 6: (a) Internal energy for 15, 30, 45, 60 degree, (b) Internal energy for 15, 20, 25, 30 degree.

2.2.5 Effect of The Separation Distance Between Support Structures

The impact of the separation distance between support structures was explored by comparing two conditions of separation distance: a standard distance of 748 mm (30 per cent of crossbar length) and a vast space of 1232 mm (50 per cent of crossbar length), as seen in Figure 2.2.7.

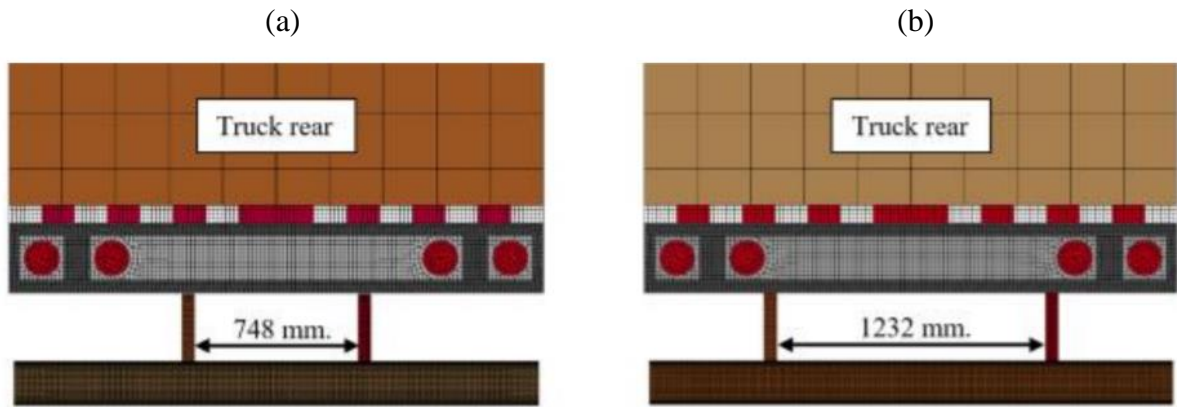


Figure 2.2. 7: Separation distance between support structures of (a) legal separation, (b) wide separation.

As seen in Figure 2.2.8, the crash simulation is configured for three conditions: full width, 50% overlap, and 30% overlap. The vehicle's speed was set to 56 km/h, and the ground clearance was set to 37 cm in all situations.

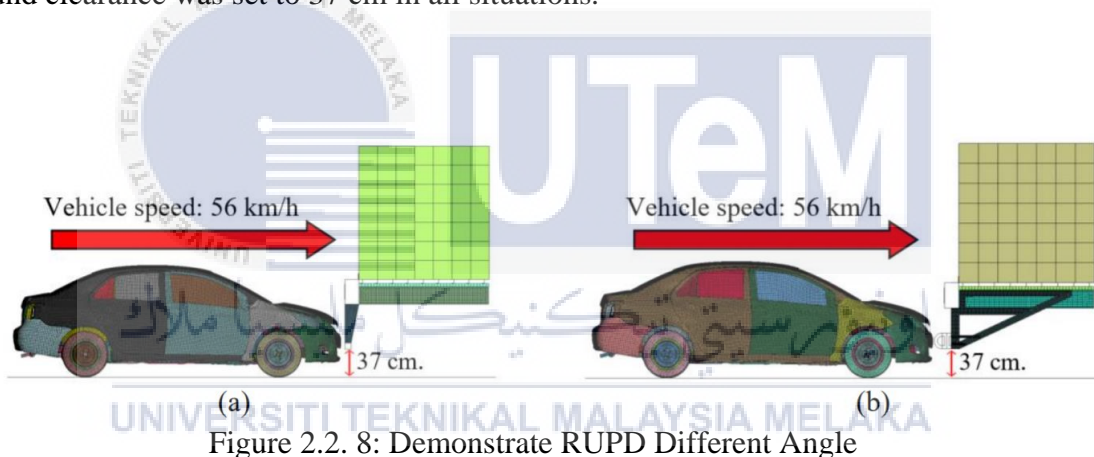


Figure 2.2. 8: Demonstrate RUPD Different Angle

The results demonstrate that no underride occurs in a total width accident. Additionally, the longitudinal deformation of the A-pillar is zero for both conventional and wide separation RUPD. Zero longitudinal A-pillar distortion is assessed in the event of a 50% overlap impact. There is no override for either conventional or wide separation RUPD.

For a crash with 30% overlap, the underride is evident in the standard separation RUPD, with a longitudinal A-pillar deformation of 24 cm. On the other hand, no underride occurs in broad separation RUPD, and no longitudinal A-pillar deformation occurs. Wide separation RUPDs absorb more energy than regular separation RUPDs, resulting in no

deformation of the passenger cell and no underride following an accident. Despite this, the crossbar of each RUPD bends forward due to the offsetting impact (Pooudom et al., 2019).

2.2.6 Simulation Condition

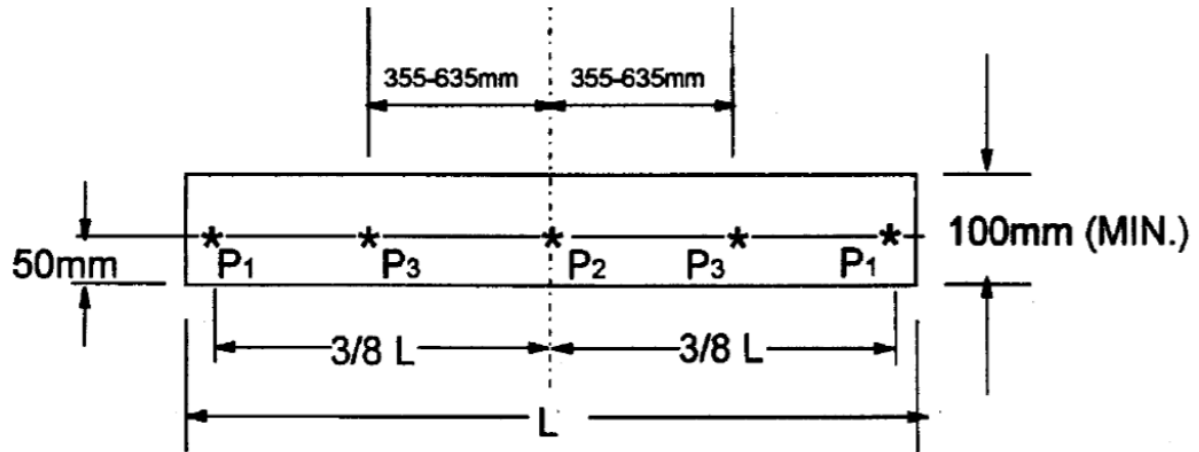
Not only is the Underrun Protection device a robust construction, but it is also capable of absorbing impact energy, therefore securing the car's occupants. According to the Department of Transportation and the National Highway Traffic Safety Administration (NHTSA), the stiffer the Underrun Protection systems, the more likely they are to damage passengers. On the other side, the more Underrun Protection fails, the more dangerous it becomes for passengers. The study's purpose is to design and build a safer RUPD capable of absorbing collapse energy while remaining robust enough to safeguard against rear underride truck collisions.

Underride guards must pass a strength test on trailers with a gross vehicle weight rating (GVWR) of 10,000 pounds or more constructed on or after 24 January 1998, according to Federal Motor Vehicle Safety Standards (FMVSS) Nos. 223 and 224, while FMVSS No. 223 specifies DOT-compliant guards' strength testing and energy absorption criteria. The final regulation, issued in 1996 (Federal Register, Vol. 61, No. 16, page 2004), cites 11,551 rear-end incidents involving passenger cars that resulted in roughly 423 passenger car occupant fatalities and 5,030 non-fatal injuries.

The criteria for energy absorption and strength testing are set at the sites shown in Figure 2:

- At P1 and P2, the protection device must withstand a force of 50,000 N without deflecting more than 125 mm.
- At position P3, the protection device must withstand a force of 100,000 N without deflecting more than 125 mm.

- At each P3 site, the protection device should absorb 5,560 J of energy within the first 125 mm of deflection.



REAR VIEW OF GUARD HORIZONTAL MEMBER

Figure 2.2. 9: Strength test and energy absorption test locations (FMVSS 223).

These rules superseded the Federal Motor Carrier Safety Regulations (effective 1 January 1952–25 January 1998) that required rear-impact guards. Still, they needed them to be significantly smaller without a strength test. Before 1998, certain vehicle manufacturers voluntarily added rear impact shields in compliance with the Truck Trailer Manufacturers Association (April 1994). Although these rear impact guards fulfil the size criteria of FMVSS 224, it is uncertain if they were tested or fulfilled the strength standards of FMVSS 223.

Additionally, by observing the implementation of RUPDs that ECE's R58 governs, Indian rule IS 14812 – 2005 is based on the ECE R58 standard and has the following requirements.

1. When in service, the device should provide enough resistance to forces applied parallel to the vehicle's longitudinal axis and be attached to the chassis side members or whatever replaces them. This criterion is achieved if it can be demonstrated that the horizontal distance between the rear of the device and the

vehicle's rear extremities does not exceed 400 mm at any of the positions P1, P2, or P3.

- Any portion of the vehicle more than 3 metres above the ground while the car is empty should be eliminated from this measurement.
- Point P is located 300 + 25 mm from the longitudinal planes tangential to the outer edges of the rear axle's wheels; point P2 is located on the line connecting points P1 and is symmetrical to the vehicle's median longitudinal plane at a distance of 700 to 1000 mm inclusive, the exact location is specified by the manufacturer.
- The vehicle manufacturer should define the height above the ground of locations P1 and P2 within the horizontal boundaries of the device. However, the size should not exceed 600 mm when the vehicle is empty. P3 is the centre of the straight line that connects points P2 and P3.
- To both points, P and P3, a horizontal force equivalent to 12.5% of the vehicle's maximum technically allowable weight but not exceeding 25 kN should be applied consecutively.

2. Both points P2 should be sequentially applied with a horizontal force equivalent to 50% of the vehicle's maximum technically allowable weight but not exceeding 100 kN.
3. Separately, the forces mentioned above shall be applied to the same guard. The manufacturer may specify the order in which the forces are applied.
4. The following criteria must be met when conducting a practical test to verify conformity with the preceding standards.

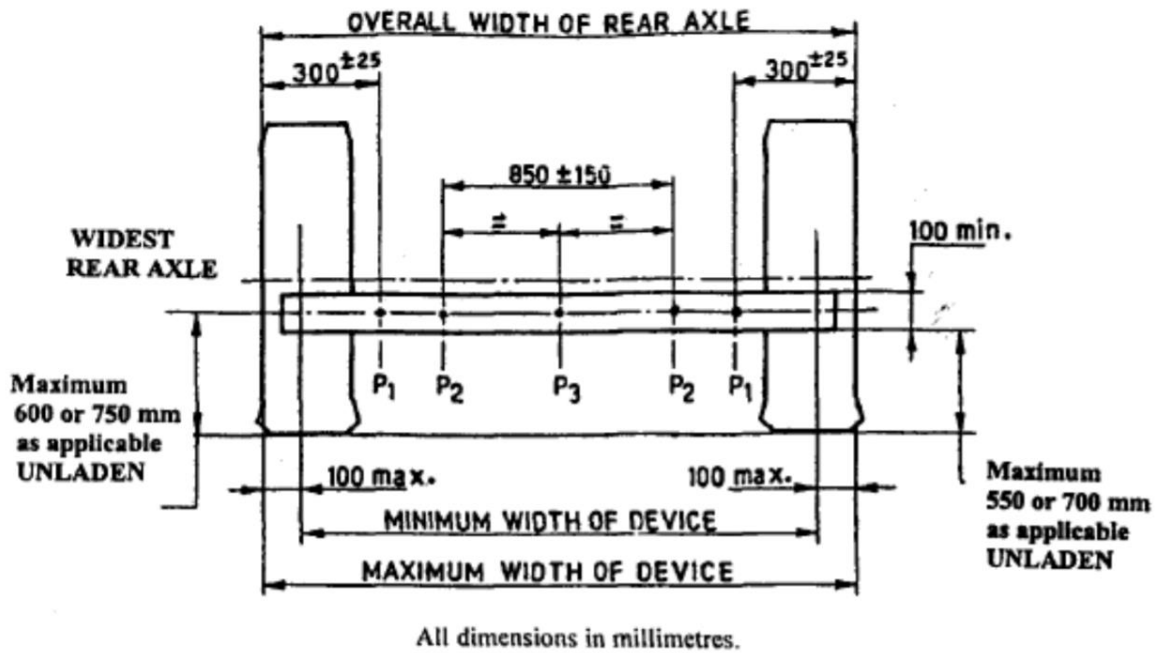


Figure 2.2. 10: Indian Standard of RUPD (IS 14812-2005)

5. Procedure for Testing

The following process for testing the Rear Under Run Protection device is based on the ECE R-58 and IS-14812 2005 regulations. The Rear Guard assembly was subjected to a quasi-static study, and its load-bearing ability was determined. Quasi tests are a slower variant of dynamic tests utilised when dynamic code provides static results. A horizontal force of 100 kN or 50% of the force generated by the vehicle's maximum mass, whichever is less, shall be applied sequentially to two points located symmetrically about the vehicle's centre line, whichever is applicable, at a minimum distance of 700 mm and a maximum distance of 1 m apart. The manufacturer may specify the order in which the forces are applied.

A horizontal force of 50 kN or 25% of the force generated by the vehicle's maximum mass, whichever is less, shall be applied sequentially to two points located $300 + 25$ mm from the longitudinal planes tangential to the outer edges of the rear axle's wheels, and to a

third point situated on the line connecting these two points in the vehicle's median vertical plane.

Additionally, the Loading Device and loading direction are depicted. The regulations' specifications manufacture the loading device. The loading device is constructed as seen in Figure 2.2. 11.

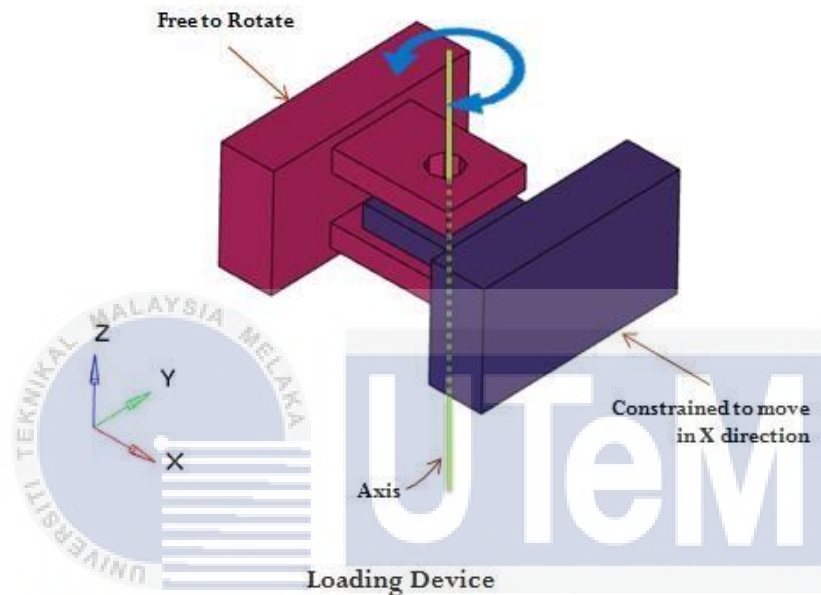


Figure 2.2. 11: Loading Device Mechanisms

Rather than that, a separate test utilising a “Uniform Load Test Force Application Device” is conducted. This device must measure 203 mm in height and have a width more significant than the distance between the outside margins of the guards' outer supports. The device's centre must be aligned with the guard's centre axis and steered to avoid rotation during testing.

CHAPTER 3

METHODOLOGY

3.1 Overview of Methodology

Methodology and methods are frequently used interchangeably. The process is a more extensive term that encompasses all forms. It comprehends the social-organisational framework, underlying beliefs, ethical standards, and political issues. Additionally, it is a system of procedures employed in a particular field of study or activity. This chapter will discuss the methodology to analyse the crashworthiness of the project proposed.

3.2 Specification of Research

The specification of this research must be defined to go forward with the approach based on the findings of the study conducted. The following section will summarise the most important specifications and references for this project research.

3.2.1 Type of Heavy Truck

Mitsubishi FUSO lorry was chosen for the installation of the under-run guards and also for subsequent engine calculation. This lorry is an FM 657 J model. Mitsubishi FUSO lorry was selected for the under-run guards' structure and following engine calculation. This lorry is an FM 657 J model. figure below shows the model and the dimension of the truck.



Figure 3.2. 1: FUSO 16 000kg trucks.

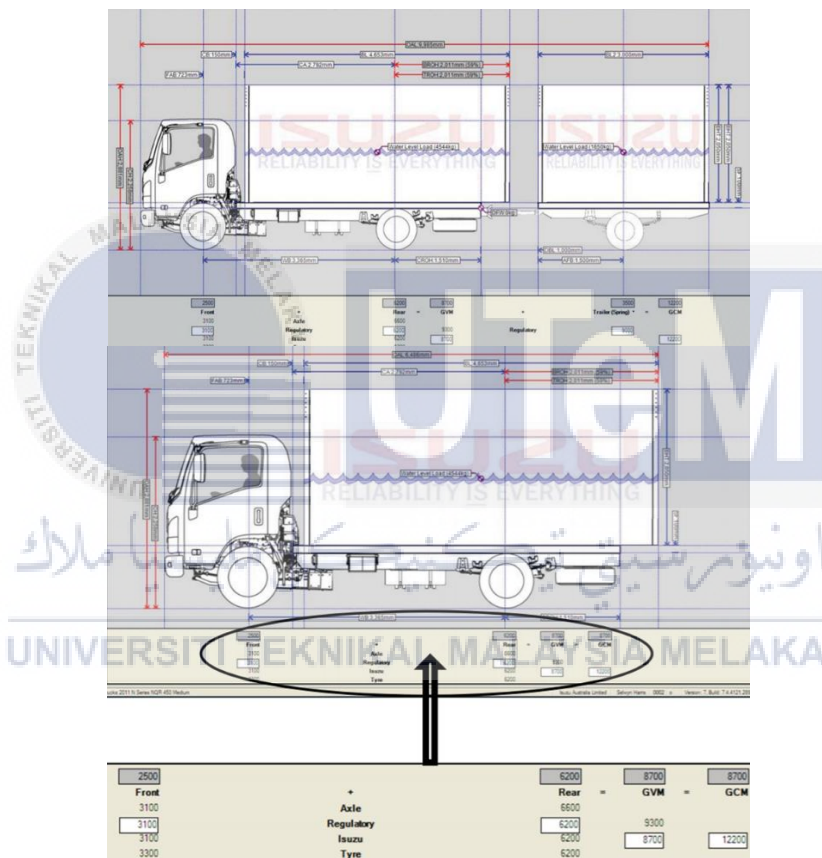


Figure 3.2. 2: Dimension FUSO truck.

3.2.2 Dimension of RUPD

The dimensions for RUPD shall be determined by FMVSS 223 (2004 Federal Motor Vehicle Safety Standards) and ECE Regulations. For RUPDs, the size highlighted is the support distance; with a greater spacing, RUPDs absorb more energy (50 per cent of crossbar length). Additionally, a guard with a lower clearance (480 mm vs 560 mm) allowed for effective engagement with both passenger vehicles travelling at 48 km/h (29 mph).

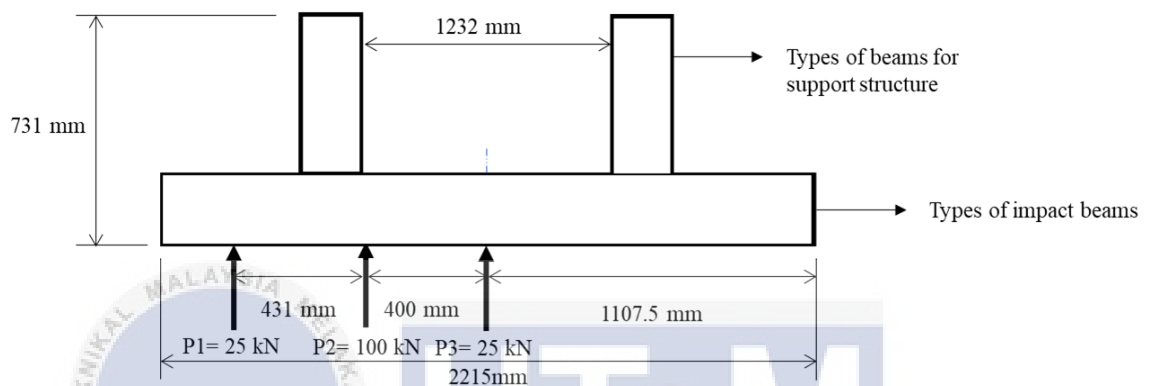


Figure 3.2. 3: Dimension of RUPD based on the FUSO truck.

3.2.3 Analysis Condition of RUPD

This subtopic will summarise the RUPD conditions encountered during the exercise. According to the HSRI, most drivers were travelling at speeds of 30 to 50 miles per hour. Thus, 50 mph will be the reference point for the maximum crash velocity. The conditions for both underride guards will be governed by the National Highway Traffic Safety Administration (NHTSA), the United Nations Economic Commission for Europe's Sustainable Transport Division, the Federal Motor Vehicle Safety Standards (FMVSS), and the Australian Trucking Association's Technical Advisory Procedure (TAP) (ATA).

3.2.3.1 Simulation Condition of RUPD

Federal Motor Vehicle Safety Standards (FMVSS) 223 and 224 oversee standards governing rear under-ride protection devices, whereas FMVSS 223 stipulates the strength testing and energy absorption parameters for DOT-compliant guards. Five forces act on the

RUPD, which account for 50% and 25% of the force created by the vehicle's maximum mass. For additional information, please refer to the Federal Motor Carrier Safety Regulations.

3.3 Flow Chart

Designing rear under-run guards for big vehicles involves multiple processes. The flow chart below illustrates developing a more effective under-run protection. The first approach is research to create new devices for these underrun protections. Then, following the research study, the concept design phase can begin. The most inventive design will be chosen. After assembling all of the components for this gadget, the following step is to sketch each member using CATIA. CAD software to complete the mechanical drawing. Then, using CES software, a configuration design was used to demonstrate material selection. Following that, perform a CAE analysis on the product using ANSYS software. Finally, the new product's detailed drawing will be completed. The flow chart depicted in Figure 3.3.1 summarises the methods used in this investigation.

UNIVERSITI TEKNIKAL MALAYSIA MELAKA

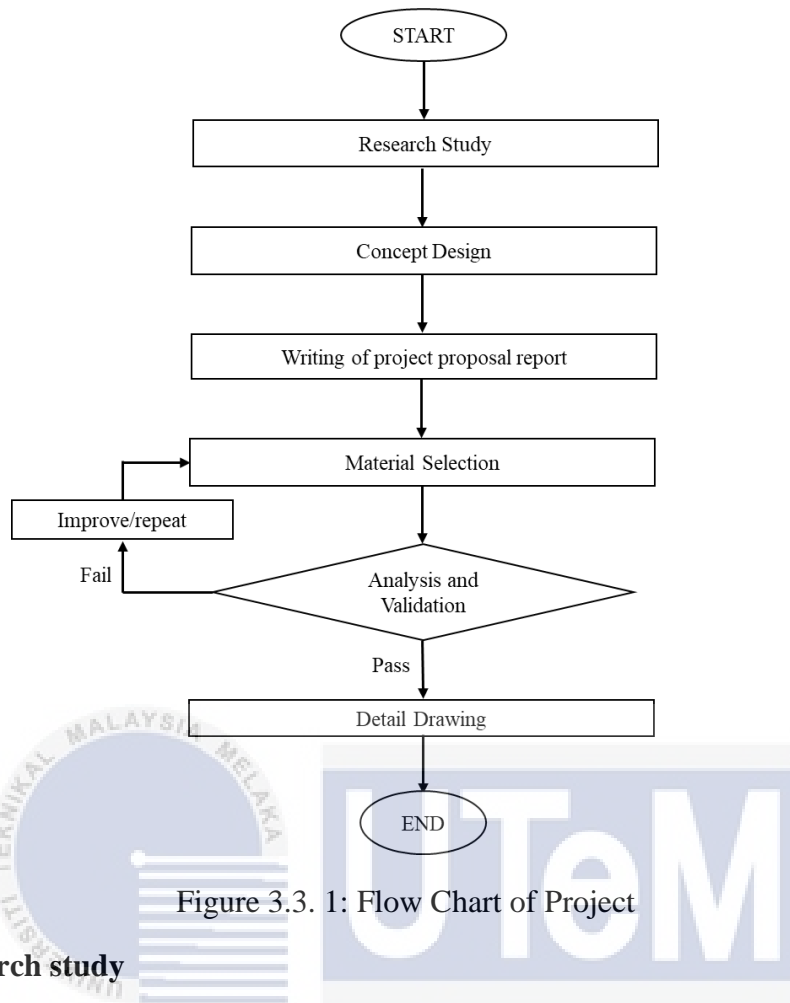


Figure 3.3. 1: Flow Chart of Project

3.3.1 Research study

Background research was undertaken to gather data for this project. For this research, the characteristics of heavy trucks have been classified. Studying the pattern and materials used for barrier protection is also necessary to achieve the most significant outcomes. Some patterns have been discovered for the under-run, such as guard rails or square tunnels. Steel is a frequently used material for this form of defence. This information is available in journals, websites, books, and other research sources, and this review will focus exclusively on rear under-run guards. This strategy will be explained in greater detail throughout this study.

3.3.2 Concept Design

The concept design phase of project planning involves generating the project's central idea. On the other side, a design philosophy is a concept that guides a design. Each

product component will have multiple concepts, and the best one will be chosen. Three designs of rear under-run are completed at a minimum. Later in this article, a different design will be shown for each concept discussed.

3.3.3 Drawing by Using CATIA Software

The application of computer technology to design documentation is called CAD (Computer-aided Design). Additionally, this tool automates the drafting process, formerly performed manually. After receiving all preliminary designs, the specification for these barrier protection heavy vehicles will be created using the CATIA programme. Only one design was chosen and developed for the back underruns. Each component of the concept must be sketched appropriately utilising this application.

3.3.4 Material Selection

Material selection is an essential point in any physical object's design. The primary purpose of material selection in product design is to lower costs while preserving production efficiency. Materials for under-runs must be carefully selected to generate a high-quality, long-lasting product. This study will use four materials: mild steel, aluminium alloy, magnesium alloy, and one plastic material, polyethene. This plastic material has been chosen since the world towards the 4.0 Industrial Revolution when 3D printing using plastic material was in advance.

3.3.5 Analysis and Validation

After selecting and drawing the design in CATIA, the research team will undertake analysis utilising Computer-Aided Engineering (CAE). Additionally, CAE is accessible in CATIA, ANSYS, and SOLIDWORKS. The study investigates and evaluates elements or structures by dismantling them and revealing their interrelationships. The gadgets will be subjected to a force sufficient to imitate an automobile colliding with the back of a truck

travelling at 50mph, and the effect will be observed. CAE will be used to accomplish this goal. This thesis will be discussed in further detail in terms of validation by comparing the shape of data obtained with others research and comparing manual calculation for simple structures.

3.3.6 Detail Drawing

A detailed drawing represents a portion of a building, machine, or something at a reasonable big scale that includes measurements or additional information used in the construction process. Eventually, assembly sketches should be included with the final drawings and information on repair and safety considerations if applicable.

3.4 Design Process

The engineering design process can result in various outputs depending on the situation. The engineering design process is a systematic sequence of stages that engineers follow to build functional products and procedures for the real world. As an added advantage, engineers go through the design process to discover a solution for any problems they may be faced. This sub-topic will show the design process for this project.

3.4.1 House of Quality

To determine which engineering qualities should be considered as design restrictions and used as choice criteria when selecting the best concept design, the House of Quality adopts a formalised process. This document takes the information generated by the design team and leads them by turning it into a more valuable format for creating future products. The eight rooms in this HOQ are as follows: engineering characteristics, improvement path, units, customer need, raw score, relative weight, significant weight factors, and rank order. The first and most important goal in its most extensive form, the HOQ process, will define

a collection of critical features and product success metrics that will act as the design team's goal values when completed. This information comes from Engineering Design (Dieter & Schmidt, 2013).

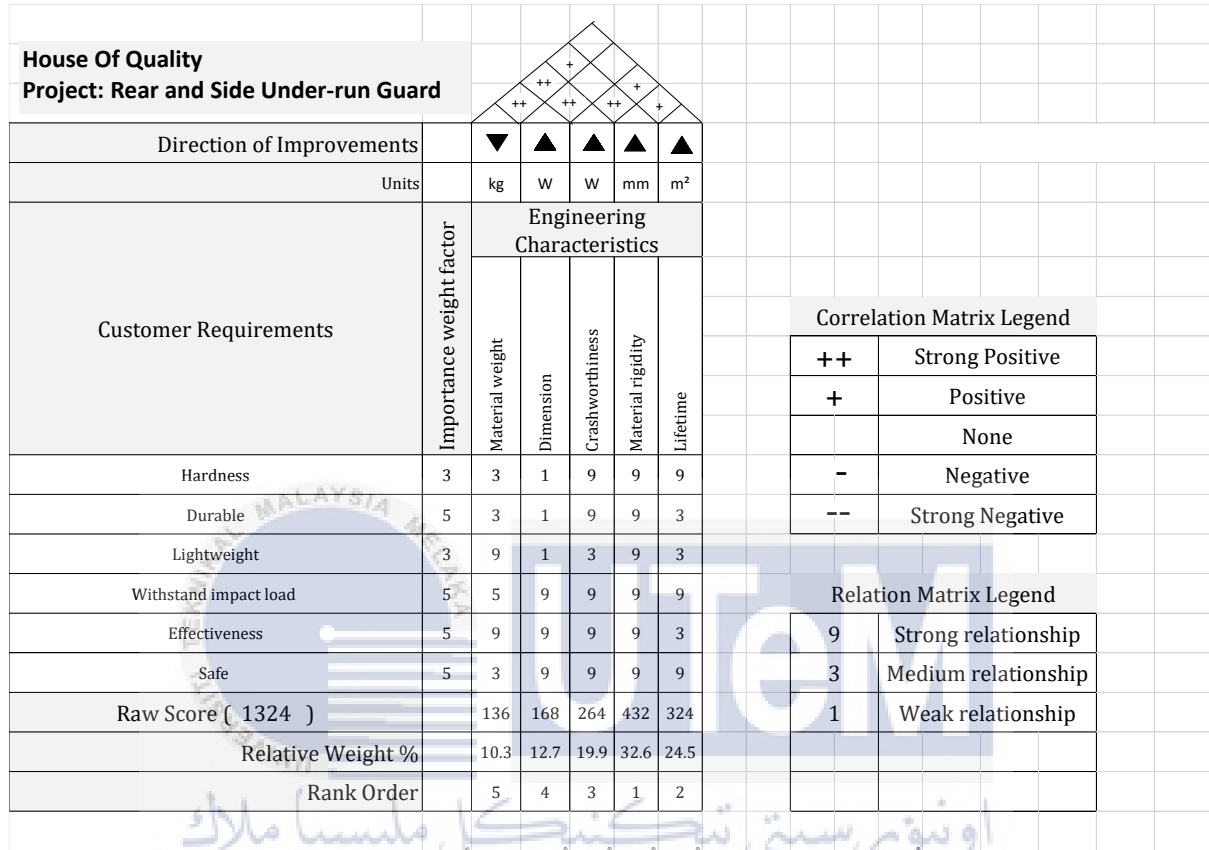









Figure 3.4. 1: House of Quality

According to the House of Quality table for an under-run guard, material rigidity is the most crucial factor to consider. Consequently, it is the most significant criterion to consider. It will impact the device's ability to endure an impact load and its strong hardness and overall life span. Material stiffness provides a value of 32.6 per cent for relative weight. In addition, a lifetime for guards in the second rank order has a 24.5 per cent relative weight. The crashworthiness of the guards is assigned a relative weight of 19.9 per cent in the third position of the ranking system. Furthermore, the dimension of the guards at the fourth while the lowest rank is the device's weight. As a result, the relative weight in HOQ is 12.7 per cent for dimension and 10.3 per cent for weight.

3.4.2 Morphological Chart

There are three steps to the overall morphological approach to design that should be followed. To begin, break down the general design problem into smaller, more manageable subproblems. Next, construct solution concepts for each subproblem that has been identified. Finally, merge subproblem answers into different complete solutions systematically and evaluate all possible combinations. Methods based on morphological charts assist in structuring the problem to synthesise various components that all provide the exact required functionality. Also known as the functional decomposition method, this mechanical design approach begins with the design problem's applicable breakdown into a detailed function structure.

Table 3.4. 1: Morphological Chart of RUPD

RUPD	CONCEPT			
	1	2	3	4
Material	Mild Steel	Aluminum Alloy	Magnesium Alloy	Polyethylene
Support	 Angle:15°	 Angle 25°	 Angle:45°	
Beam	 Rectangular Hollow Beam	 W-Beam	 Square Hollow Beam	 Circular Hollow Section

The morphological chart for the under-run protection device on the back and side of the vehicle is shown in the preceding table. There are numerous concepts of the under-run guards represented on the chart. In this table, there are three different parameters. The first

thing to consider is the material used to construct the guards. The second point to mention is the support concept for devices—finally, the type of beam used to build the design.

3.4.3 Design Concept

The following procedure is the generation of the design concept for RUPD and SUPD based on the morphological chart above. Each form of under-ride protection device will have three alternative concepts to choose from, which will make it easier to compare and contrast them.

3.4.4 Concept Selection

Concept selection is the process of evaluating concepts concerning customers' needs and other criteria, comparing the relative strength and weaknesses of the concepts and selecting one concept for further development. Based on ideas for each type, the final concept's material will be analysed after the final concept is chosen based on the design analysis.

3.4.5 Modelling of UPD

This process begins with modelling under-run guards and ends with drawing the devices. After that, the components will be analysed using CAE. The model of the Mitsubishi FUSO vehicle will determine the under-run dimension pattern.

CHAPTER 4

RESULTS AND DISCUSSION

4.0 Analysis of RUPD

The crashworthiness simulation of RUPD's condition is shown in the below tables. Figure 4.0.1 (a) shows the material properties for the static structural analysis, which will be constant to compare the strength and energy absorption with different beams and angles of support. The impact loading condition considered during analysis is shown in Figure 4.0.1 (b), following the regulation.

(a)		(b)	
AISI 1020 steel properties		Point	Impact loading condition
Yield strength	350 MPa	P1, P3	A horizontal force equal to 12.5 percent of the maximum technically permissible weight of the vehicle but not exceeding 25 kN shall be applied successively to both points P1 and P3
Ultimate strength	420 MPa		
Poisson's ratio	0.29		
Young's modulus	205 GPa	P2	A horizontal force equal to 50 percent of the maximum technically permissible weight of the vehicle but not exceeding 100 kN shall be applied successively to both points P2
Shear modulus	80 GPa		
Density	7.87 g/cm ³		

Figure 4.0. 1: Condition of simulation RUPD (a) Material properties (b) Impact loading condition.

4.1 Static Structural Analysis

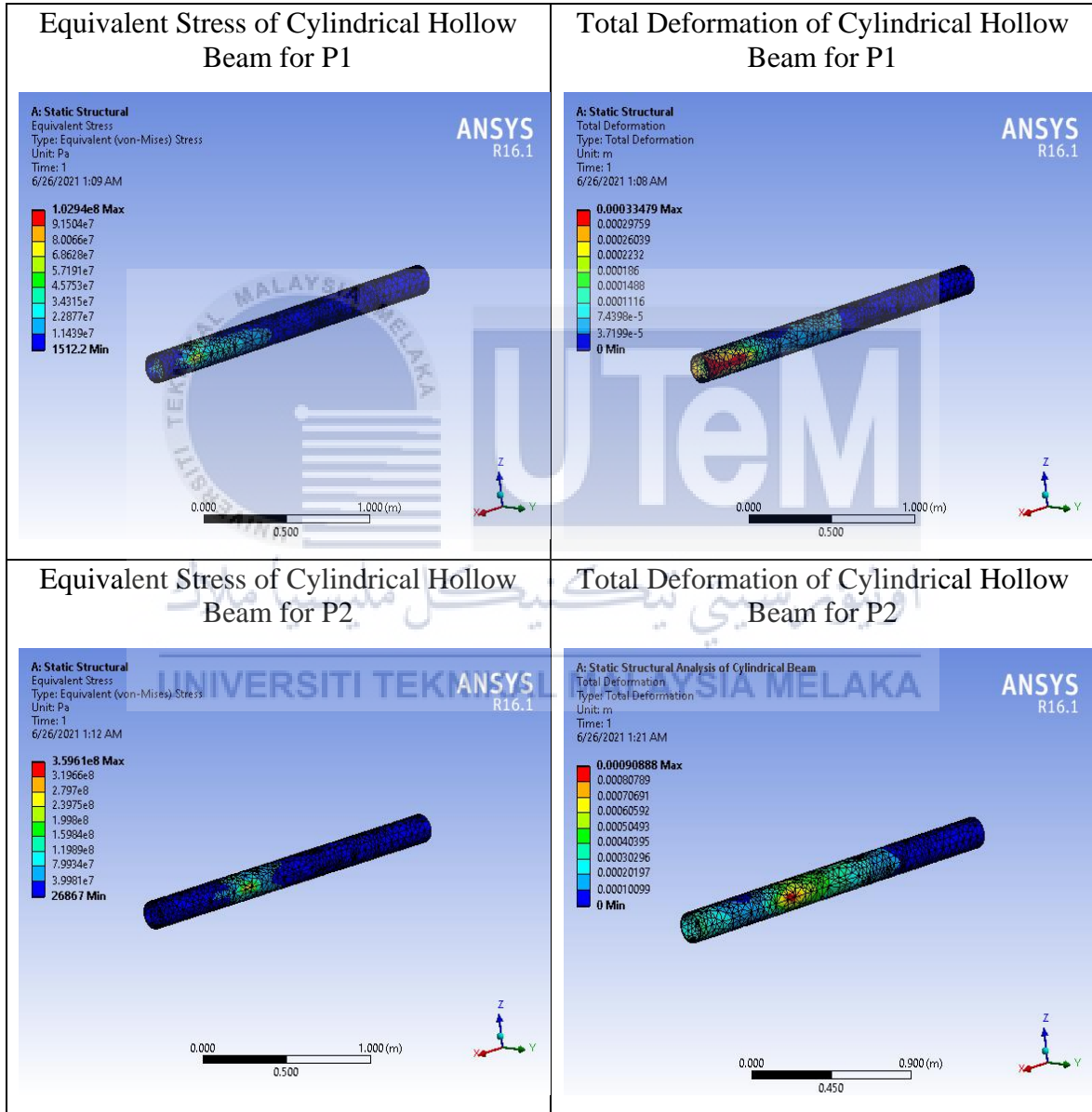
A static structural analysis identifies the displacements, stresses, strains, and forces induced in structures or components by loads that do not create substantial inertia or damping effects. Stable loading and response conditions are assumed, which means that the loads and the structure's reaction will fluctuate slowly over time.

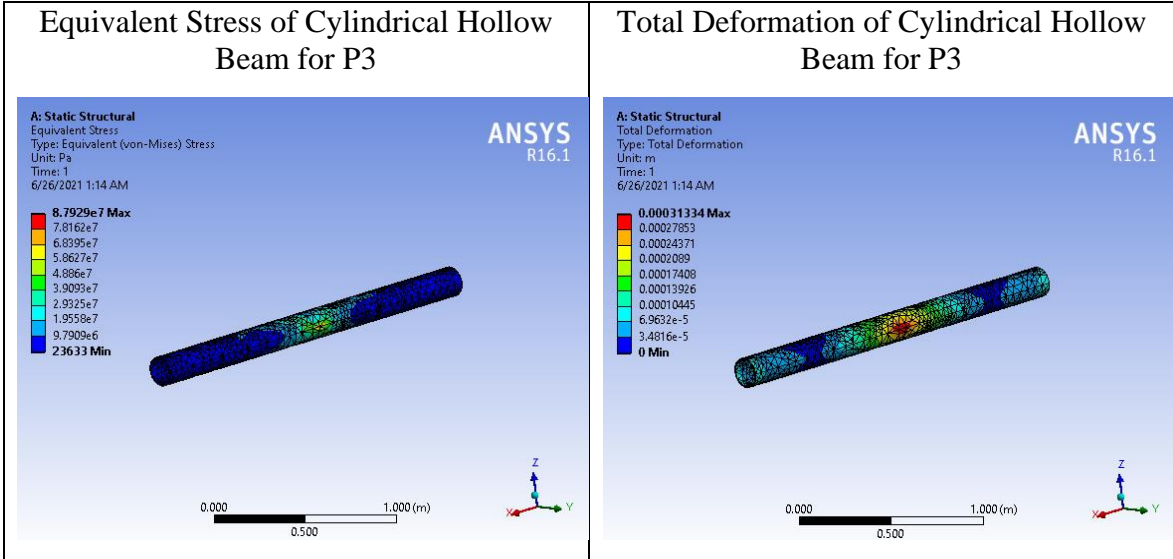
4.1.1 Beams Impact Analysis

Examining the beam type will use static structural analysis for four types of beam: circular hollow beam, W-beam, rectangular hollow beam, and square hollow beam. This section will compare the result from ANSYS with the manual calculation.

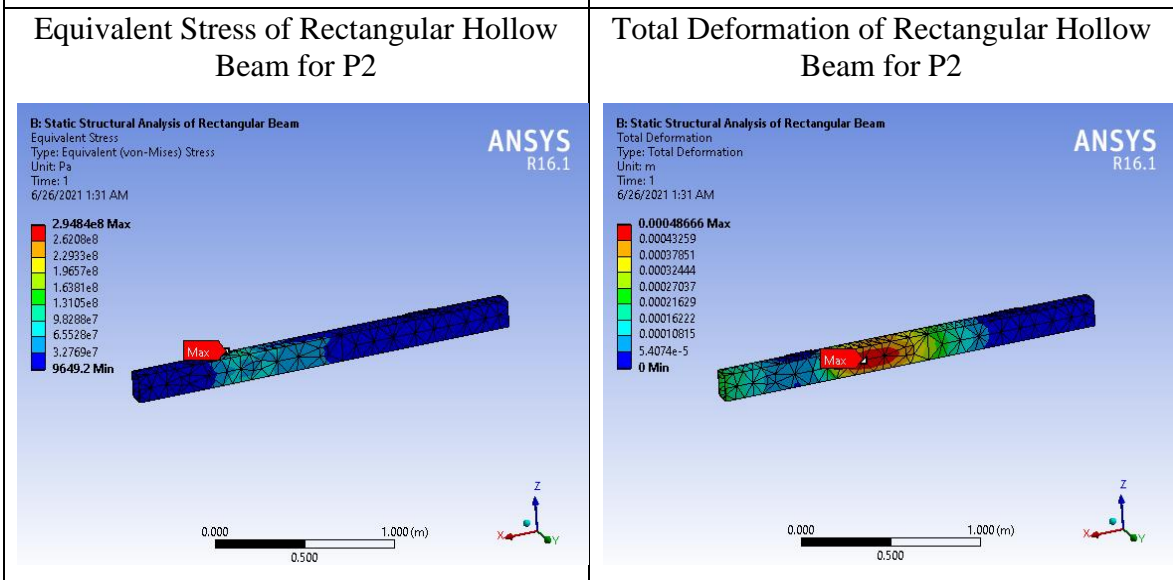
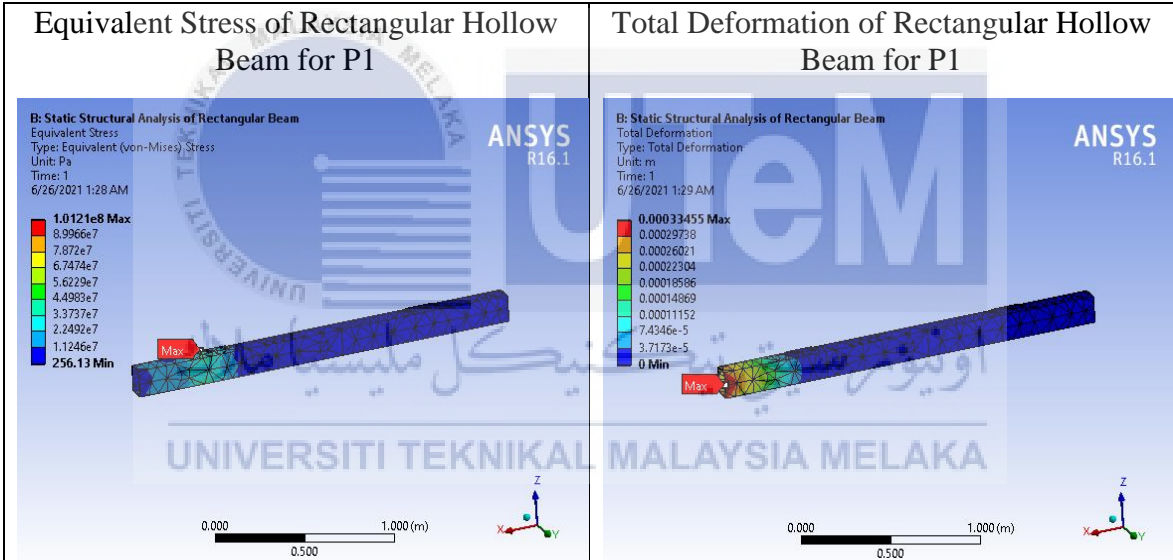
4.1.1.1 Computational Analysis by Using ANSYS Software

i. Cylindrical Hollow Beam

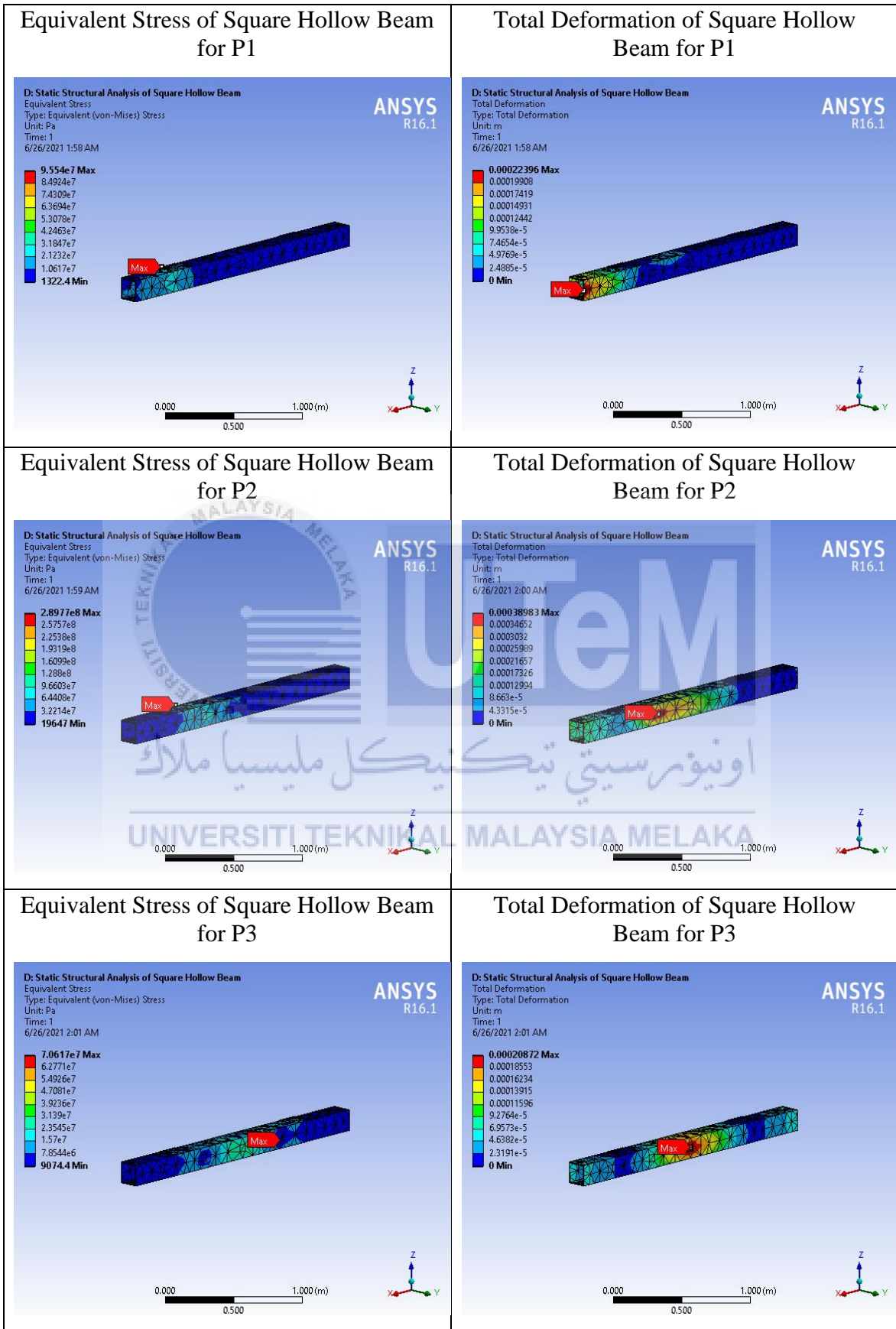




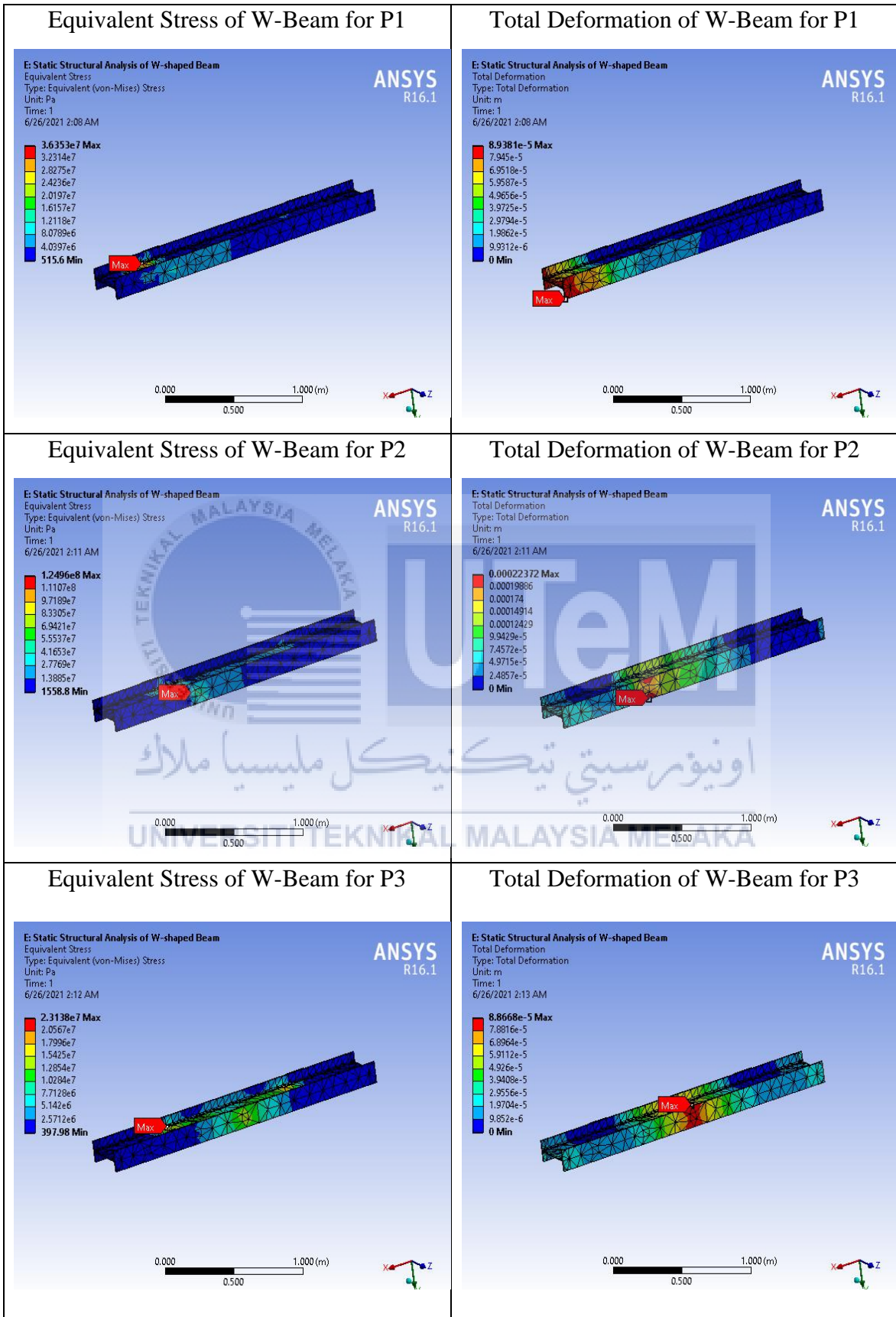
ii. Rectangular Hollow Beam



iii. Square Hollow Beam



iv. W-Beam



4.1.1.2 Manual Calculation by Using Theory Von Mises

$$\sigma_x = \pm \frac{P}{A} \pm \frac{Mc}{I} \quad (1)$$

$$\tau_{xy} = \pm \frac{VQ}{It} \pm \frac{Tc}{J} \quad (2)$$

$$\sigma_{ave} = \frac{\sigma_x + \sigma_y}{2} \quad (3)$$

$$R = \sqrt{\left(\frac{\sigma_x - \sigma_y}{2}\right)^2 + (\tau_{xy})^2} \quad (4)$$

$$\sigma_{1,2} = \sigma_{ave} \pm R \quad (5)$$

$$\tau_{max} = R \quad (6)$$

Using Von Mises Theory,

$$\sigma' = (\sigma_1^2 - \sigma_1\sigma_2 + \sigma_2^2)^{1/2} \quad (7)$$

$$F.S. = \frac{S_{ut}}{\sigma'} \quad (8)$$

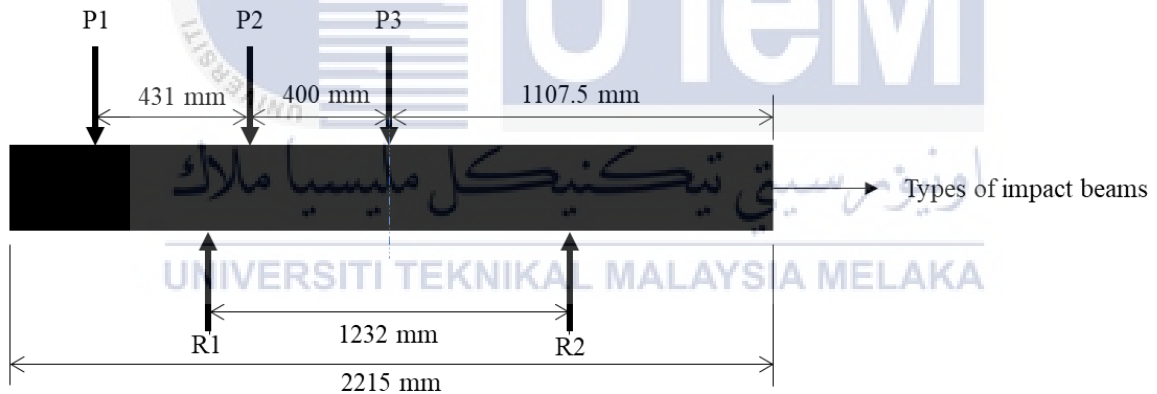


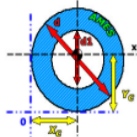
Figure 4.1. 1: Condition of Analysis of Impact Beam

Table 4.1. 1: Type of forces on impact beams.

Force	Description
P1	Based on FMVSS Regulations, using P1= 25 kN
P2	Based on FMVSS Regulations, using P2= 100 kN
P3	Based on FMVSS Regulations, using P3= 25 kN
R1	The reaction force of support structure from fixed support when applying force

R2	The reaction force of support structure from fixed support when applying force
----	--

i. Cylindrical Hollow Beam



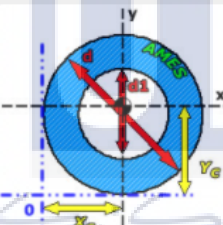
INPUT PARAMETERS	
Parameter	Value
Outer diameter (d)	<input type="text" value="165.1"/>
Inner diameter (d1)	<input type="text" value="159.7"/>
Length (L)	<input type="text" value="2215"/>
Density (p)	<input type="text" value="7.87"/>
<input type="button" value="Calculate"/>	

RESULTS	
Parameter	Value
Cross section area [A]	13.775 <input type="text" value="cm^2"/>
Mass [M]	24.013 <input type="text" value="kg"/>
Second moment of area [Ixx]	4542579
Second moment of area [Iyy]	4542579 <input type="text" value="mm^4"/>
Polar second moment of area [J]	9085158
Section modulus [Sxx]	55028.211
Section modulus [Syy]	55028.211 <input type="text" value="mm^3"/>
Radius of gyration [rx]	57.425
Radius of gyration [ry]	57.425 <input type="text" value="mm"/>
Centroid distance in x direction [xc]	82.55
Centroid distance in y direction [yc]	82.55 <input type="text" value="mm"/>

Note: Use dot "." as decimal separator.

Circular Hollow Section Formulas:

HOLLOW CIRCLE (HOLLOW SHAFT)



Parameter	Symbol	Equation
Cross section area	A	$A = \pi d^2/4 - \pi d_1^2/4$
Area moment of inertia	I_{xx}	$I_{xx} = \pi d^4/64 - \pi d_1^4/64$
Area moment of inertia	I_{yy}	$I_{yy} = \pi d^4/64 - \pi d_1^4/64$
Section modulus	S_{xx}	$S_{xx} = 2I_{xx}/d$
Section modulus	S_{yy}	$S_{yy} = 2I_{yy}/d$
Centroid	x_c	$x_c = d/2$
Centroid	y_c	$y_c = d/2$
Mass	M	$M = AL\rho$
Radius of gyration	r	$r = (I/A)^{0.5}$
Polar moment of inertia	J	$J = I_{xx} + I_{yy}$

Figure 4.1. 2: Cylindrical hollow beam properties.

P1

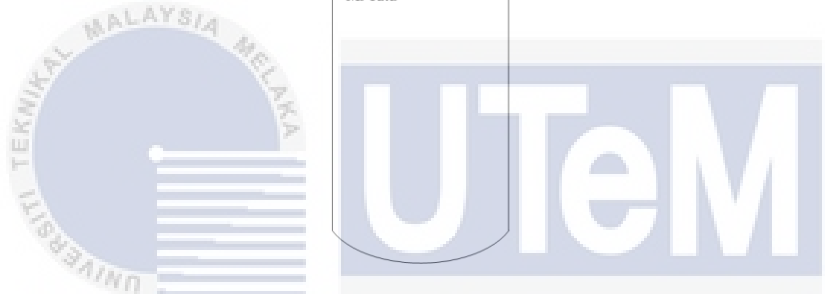
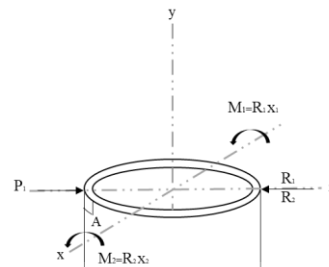
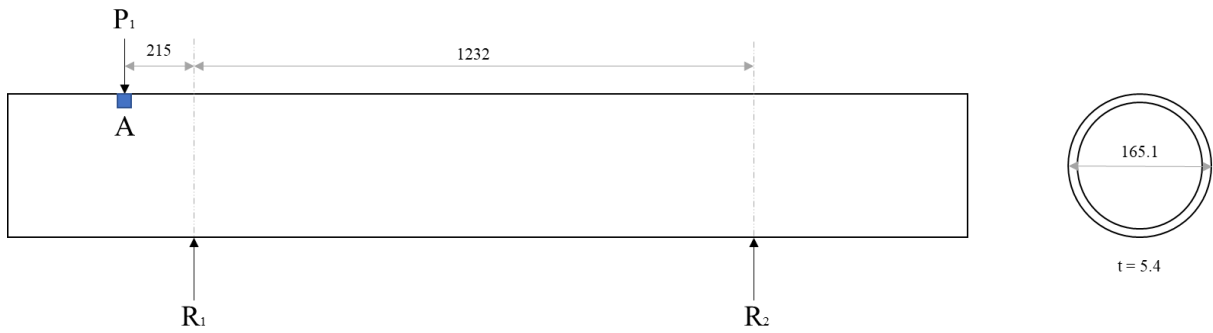
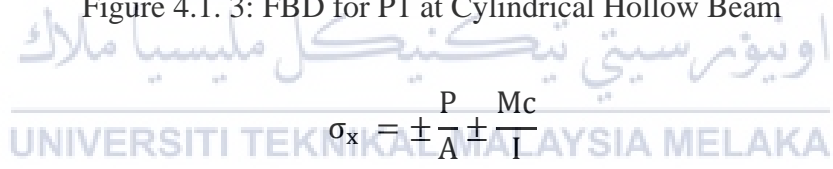


Figure 4.1. 3: FBD for P1 at Cylindrical Hollow Beam



$$\sigma_x = \pm \frac{P}{A} \pm \frac{Mc}{I}$$

Based on the FBD, normal stress is neglected for stress x. Then,

$$\sigma_x = -\frac{M_1 c}{I_{cyl}} - \frac{M_2 c}{I_{cyl}}$$

(negative bending stress because the point of interest in compression state by the moment)

$$M_1 = R_1 x_1$$

$$R_1 = 20637.18 \text{ N}, \quad x_1 = 215 \text{ mm}$$

$$M_1 = (20637.18)(215) = 4436993.7 \text{ Nmm}$$

$$M_2 = R_2 x_2$$

$$R_2 = 4362.82 \text{ N}, \quad x_2 = 1447 \text{ mm}$$

$$M_2 = (4362.82)(1447) = 6313000.54 \text{ Nmm}$$

$$c = 82.55 \text{ mm} \quad I_{cyl} = 4542579 \text{ mm}^4$$

$$\sigma_x = -\frac{(4436993.7)(82.55)}{4542579} - \frac{(6313000.54)(82.55)}{4542579} = -195.35 \text{ MPa}$$

$$\tau_{xy} = \pm \frac{VQ}{It} \pm \frac{Tc}{J}$$

$$\tau_{xy} = 0$$

Shear stress has zero value since the shear force is applied on the same axis of the point of interest, which $Q=Ay$, y has zero value. For the torsional, stress can be neglected since there is no torsion occurring based on the FBD.

$$\sigma_{ave} = \frac{195.35 + 0}{2} = 97.68 \text{ MPa}$$

$$R = 97.68 \text{ MPa}$$

$$\sigma_1 = 195.35 \text{ MPa}$$

$$\sigma_2 = 0$$

$$\tau_{max} = R$$

Using Von Mises Theory,

$$\sigma' = 195.35 \text{ MPa}$$

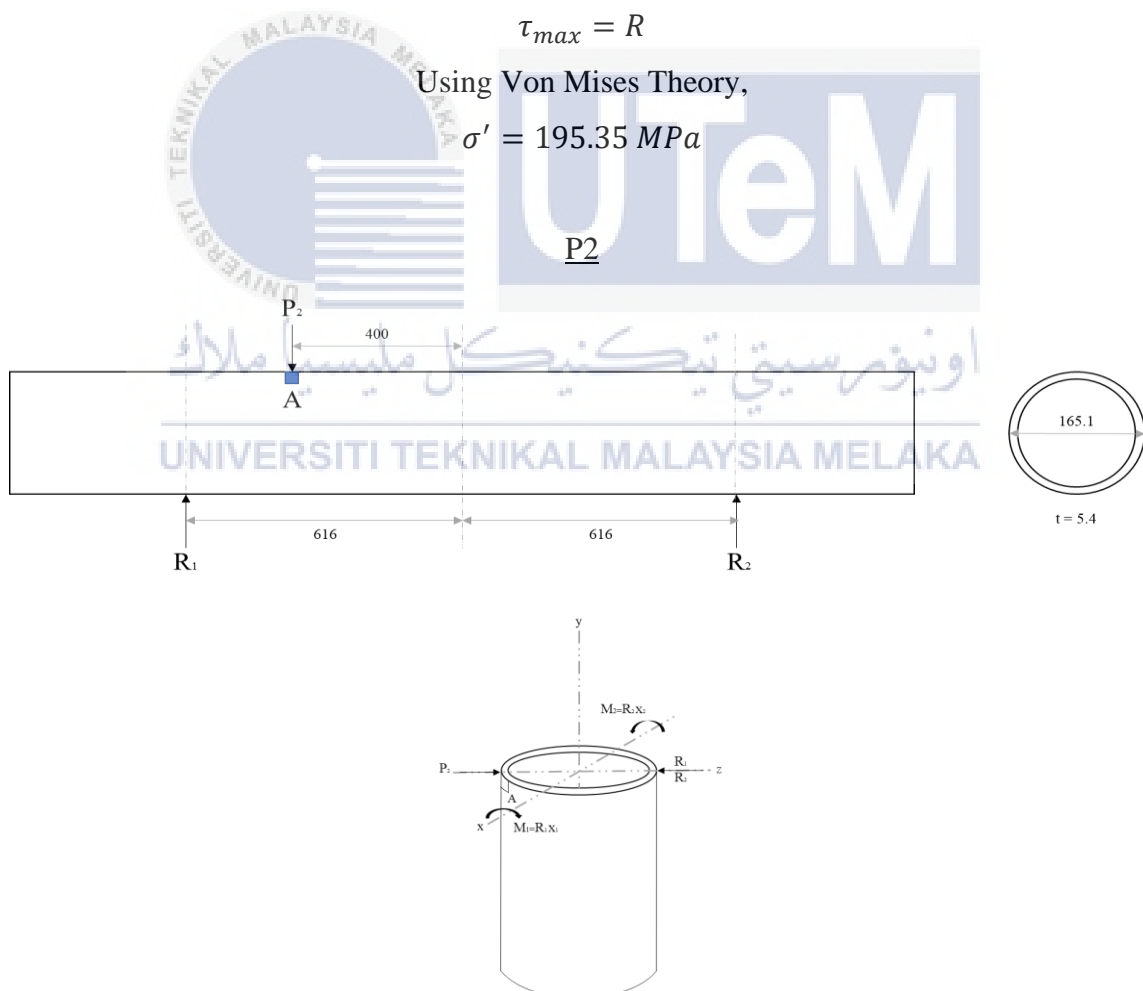


Figure 4.1. 4: FBD for P2 at Cylindrical Hollow Beam

$$\sigma_x = \pm \frac{P}{A} \pm \frac{Mc}{I}$$

Based on the FBD, normal stress is neglected for stress x. Then,

$$\sigma_x = \frac{M_1 c}{I_{cyl}} - \frac{M_2 c}{I_{cyl}}$$

(negative bending stress because the point of interest in compression state by the moment and vice versa)

$$M_1 = R_1 x_1$$

$$R_1 = 82467 \text{ N}, \quad x_1 = 216 \text{ mm}$$

$$M_1 = (82467)(216) = 17812872 \text{ Nmm}$$

$$M_2 = R_2 x_2$$

$$R_2 = 17532.47 \text{ N}, \quad x_2 = 1016 \text{ mm}$$

$$M_2 = (17532.47)(1016) = 17812989.52 \text{ Nmm}$$

$$c = 82.55 \text{ mm} \quad I_{cyl} = 4542579 \text{ mm}^4$$

$$\sigma_x = \frac{(17812872)(82.55)}{4542579} - \frac{(17812989.52)(82.55)}{4542579} = 323.70 \text{ MPa}$$

$$\tau_{xy} = \pm \frac{VQ}{It} \pm \frac{Tc}{J}$$

$$\tau_{xy} = 0$$

Shear stress has zero value since the shear force is applied on the same axis of the point of interest, which $Q=Ay$, y has zero value. For the torsional, stress can be neglected since there is no torsion occurring based on the FBD.

$$\sigma_{ave} = \frac{323.70 + 0}{2} = 161.85 \text{ MPa}$$

$$R = 161.85 \text{ MPa}$$

$$\sigma_1 = 323.70 \text{ MPa}$$

$$\sigma_2 = 0$$

$$\tau_{max} = R$$

Using Von Mises Theory,

$$\sigma' = 323.70 \text{ MPa}$$

P3

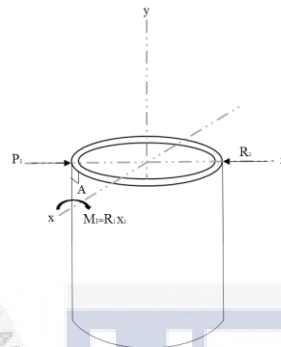
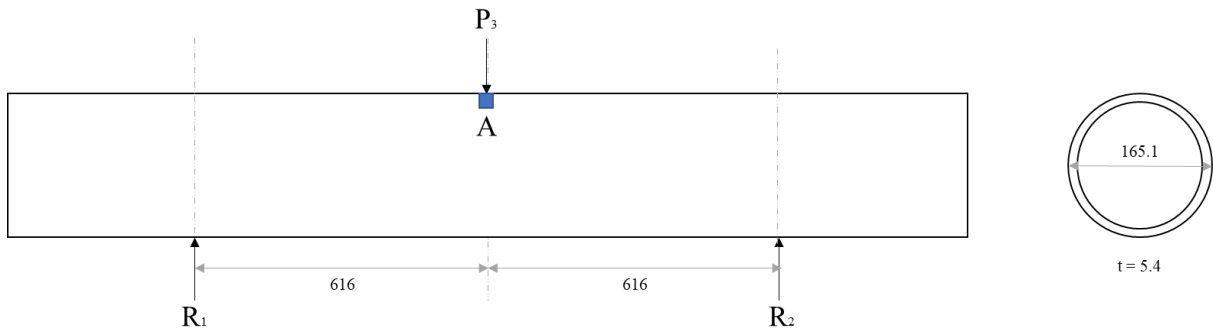


Figure 4.1. 5: FBD for P3 at Cylindrical Hollow Beam

$$\sigma_x = \pm \frac{P}{A} \pm \frac{Mc}{I}$$

Based on the FBD, normal stress is neglected for stress x. Then,

$$\sigma_x = \frac{M_1 c}{I_{cyl}}$$

(negative bending stress because the point of interest in compression state by the moment and vice versa)

$$M_1 = R_1 x_1$$

$$R_1 = 12500 \text{ N}, \quad x_1 = 616 \text{ mm}$$

$$M_1 = (12500)(616) = 7700000 \text{ Nmm}$$

$$c = 82.55 \text{ mm} \quad I_{cyl} = 4542579 \text{ mm}^4$$

$$\sigma_x = \frac{(7700000)(82.55)}{4542579} = 139.93 \text{ MPa}$$

$$\tau_{xy} = \pm \frac{VQ}{It} \pm \frac{Tc}{J}$$

$$\tau_{xy} = 0$$

Shear stress has zero value since the shear force is applied on the same axis of the point of interest, which $Q=Ay$, y has zero value. For the torsional, stress can be neglected since there is no torsion occurring based on the FBD.

$$\sigma_{ave} = \frac{139.93 + 0}{2} = 69.96 \text{ MPa}$$

$$R = 69.96 \text{ MPa}$$

$$\sigma_1 = 139.93 \text{ MPa}$$

$$\sigma_2 = 0$$

$$\tau_{max} = R$$

Using Von Mises Theory,

$$\sigma' = 139.93 \text{ MPa}$$

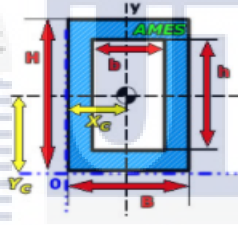


i. Rectangular Hollow Beam

INPUT PARAMETERS		Value	
Height [H]	<input type="text" value="150"/>	mm	mm
Width [B]	<input type="text" value="100"/>		
Internal height [h]	<input type="text" value="138"/>		
Internal width [b]	<input type="text" value="88"/>		
Length [L]	<input type="text" value="2215"/>		
Density [p]	<input type="text" value="7.87"/>	g/cm ³	

Parameter	Value	Unit
Cross section area (A)	28.56	cm ²
Mass (M)	49.786	kg
Second moment of area (I _{xx})	8852472	mm ⁴
Second moment of area (I _{yy})	4663072	mm ⁴
Section modulus (S _{xx})	118032.961	mm ³
Section modulus (S _{yy})	93261.438	mm ³
Radius of gyration (r _x)	55.674	mm
Radius of gyration (r _y)	40.407	mm
CoG distance in x direction (x _{cog})	50	mm
CoG distance in y direction (y _{cog})	75	mm

Hollow Rectangle Formulas:



Parameter	Symbol	Equation
Cross section area	A	$A = BH - bh$
Area moment of inertia	I_{xx}	$I_{xx} = BH^3/12 - bh^3/12$
Area moment of inertia	I_{yy}	$I_{yy} = HB^3/12 - hb^3/12$
Section modulus	S_{xx}	$S_{xx} = I_{xx}/y_{cog}$
Section modulus	S_{yy}	$S_{yy} = I_{yy}/x_{cog}$
Centroid	x_c	$x_c = B/2$
Centroid	y_c	$y_c = H/2$
Mass	M	$M = AL\rho$
Radius of gyration	r	$r = (I/A)^{0.5}$

Figure 4.1. 6: Properties of Rectangular Hollow Beam

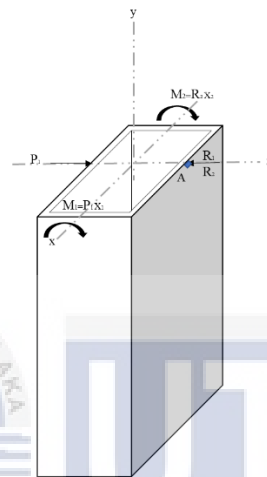
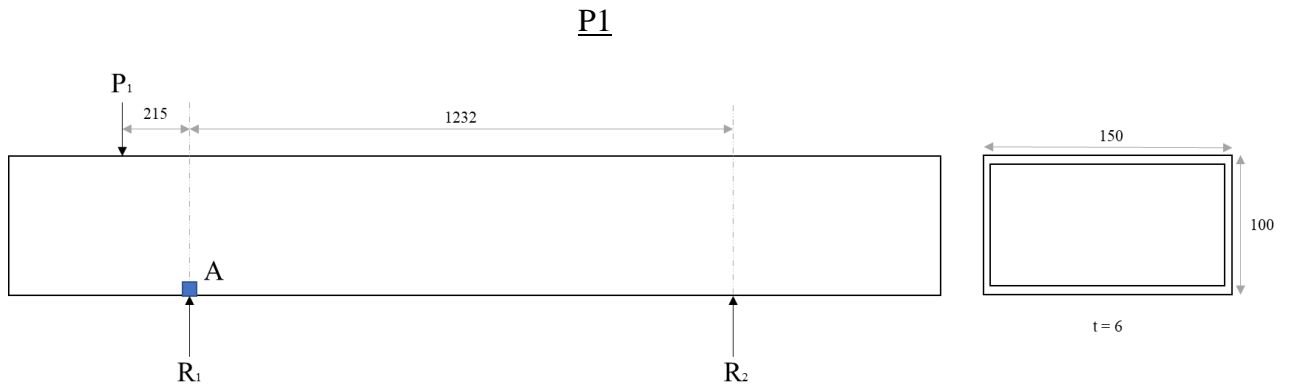


Figure 4.1. 7: FBD for P1 at Rectangular Hollow Beam

$$\sigma_x = \pm \frac{P}{A} \pm \frac{Mc}{I}$$

Based on the FBD, normal stress is neglected for stress x. Then,

$$\sigma_x = -\frac{M_1 c}{I_{zz}} - \frac{M_2 c}{I_{zz}}$$

(negative bending stress because the point of interest in compression state by the moment)

$$M_1 = P_1 x_1$$

$$P_1 = 25000 \text{ N}, \quad x_1 = 215 \text{ mm}$$

$$M_1 = (25000)(215) = 5375000 \text{ Nmm}$$

$$M_2 = R_2 x_2$$

$$R_2 = 4362.82 \text{ N}, \quad x_2 = 1232 \text{ mm}$$

$$M_2 = (4362.82)(1232) = 5374994.24 \text{ Nmm}$$

$$c = 50 \text{ mm} \quad I_{zz} = 8852472 \text{ mm}^4$$

$$\sigma_x = -\frac{(5375000)(50)}{8852472} - \frac{(5374994.24)(50)}{8852472} = -60.77 \text{ MPa}$$

$$\tau_{xy} = \pm \frac{VQ}{It} \pm \frac{Tc}{J}$$

$$\tau_{xy} = 0$$

Shear stress has zero value since the shear force is applied on the same axis of the point of interest, which $Q=Ay$, y has zero value. For the torsional, stress can be neglected since there is no torsion occurring based on the FBD.

$$\sigma_{ave} = \frac{60.77 + 0}{2} = 30.385 \text{ MPa}$$

$$R = 30.385 \text{ MPa}$$

$$\sigma_1 = 60.77 \text{ MPa}$$

$$\sigma_2 = 0$$

$$\tau_{max} = R$$

Using Von Mises Theory,

$$\sigma' = 60.77 \text{ MPa}$$

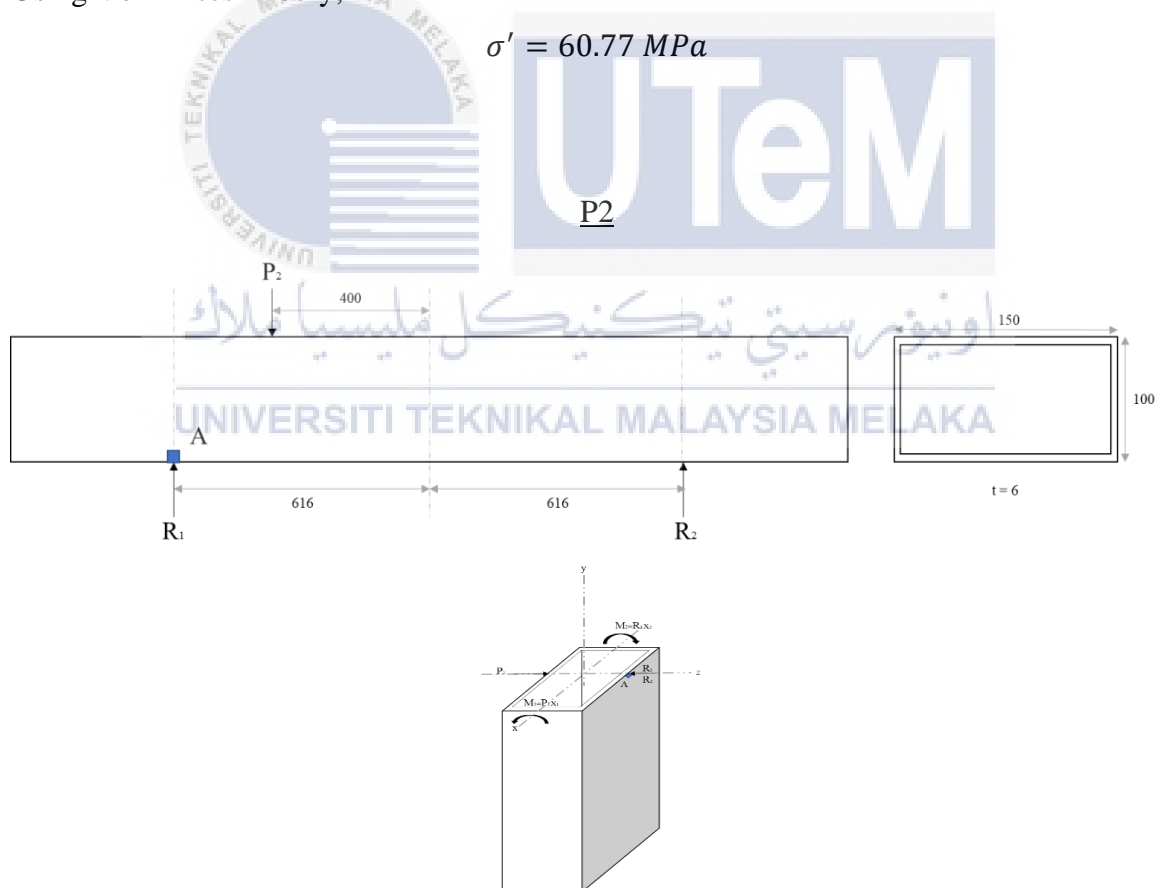


Figure 4.1. 8: FBD for P2 at Rectangular Hollow Beam

$$\sigma_x = \pm \frac{P}{A} \pm \frac{Mc}{I}$$

Based on the FBD, normal stress is neglected for stress x. Then,

$$\sigma_x = \frac{M_1 c}{I_{zz}} - \frac{M_2 c}{I_{zz}}$$

(negative bending stress because the point of interest in compression state by the moment and vice versa)

$$M_1 = P_1 x_1$$

$$P_1 = 100000 \text{ N}, \quad x_1 = 216 \text{ mm}$$

$$M_1 = (100000)(216) = 21600000 \text{ Nmm}$$

$$M_2 = R_2 x_2$$

$$R_2 = 17532.47 \text{ N}, \quad x_2 = 1232 \text{ mm}$$

$$M_2 = (17532.47)(1232) = 21600003.04 \text{ Nmm}$$

$$c = 50 \text{ mm} \quad I_{zz} = 8852472 \text{ mm}^4$$

$$\sigma_x = -\frac{(21600000)(50)}{8852472} - \frac{(21600003.04)(50)}{8852472} = -122 \text{ MPa}$$

$$\tau_{xy} = \pm \frac{VQ}{It} \pm \frac{Tc}{J}$$

$$\tau_{xy} = 0$$

Shear stress has zero value since the shear force is applied on the same axis of the point of interest, which $Q=Ay$, y has zero value. For the torsional, stress can be neglected since there is no torsion occurring based on the FBD.

$$\sigma_{ave} = \frac{122 + 0}{2} = 61 \text{ MPa}$$

$$R = 61 \text{ MPa}$$

$$\sigma_1 = 122 \text{ MPa}$$

$$\sigma_2 = 0$$

$$\tau_{max} = R$$

Using Von Mises Theory,

$$\sigma' = 122 \text{ MPa}$$

P3

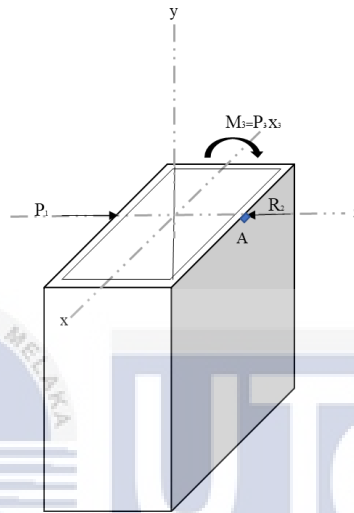
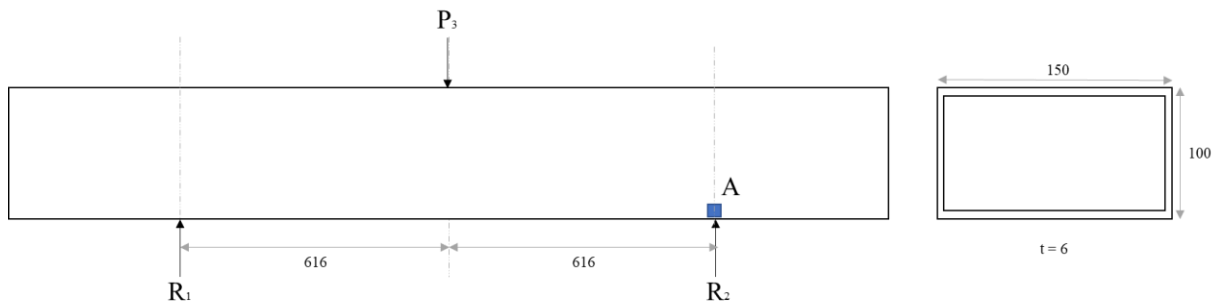


Figure 4.1. 9: FBD for P3 at Rectangular Hollow Beam

$$\sigma_x = \pm \frac{P}{A} \pm \frac{Mc}{I}$$

Based on the FBD, normal stress is neglected for stress x. Then,

$$\sigma_x = -\frac{M_3 c}{I_{zz}}$$

(negative bending stress because the point of interest in compression state by the moment)

$$M_3 = P_3 x_3$$

$$P_3 = 25000 \text{ N}, \quad x_3 = 616 \text{ mm}$$

$$M_3 = (25000)(616) = 15400000 \text{ Nmm}$$

$$c = 50 \text{ mm} \quad I_{zz} = 8852472 \text{ mm}^4$$

$$\sigma_x = -\frac{(15400000)(50)}{8852472} = -86.98 \text{ MPa}$$

$$\tau_{xy} = \pm \frac{VQ}{It} \pm \frac{Tc}{J}$$

$$\tau_{xy} = 0$$

Shear stress has zero value since the shear force is applied on the same axis of the point of interest, which $Q=Ay$, y has zero value. For the torsional, stress can be neglected since there is no torsion occurring based on the FBD.

$$\sigma_{ave} = \frac{86.98 + 0}{2} = 43.49 \text{ MPa}$$

$$R = 43.49 \text{ MPa}$$

$$\sigma_1 = 86.98 \text{ MPa}$$

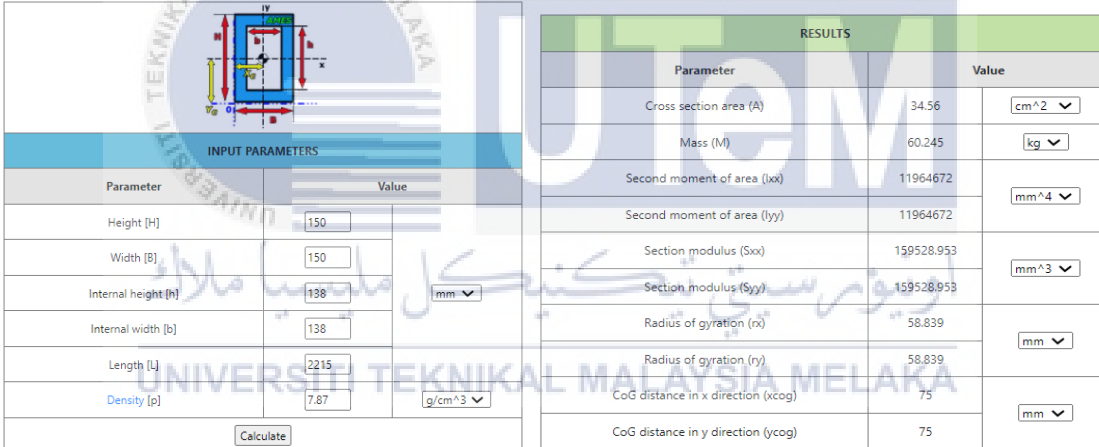
$$\sigma_2 = 0$$

$$\tau_{max} = R$$

Using Von Mises Theory,

$$\sigma' = 86.98 \text{ MPa}$$

ii. Square Hollow Beam



INPUT PARAMETERS		
Parameter	Value	
Height [H]	150	
Width [B]	150	
Internal height [h]	138	mm
Internal width [b]	138	
Length [L]	2215	
Density [ρ]	7.87	g/cm ³
Calculate		

RESULTS		
Parameter	Value	
Cross section area (A)	34.56	cm ²
Mass (M)	60.245	kg
Second moment of area (I _{xx})	11964672	
Second moment of area (I _{yy})	11964672	mm ⁴
Section modulus (S _{xx})	159528.953	
Section modulus (S _{yy})	159528.953	mm ³
Radius of gyration (r _x)	58.839	
Radius of gyration (r _y)	58.839	mm
CoG distance in x direction (xcog)	75	
CoG distance in y direction (ycog)	75	mm

Figure 4.1. 10: Properties of Square Hollow Beam

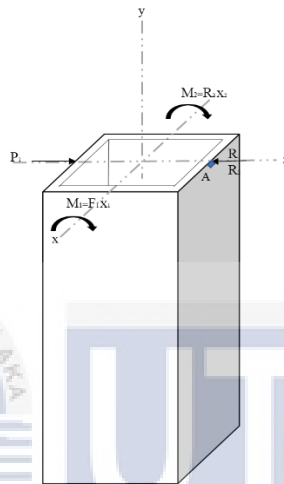
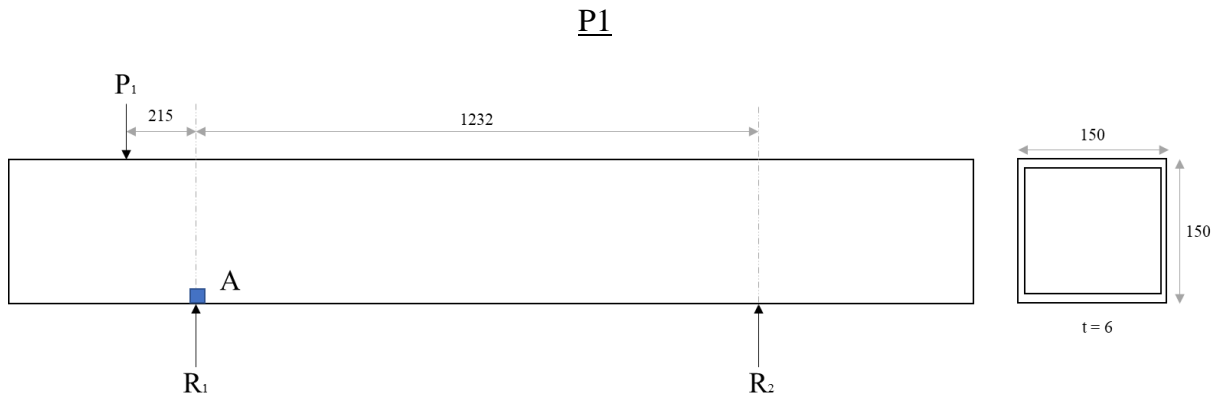


Figure 4.1. 11: FBD for P1 at Square Hollow Beam

$$\sigma_x = \pm \frac{P}{A} \pm \frac{Mc}{I}$$

Based on the FBD, normal stress is neglected for stress x. Then,

$$\sigma_x = -\frac{M_1 c}{I_{zz}} - \frac{M_2 c}{I_{zz}}$$

(negative bending stress because the point of interest in compression state by the moment)

$$M_1 = P_1 x_1$$

$$P_1 = 25000 \text{ N}, \quad x_1 = 215 \text{ mm}$$

$$M_1 = (25000)(215) = 5375000 \text{ Nmm}$$

$$M_2 = R_2 x_2$$

$$R_2 = 4362.82 \text{ N}, \quad x_2 = 1232 \text{ mm}$$

$$M_2 = (4362.82)(1232) = 5374994.24 \text{ Nmm}$$

$$c = 75 \text{ mm} \quad I_{zz} = 11964672 \text{ mm}^4$$

$$\sigma_x = -\frac{(5375000)(75)}{11964672} - \frac{(5374994.24)(75)}{11964672} = -67.39 \text{ MPa}$$

$$\tau_{xy} = \pm \frac{VQ}{It} \pm \frac{Tc}{J}$$

$$\tau_{xy} = 0$$

Shear stress has zero value since the shear force is applied on the same axis of the point of interest, which $Q=Ay$, y has zero value. For the torsional, stress can be neglected since there is no torsion occurring based on the FBD.

$$\sigma_{ave} = \frac{67.39 + 0}{2} = 33.695 \text{ MPa}$$

$$R = 33.695 \text{ MPa}$$

$$\sigma_1 = 67.39 \text{ MPa}$$

$$\sigma_2 = 0$$

$$\tau_{max} = R$$

Using Von Mises Theory,

$$\sigma' = 67.39 \text{ MPa}$$

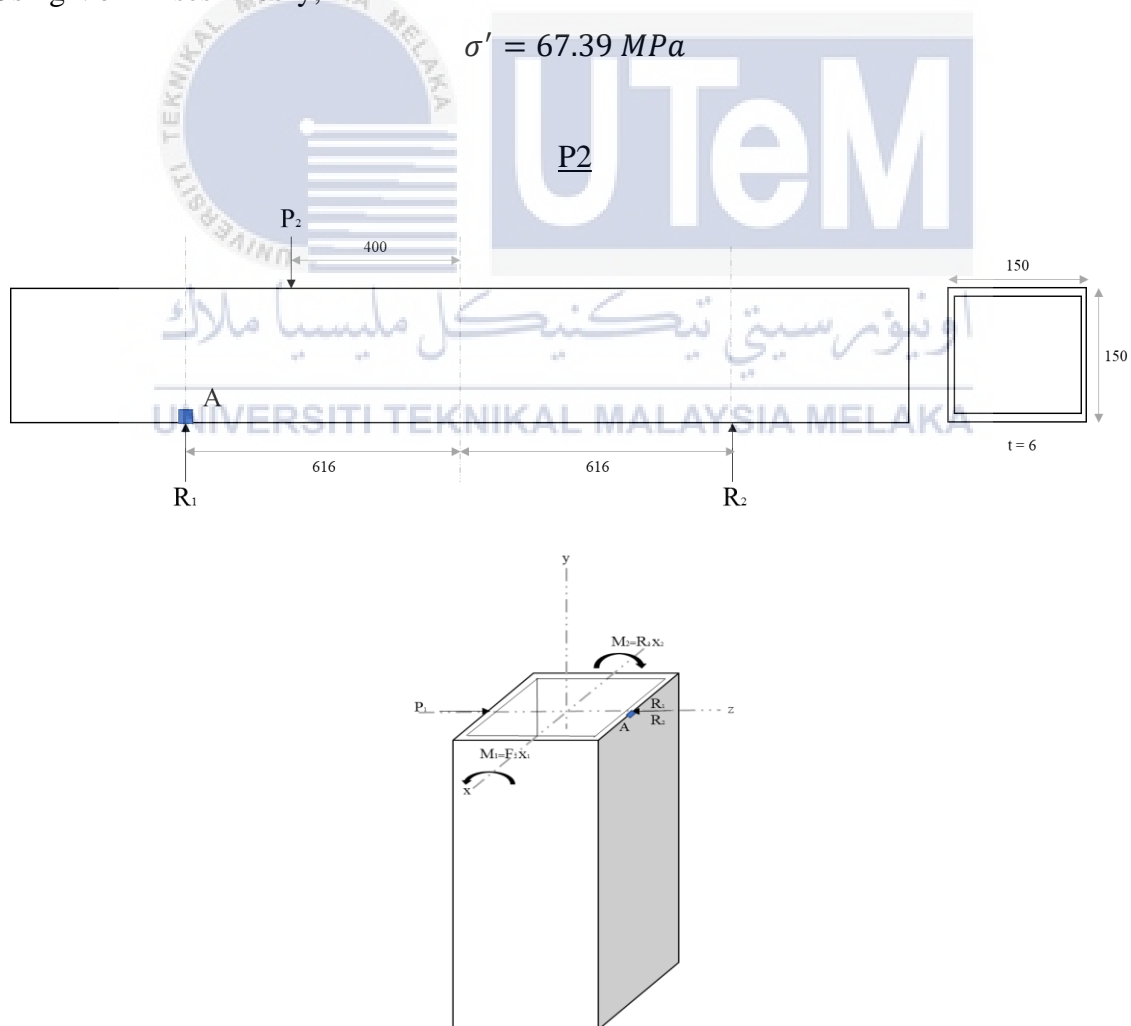


Figure 4.1. 12: FBD for P2 at Square Hollow Beam

$$\sigma_x = \pm \frac{P}{A} \pm \frac{Mc}{I}$$

Based on the FBD, normal stress is neglected for stress x. Then,

$$\sigma_x = \frac{M_1 c}{I_{zz}} - \frac{M_2 c}{I_{zz}}$$

(negative bending stress because the point of interest in compression state by the moment and vice versa)

$$M_1 = P_1 x_1$$

$$P_1 = 100000 \text{ N}, \quad x_1 = 216 \text{ mm}$$

$$M_1 = (100000)(216) = 21600000 \text{ Nmm}$$

$$M_2 = R_2 x_2$$

$$R_2 = 17532.47 \text{ N}, \quad x_2 = 1232 \text{ mm}$$

$$M_2 = (17532.47)(1232) = 21600003.04 \text{ Nmm}$$

$$c = 75 \text{ mm} \quad I_{zz} = 11964672 \text{ mm}^4$$

$$\sigma_x = -\frac{(21600000)(75)}{11964672} - \frac{(21600003.04)(75)}{11964672} = -135.40 \text{ MPa}$$

$$\tau_{xy} = \pm \frac{VQ}{It} \pm \frac{Tc}{J}$$

$$\tau_{xy} = 0$$

Shear stress has zero value since the shear force is applied on the same axis of the point of interest, which $Q=Ay$, y has zero value. For the torsional, stress can be neglected since there is no torsion occurring based on the FBD.

$$\sigma_{ave} = \frac{135.4 + 0}{2} = 67.7 \text{ MPa}$$

$$R = 67.7 \text{ MPa}$$

$$\sigma_1 = 135.4 \text{ MPa}$$

$$\sigma_2 = 0$$

$$\tau_{max} = R$$

Using Von Mises Theory,

$$\sigma' = 135.4 \text{ MPa}$$

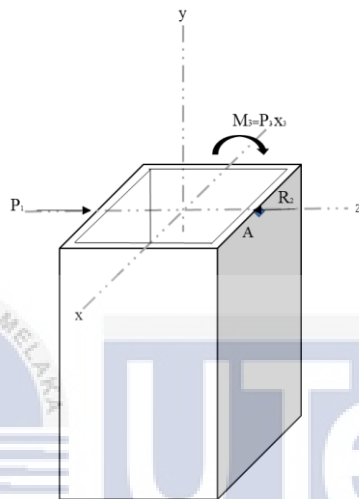
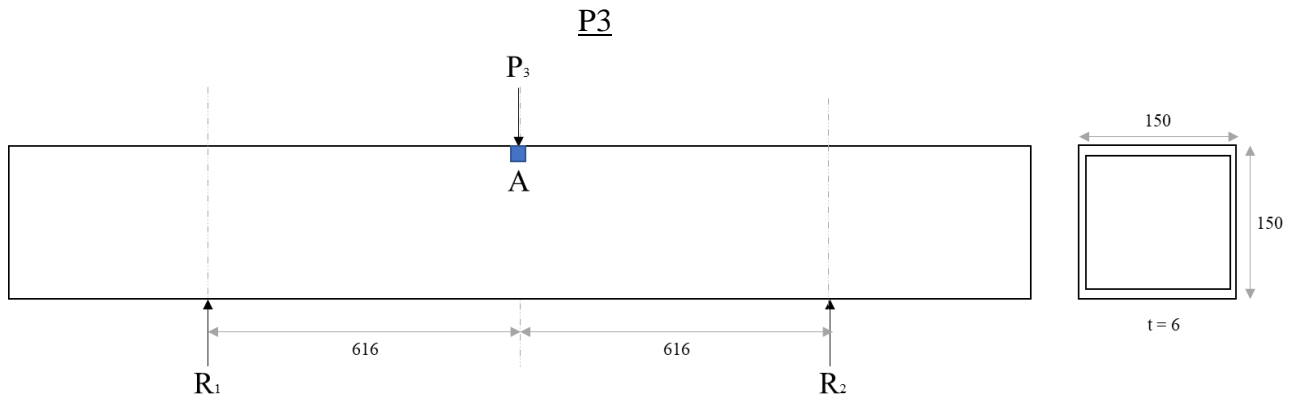


Figure 4.1. 13: FBD for P3 at Square Hollow Beam

$$\sigma_x = \pm \frac{P}{A} \pm \frac{Mc}{I}$$

Based on the FBD, normal stress is neglected for stress x . Then,

$$\sigma_x = -\frac{M_3 c}{I_{zz}}$$

(negative bending stress because the point of interest in compression state by the moment)

$$M_3 = P_3 x_3$$

$$P_3 = 25000 \text{ N}, \quad x_3 = 616 \text{ mm}$$

$$M_3 = (25000)(616) = 15400000 \text{ Nmm}$$

$$c = 75 \text{ mm} \quad I_{zz} = 11964672 \text{ mm}^4$$

$$\sigma_x = -\frac{(15400000)(75)}{11964672} = -96.53 \text{ MPa}$$

$$\tau_{xy} = \pm \frac{VQ}{It} \pm \frac{Tc}{J}$$

$$\tau_{xy} = 0$$

Shear stress has zero value since the shear force is applied on the same axis of the point of interest, which $Q=Ay$, y has zero value. For the torsional, stress can be neglected since there is no torsion occurring based on the FBD.

$$\sigma_{ave} = \frac{96.53 + 0}{2} = 48.27 \text{ MPa}$$

$$R = 48.27 \text{ MPa}$$

$$\sigma_1 = 96.53 \text{ MPa}$$

$$\sigma_2 = 0$$

$$\tau_{max} = R$$

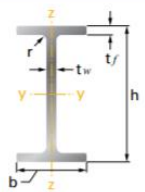
Using Von Mises Theory,

$$\sigma' = 96.43 \text{ MPa}$$

iii. I-Beam

5 Sizes and Section Properties

Wide Flange Shapes (JIS G 3192 Metric Series)



Nominal Size	Section Dimensions (mm)						Area of Section (cm ²)	Mass per Metre (kg/m)	Second Moment of Area (cm ⁴)		Elastic Modulus (cm ³)		Plastic Modulus (cm ³)	
	h x b	h	b	t _w	t _f	r			Axis y-y I _y	Axis z-z I _z	Axis y-y Wel. y	Axis z-z Wel. z	Axis y-y Wpl. y	Axis z-z Wpl. z
300 x 150	300	150	6.5	9	13	46.78	36.7	7,210	508	481	67.7	542	105	
*298	149	5.5	8	13	40.80	32.0	6,320	442	424	59.3	475	91.8		

Figure 4.1. 14: Properties of W-Beam

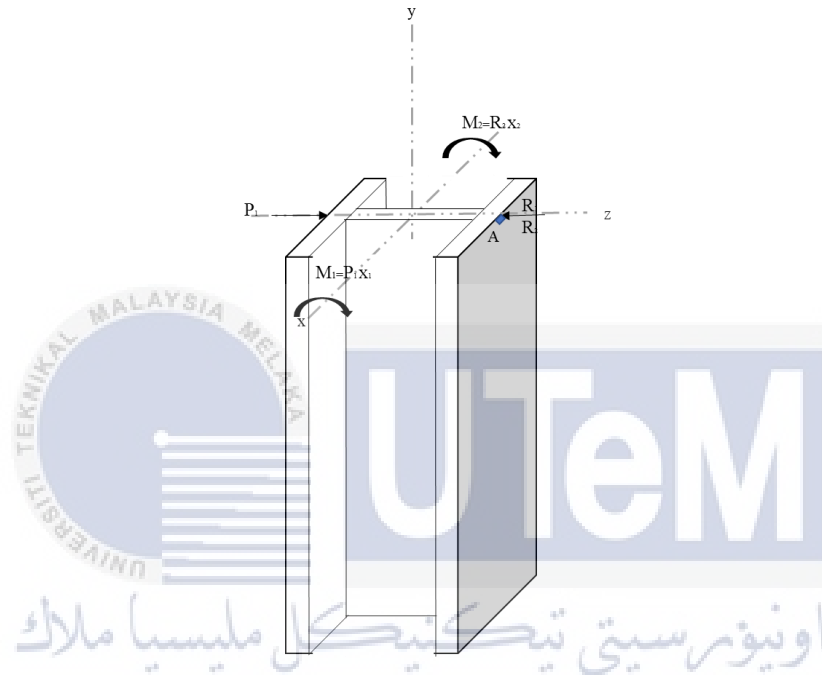
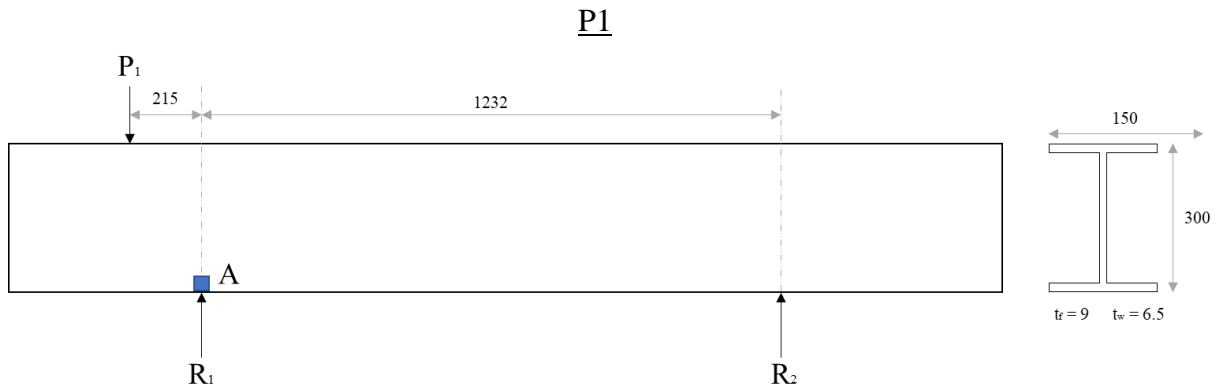


Figure 4.1. 15: FBD for P1 at W-Beam

$$\sigma_x = \pm \frac{P}{A} \pm \frac{Mc}{I}$$

Based on the FBD, normal stress is neglected for stress x. Then,

$$\sigma_x = -\frac{M_1 c}{I_{yy}} - \frac{M_2 c}{I_{yy}}$$

(negative bending stress because the point of interest in compression state by the moment)

$$M_1 = P_1 x_1$$

$$P_1 = 25000 \text{ N}, \quad x_1 = 215 \text{ mm}$$

$$M_1 = (25000)(215) = 5375000 \text{ Nmm}$$

$$M_2 = R_2 x_2$$

$$R_2 = 4362.82 \text{ N}, \quad x_2 = 1232 \text{ mm}$$

$$M_2 = (4362.82)(1232) = 5374994.24 \text{ Nmm}$$

$$c = 75 \text{ mm} \quad I_{yy} = 72100000 \text{ mm}^4$$

$$\sigma_x = -\frac{(5375000)(75)}{72100000} - \frac{(5374994.24)(75)}{72100000} = -11.182 \text{ MPa}$$

$$\tau_{xy} = \pm \frac{VQ}{It} \pm \frac{Tc}{J}$$

$$\tau_{xy} = 0$$

Shear stress has zero value since the shear force is applied on the same axis of the point of interest, which $Q=Ay$, y has zero value. For the torsional, stress can be neglected since there is no torsion occurring based on the FBD.

$$\sigma_{ave} = \frac{11.182 + 0}{2} = 5.591 \text{ MPa}$$

$$R = 5.591 \text{ MPa}$$

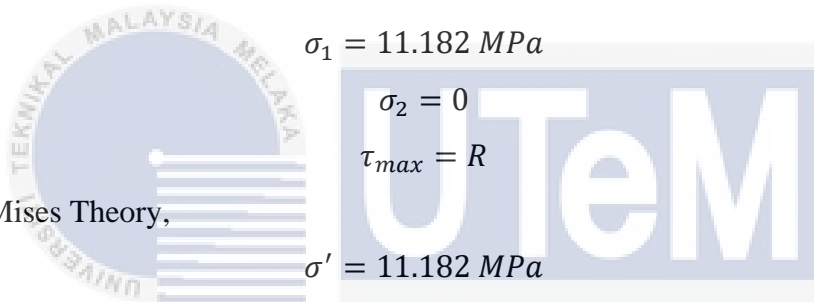
$$\sigma_1 = 11.182 \text{ MPa}$$

$$\sigma_2 = 0$$

$$\tau_{max} = R$$

$$\sigma' = 11.182 \text{ MPa}$$

Using Von Mises Theory,



اونيورسيتي تيكنيكل مليسيا ملاك

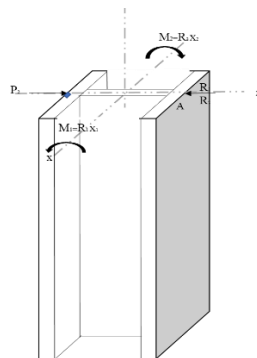
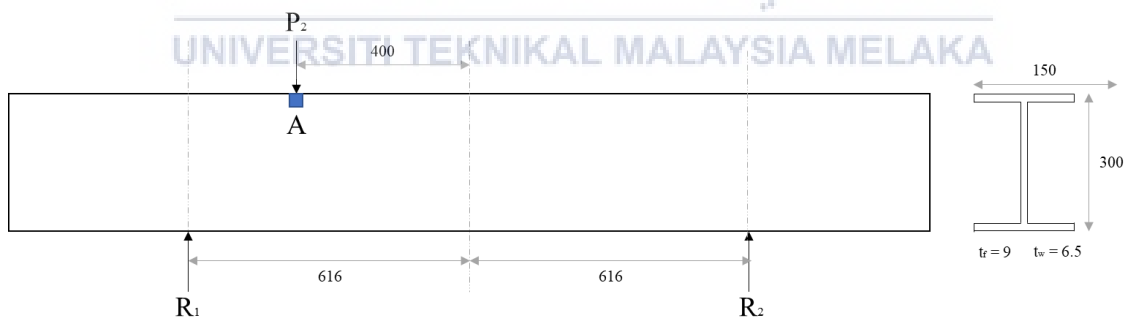


Figure 4.1. 16: FBD for P2 at W-Beam

$$\sigma_x = \pm \frac{P}{A} \pm \frac{Mc}{I}$$

Based on the FBD, normal stress is neglected for stress x. Then,

$$\sigma_x = -\frac{M_1 c}{I_{cyl}} + \frac{M_2 c}{I_{cyl}}$$

(negative bending stress because the point of interest in compression state by the moment and vice versa)

$$M_1 = R_1 x_1$$

$$R_1 = 82467.53 \text{ N}, \quad x_1 = 216 \text{ mm}$$

$$M_1 = (82467.53)(216) = 17812986.48 \text{ Nmm}$$

$$M_2 = R_2 x_2$$

$$R_2 = 17532.47 \text{ N}, \quad x_2 = 1232 \text{ mm}$$

$$M_2 = (17532.47)(1232) = 21600003.04 \text{ Nmm}$$

$$c = 75 \text{ mm} \quad I_{zz} = 8852472 \text{ mm}^4$$

$$\sigma_x = -\frac{(17812986.48)(75)}{8852472} + \frac{(21600003.04)(75)}{8852472} = -3.94 \text{ MPa}$$

$$\tau_{xy} = \pm \frac{VQ}{It} \pm \frac{Tc}{J}$$

$$\tau_{xy} = 0$$

Shear stress has zero value since the shear force is applied on the same axis of the point of interest, which $Q=Ay$, y has zero value. For the torsional, stress can be neglected since no torsion occurs based on the FBD.

$$\sigma_{ave} = \frac{3.94 + 0}{2} = 1.97 \text{ MPa}$$

$$R = 1.97 \text{ MPa}$$

$$\sigma_1 = 3.94 \text{ MPa}$$

$$\sigma_2 = 0$$

$$\tau_{max} = R$$

Using Von Mises Theory,

$$\sigma' = 3.94 \text{ MPa}$$

P3

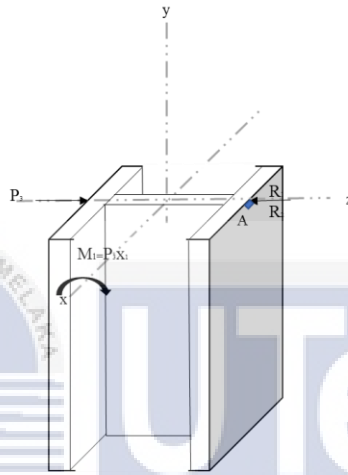
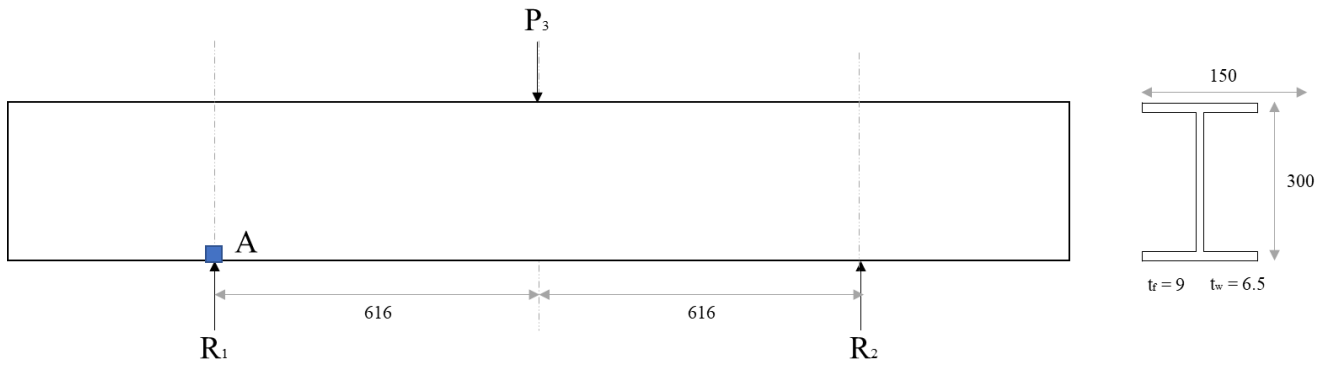


Figure 4.1. 17: FBD for P3 at W-Beam

$$\sigma_x = \pm \frac{P}{A} \pm \frac{Mc}{I}$$

Based on the FBD, normal stress is neglected for stress x. Then,

$$\sigma_x = -\frac{M_3 c}{I_{zz}}$$

(negative bending stress because the point of interest in compression state by the moment)

$$M_3 = P_3 x_3$$

$$P_3 = 25000 \text{ N}, \quad x_3 = 616 \text{ mm}$$

$$M_3 = (25000)(616) = 15400000 \text{ Nmm}$$

$$c = 75 \text{ mm} \quad I_{yy} = 76100000 \text{ mm}^4$$

$$\sigma_x = -\frac{(15400000)(75)}{76100000} = -15.18 \text{ MPa}$$

$$\tau_{xy} = \pm \frac{VQ}{It} \pm \frac{Tc}{J}$$

$$\tau_{xy} = 0$$

Shear stress has zero value since the shear force is applied on the same axis of the point of interest, which $Q=Ay$, y has zero value. For the torsional, stress can be neglected since there is no torsion occurring based on the FBD

$$\sigma_{ave} = \frac{15.18 + 0}{2} = 7.59 \text{ MPa}$$

$$R = 7.59 \text{ MPa}$$

$$\sigma_1 = 15.18 \text{ MPa}$$

$$\sigma_2 = 0$$

$$\tau_{max} = R$$

Using Von Mises Theory,

$$\sigma' = 15.18 \text{ MPa}$$

So, all the data comparisons of beam analysis are shown below.

Table 4.1. 2: Static Structural Analysis Data for Types of Beams

Type of Beam	P1=25kN		
	Manual Calculation	ANSYS	
	$\sigma_{VM}(\text{Mpa})$	$\sigma_{VM}(\text{MPa})$	$\delta(\text{mm})$
Cylindrical	195.35	102.94	0.3348
Rectangular	60.77	101.21	0.3346
Square	67.39	95.54	0.2240
W-shaped	11.182	36.35	0.0894
Type of Beam	P2=100kN		
	Manual Calculation	ANSYS	
	$\sigma_{VM}(\text{Mpa})$	$\sigma_{VM}(\text{MPa})$	$\delta(\text{mm})$
Cylindrical	323.7	359.61	0.9089
Rectangular	122	294.84	0.4867
Square	135.4	289.77	0.3898
W-shaped	3.94	124.96	0.2237

Table 4.1. 3: Static Structural Analysis Data for Types of Beams

Type of Beam	P3=25kN		
	Manual Calculation	ANSYS	
	σ_{VM} (Mpa)	σ_{VM} (MPa)	δ (mm)
Cylindrical	139.93	87.93	0.3133
Rectangular	86.98	73.07	0.3511
Square	96.53	70.62	0.2087
W-shaped	15.18	23.14	0.0887

With the data from static analysis recorded in Table 4.1.18 and 4.1.19, the data converted to the graph below to show more apparent on the comparison of stress Von-Mises from ANSYS with manual calculation and the deformation between deformation four types of beams from ANSYS.

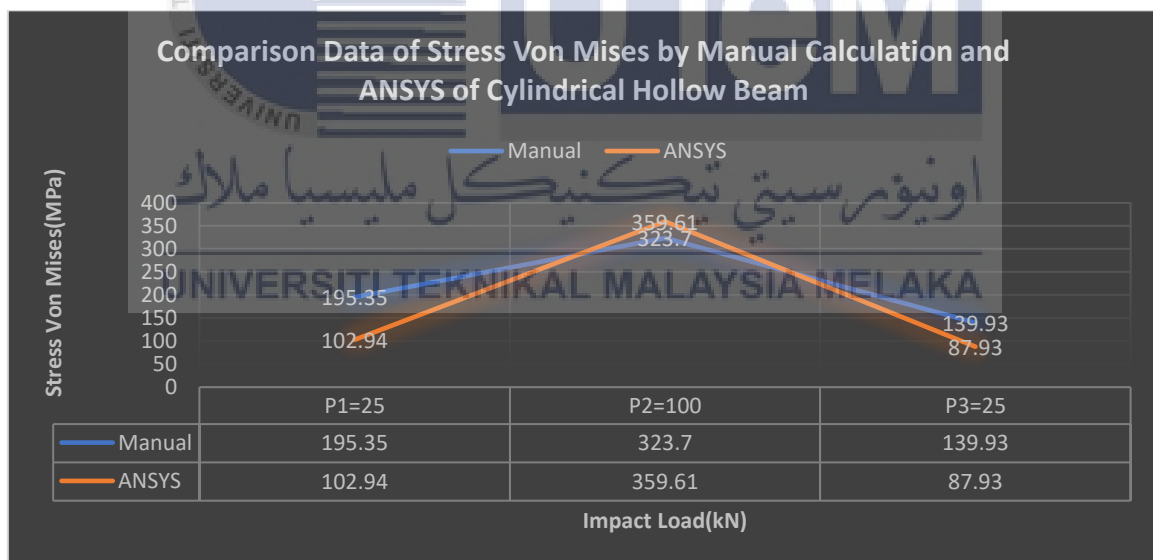


Figure 4.1. 18: Graph Comparison ANSYS and Manual Stress Von Mises of Cylindrical Hollow Beam

The above figure shows the data comparison of stress Von Mises from ANSYS and manual calculation. Three forces applied at different coordinates showed that both types of analysis at P2 give the highest stress than P1 and P3. At the same time, stress at P1 is higher than P3, where both also give the same result. Even though the value is different, the shape

of the data has the same pattern. For manual analysis, stress at P1 and P3 is higher than ANSYS, while vice versa for P2.

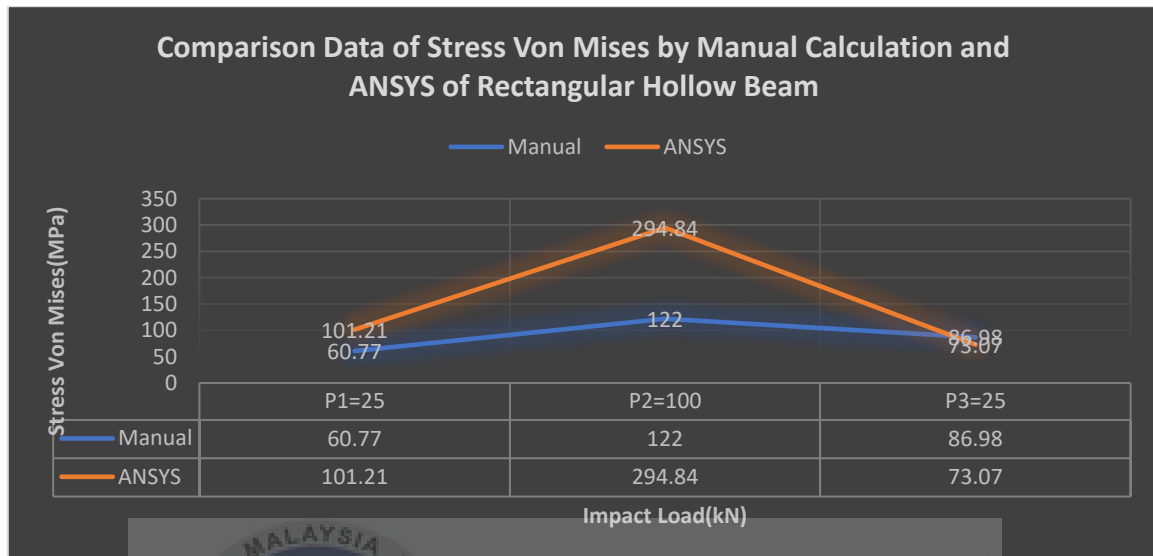


Figure 4.1. 19: Graph Comparison ANSYS and Manual Stress Von Mises of Rectangular Hollow Beam

Figure 4.1.19 illustrates the data shape for rectangular hollow beam analysis, which also shows the exact shape of data in which P2 has the highest stress Von Mises. However, the cylindrical hollow beam has higher maximum stress Von Mises than the rectangular hollow beam. For rectangular analysis, all the manual data is lower than data from ANSYS.

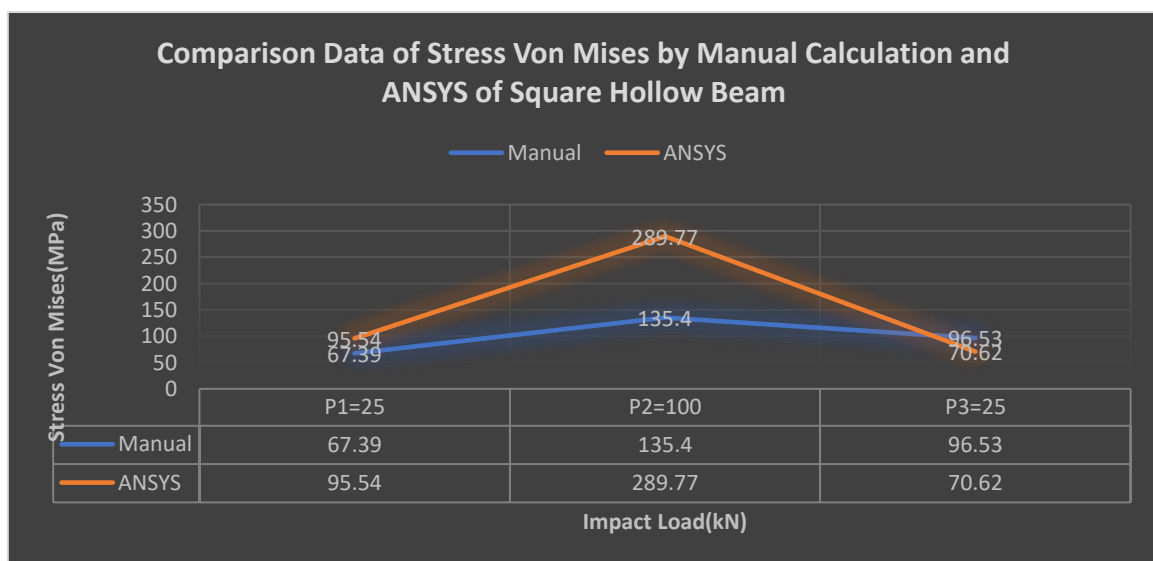


Figure 4.1. 20: Comparison ANSYS and Manual Stress Von Mises of Square Hollow Beam

The above figure compares the data analysis of hollow beams in maximum stress Von Mises. That data also showed different values but the same with the data shape. For P2 of both analyses is the highest maximum stress. For P2 and P3 of manual and ANSYS data have a different position.

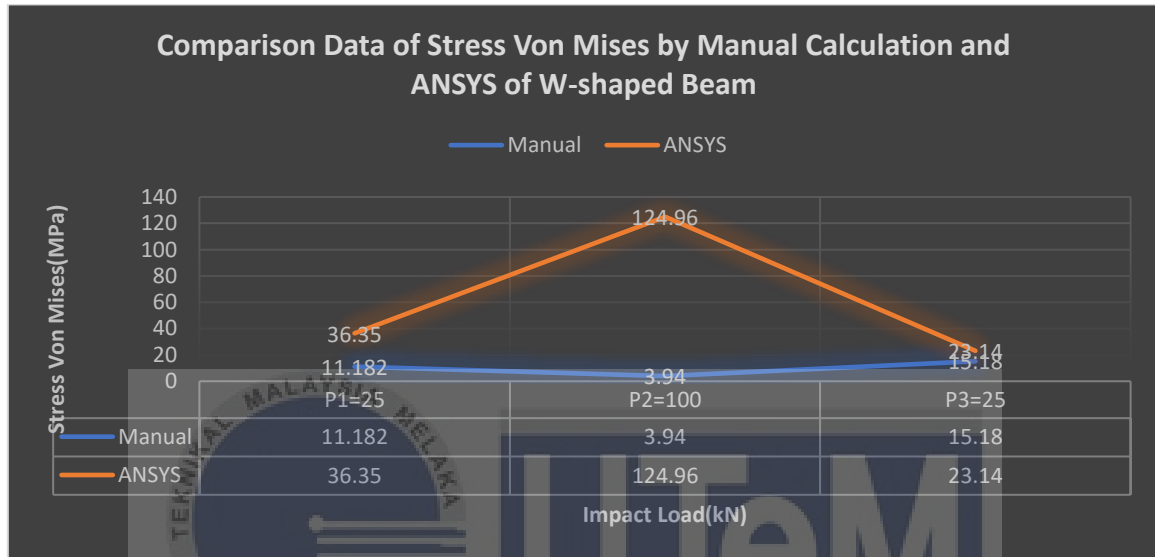


Figure 4.1. 21: Graph Comparison ANSYS and Manual Stress Von Mises of W-shaped Beam

Besides, the W-shaped beam has a different output of manual and ANSYS, which the P3 for ANSYS has the highest maximum stress but on the manual calculation at the lowest.

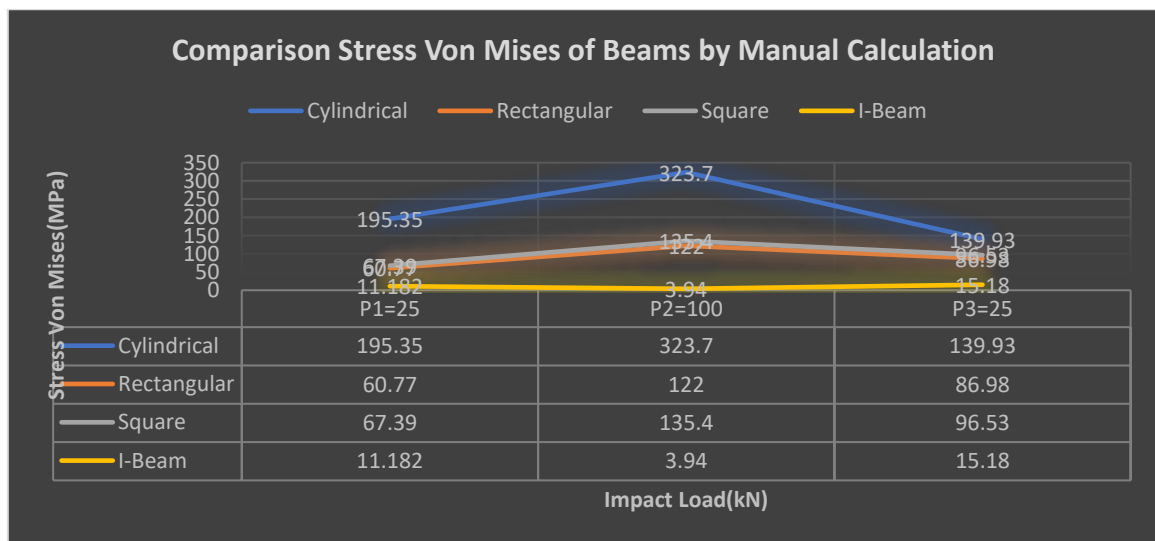


Figure 4.1. 22: Graph Comparison Manual Stress Von Mises of Four Types of Beams

On the manual calculation data, the cylindrical hollow beam shows the highest type of beam that can receive stress, then the square, rectangular and W-shaped beam. ANSYS data in Figure 4.1.22 also shows that cylindrical has the highest maximum Von-Mises than the other beams. While rectangular has the second-highest stress, then square and W-shaped accordingly.

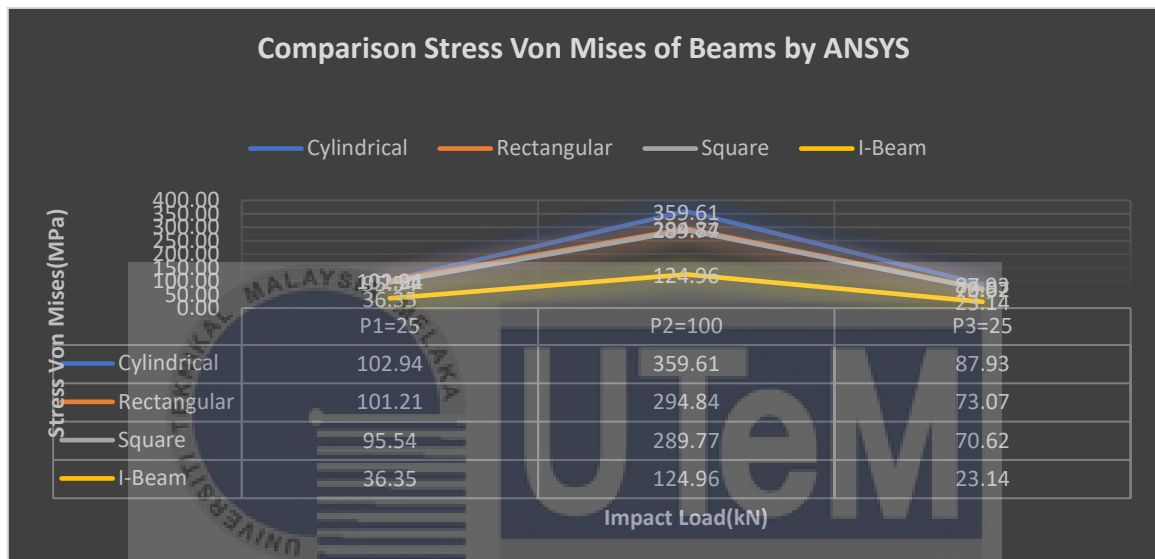


Figure 4.1. 23: Graph Comparison ANSYS Von Mises of Four Types of Beams

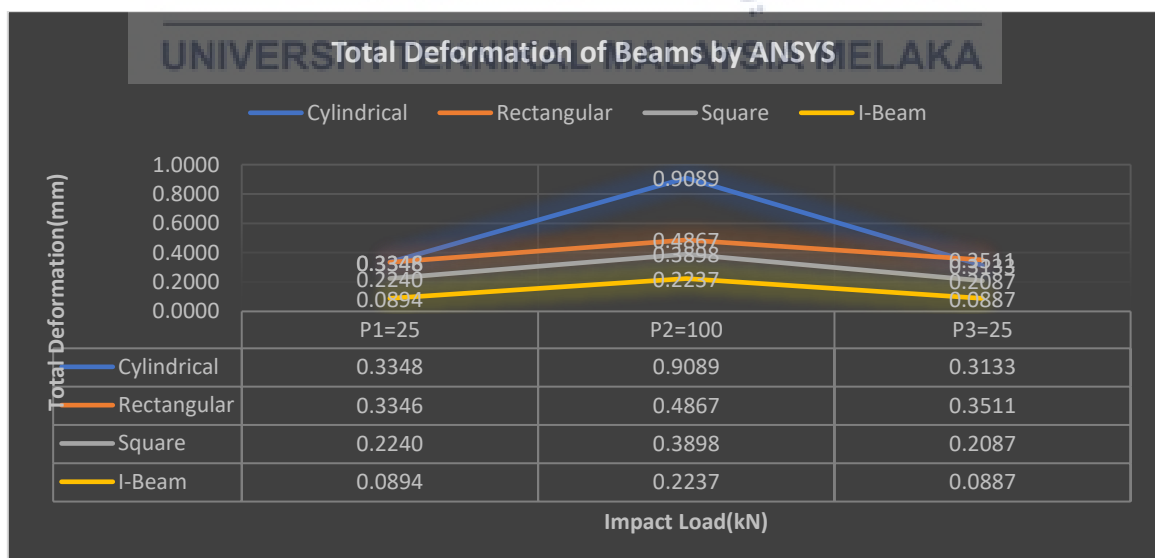


Figure 4.1. 24: Graph Comparison Total deformation of ANSYS for Four Types of Beams

For the deformation data of beams, cylindrical beams have the highest deformation than rectangular, square and W-shaped. Thus, the higher the maximum stress of a structure, the higher the deformation of the structure. For the overall analysis result, all the beams do not exceed the standard limit in terms of deformation.

4.1.2 Angle of Support Analysis

The support structure is a component that holds the underdrive protection beams. This study will discuss the angle of the support structure and the type of beams used for the support structure. First, to study the angle characteristic, the analysis angle of support will use a square hollow beam as constant then compare with different angles. After that, all types of beams also will be analysed with different angles of support to validate the result of the data output. Then, analyse the structure by changing the beams used for support with a constant support angle to choose the best support structure design. Total deformation (δ_T), equivalent stress (Von Mises) (σ_{VM}) strain energy (U) and safety factor (FS) is the output that will be observed in selecting the angle of support.

UNIVERSITI TEKNIKAL MALAYSIA MELAKA

4.1.2.1 Circular Hollow Beam with 15, 25 and 25 Degrees of Angle of Support

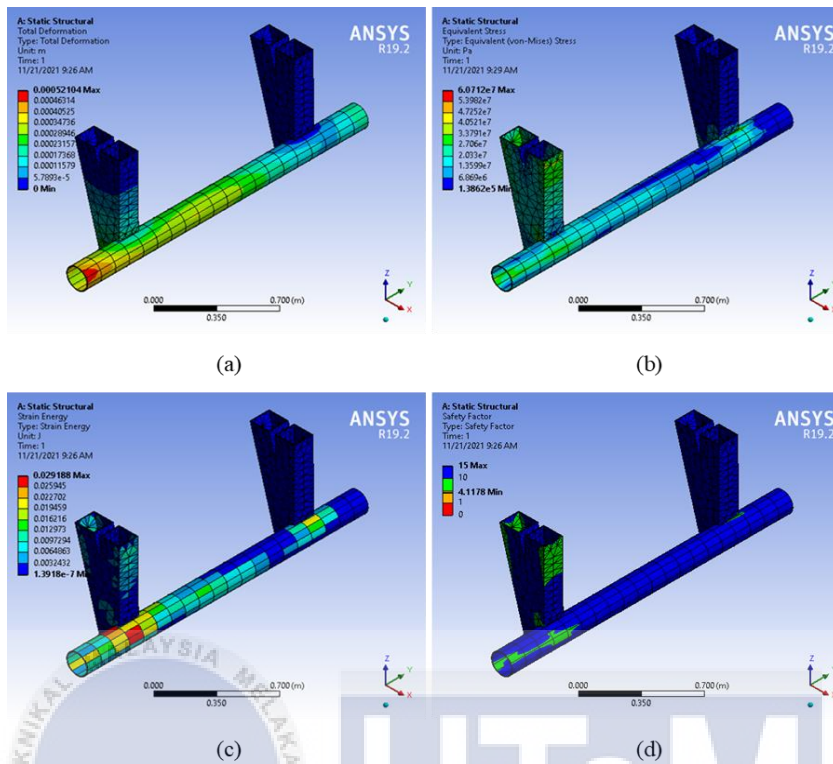


Figure 4.1. 25: Analysis P1 of Circular beam with 15-degree angles (a) Total Deformation (b) Maximum Stress Von Mises (c) Strain Energy (d) Factor of Safety

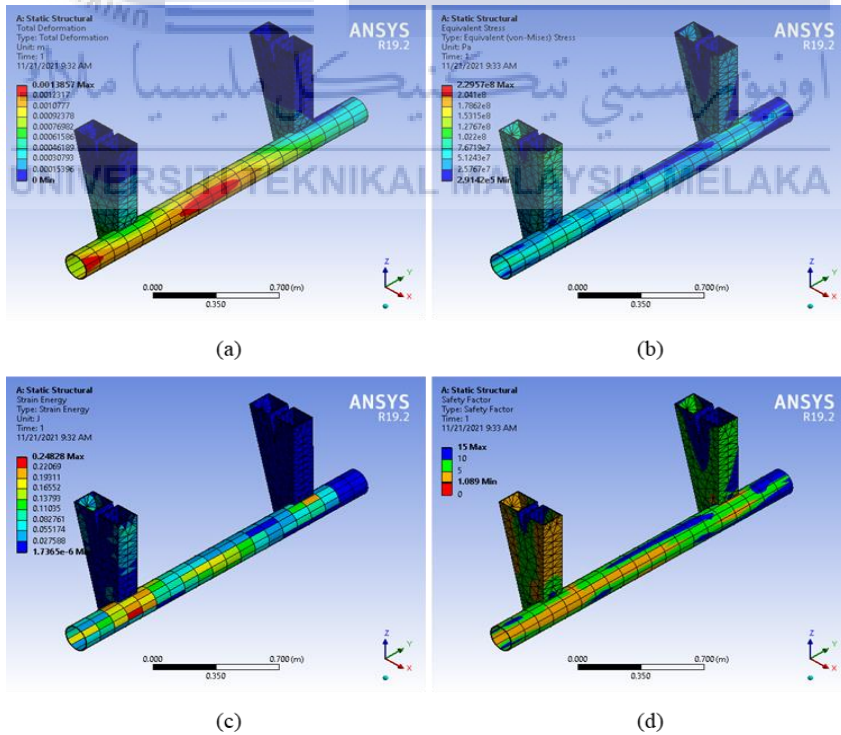


Figure 4.1. 26: Analysis P2 of Circular beam with 15-degree angles (a) Total Deformation (b) Maximum Stress Von Mises (c) Strain Energy (d) Factor of Safety

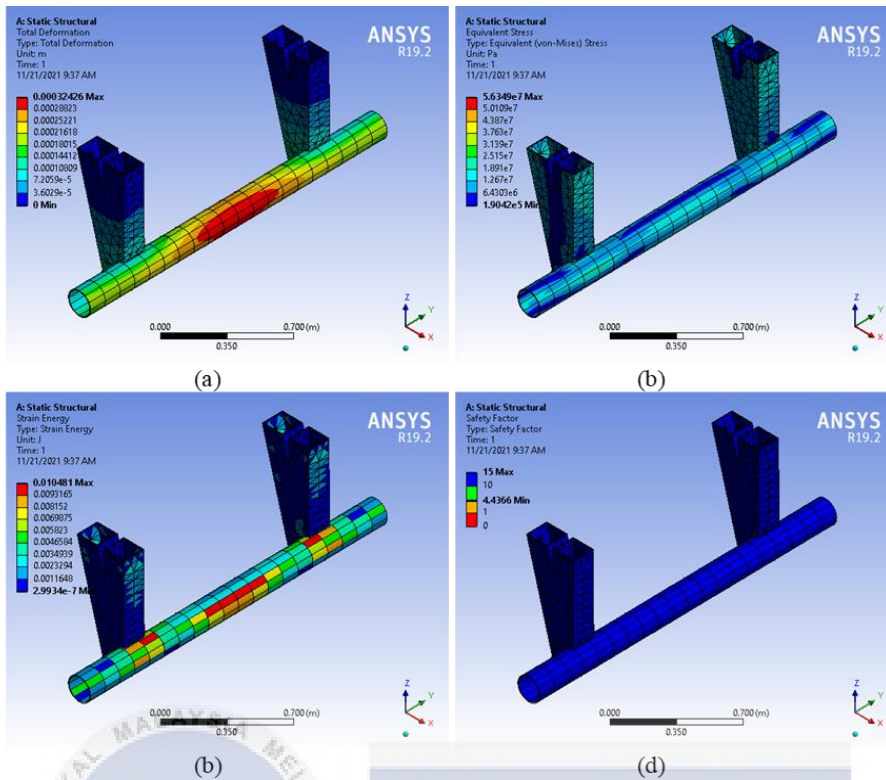


Figure 4.1. 27: Analysis P3 of Circular beam with 15-degree angle (a) Total Deformation (b) Maximum Stress Von Mises (c) Strain Energy (d) Factor of Safety

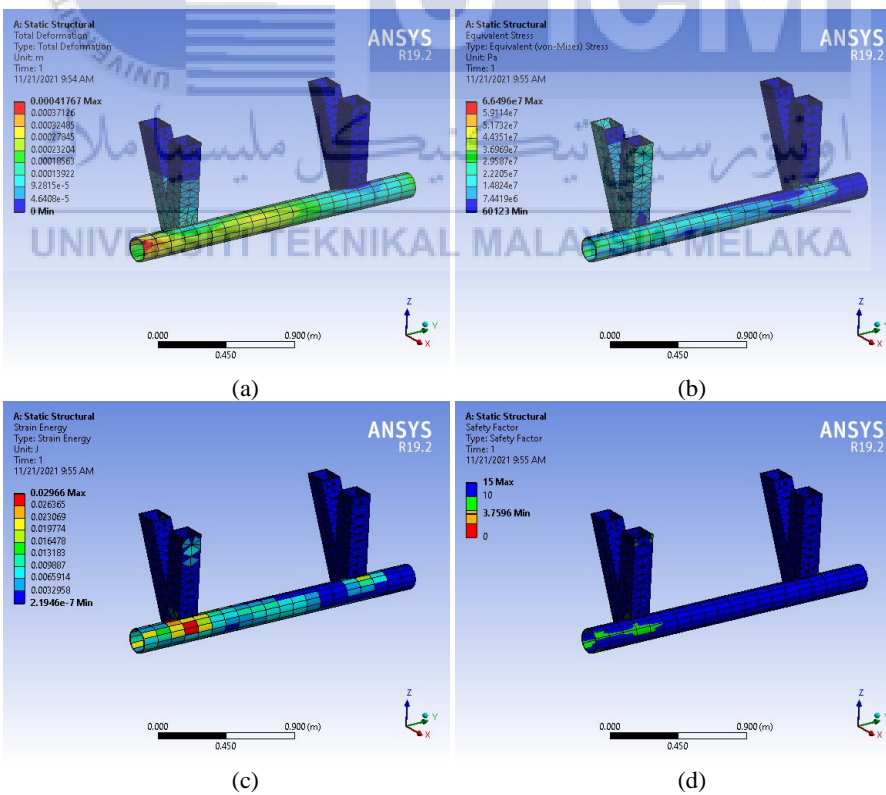


Figure 4.1. 28: Analysis P1 of Circular beam with 25-degree angles (a) Total Deformation (b) Maximum Stress Von Mises (c) Strain Energy (d) Factor of Safety

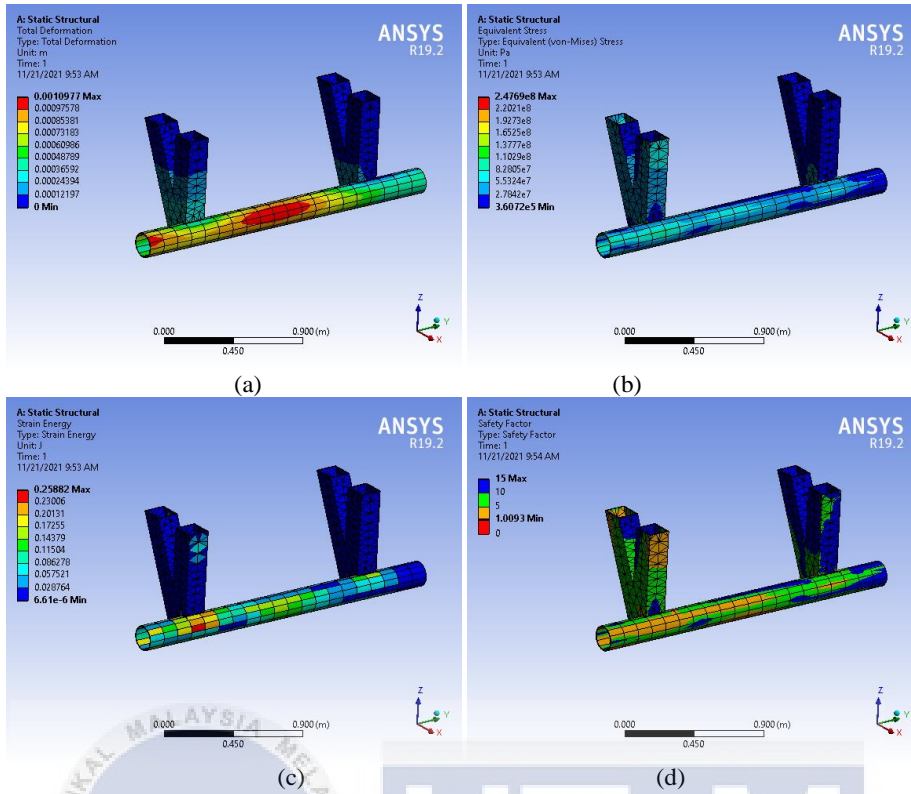


Figure 4.1. 29: Analysis P2 of Circular beam with 25-degree angle (a) Total Deformation (b) Maximum Stress Von Mises (c) Strain Energy (d) Factor of Safety

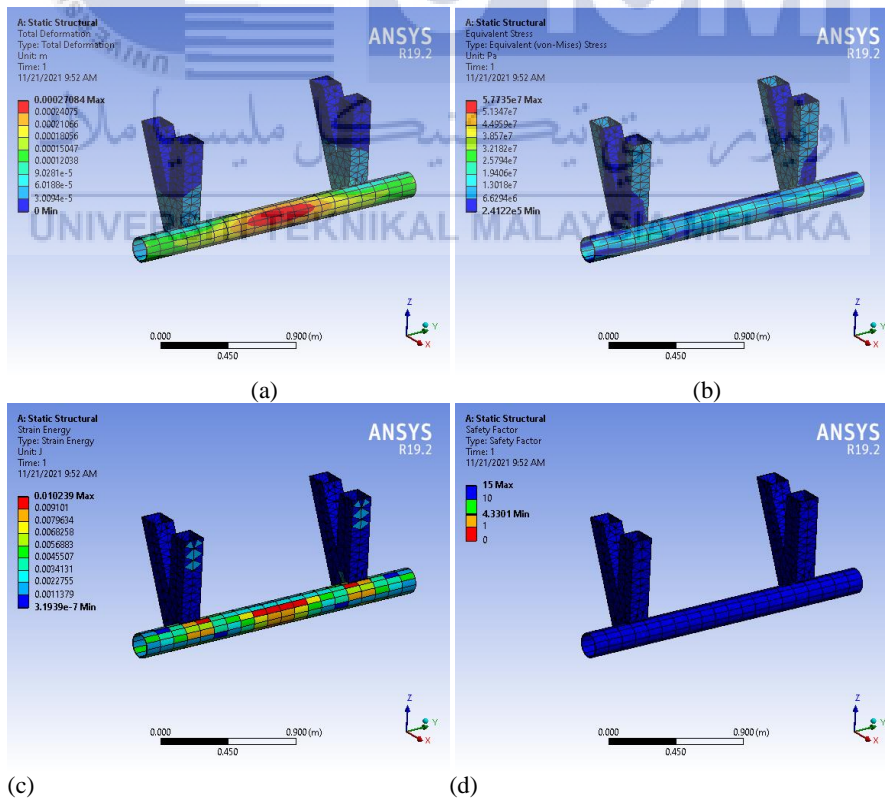


Figure 4.1. 30: Analysis P3 of Circular beam with 25-degree angle (a) Total Deformation (b) Maximum Stress Von Mises (c) Strain Energy (d) Factor of Safety

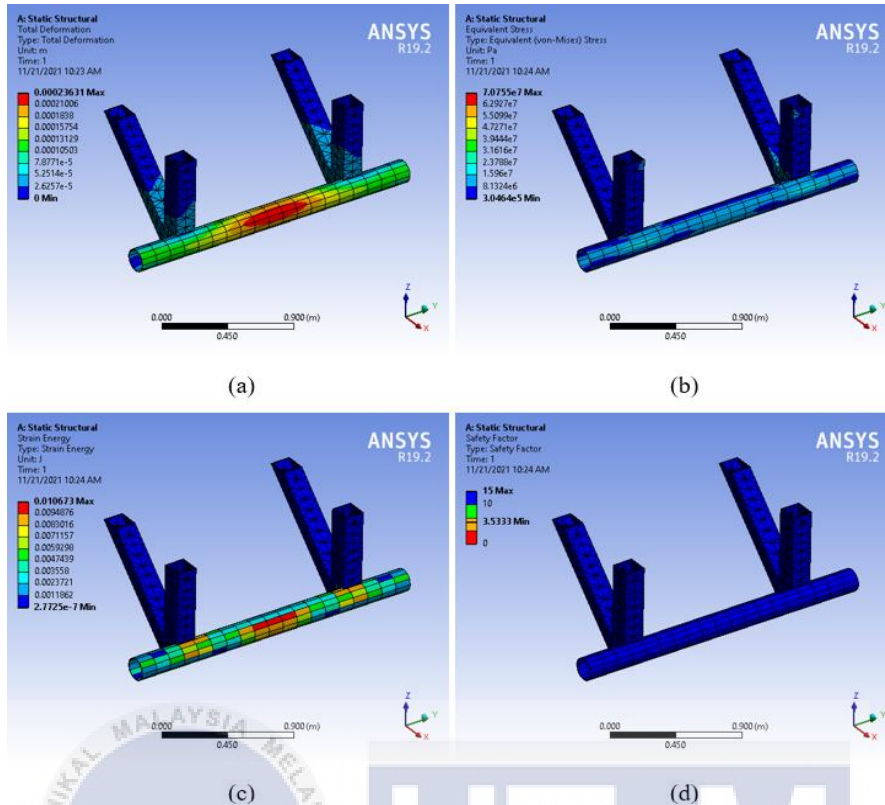


Figure 4.1. 31: Analysis P1 of Circular beam with 45-degree angle (a) Total Deformation (b) Maximum Stress Von Mises (c) Strain Energy (d) Factor of Safety

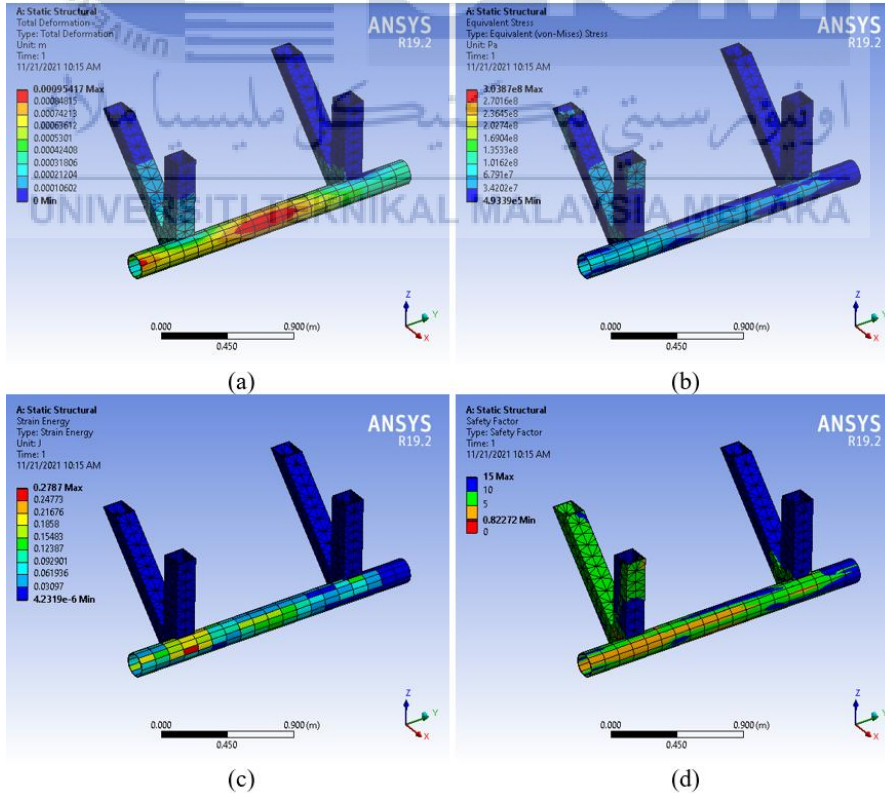


Figure 4.1. 32: Analysis P2 of Circular beam with 45-degree angle (a) Total Deformation (b) Maximum Stress Von Mises (c) Strain Energy (d) Factor of Safety

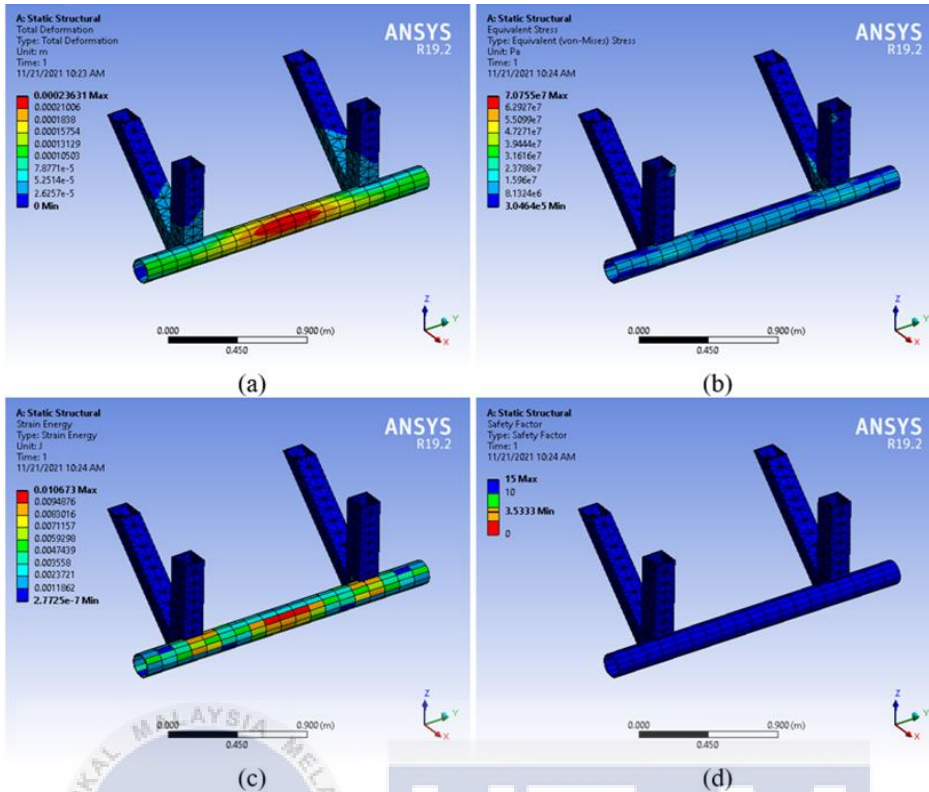


Figure 4.1. 33: Analysis P3 of Circular beam with 45-degree angle (a) Total Deformation (b) Maximum Stress Von Mises (c) Strain Energy (d) Factor of Safety

4.1.2.2 W-Beam beam with 15, 25 and 25 Degrees of Angle Support

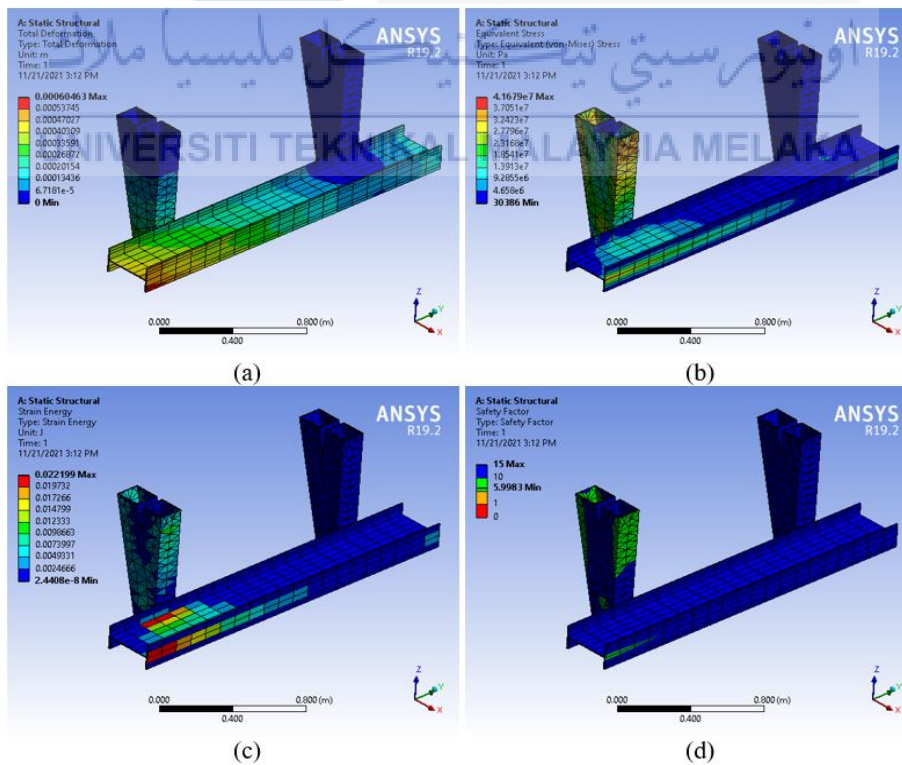


Figure 4.1. 34: Analysis P1 of W-beam with 15-degree angle (a) Total Deformation (b) Maximum Stress Von Mises (c) Strain Energy (d) Factor of Safety

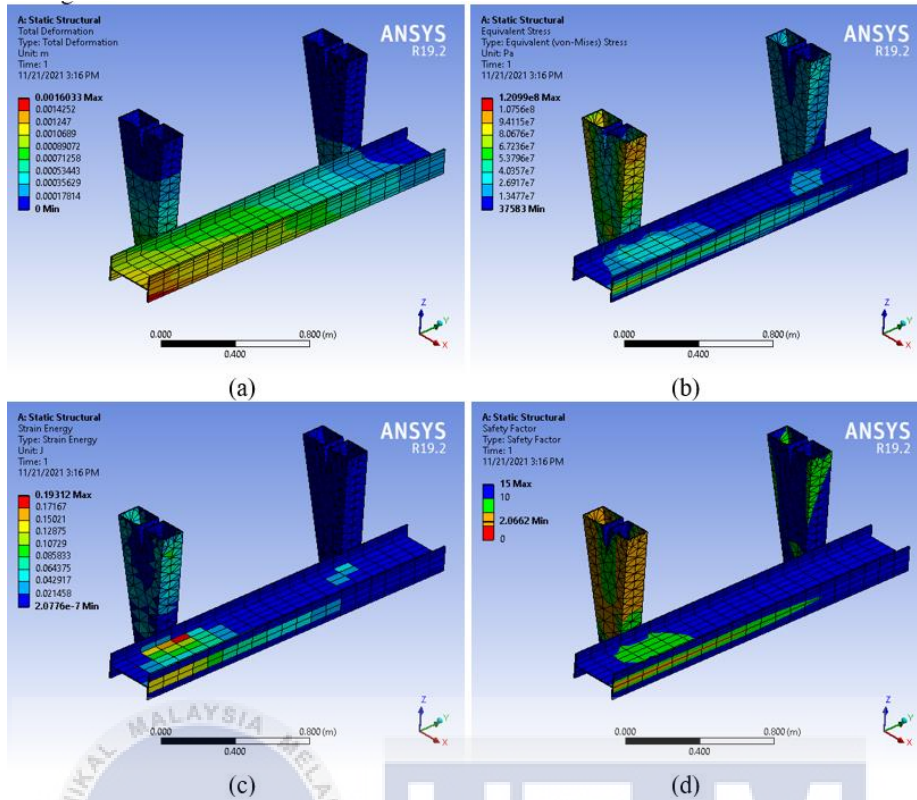


Figure 4.1. 35: Analysis P2 of W-beam with 15-degree angle (a) Total Deformation (b) Maximum Stress Von Mises (c) Strain Energy (d) Factor of Safety

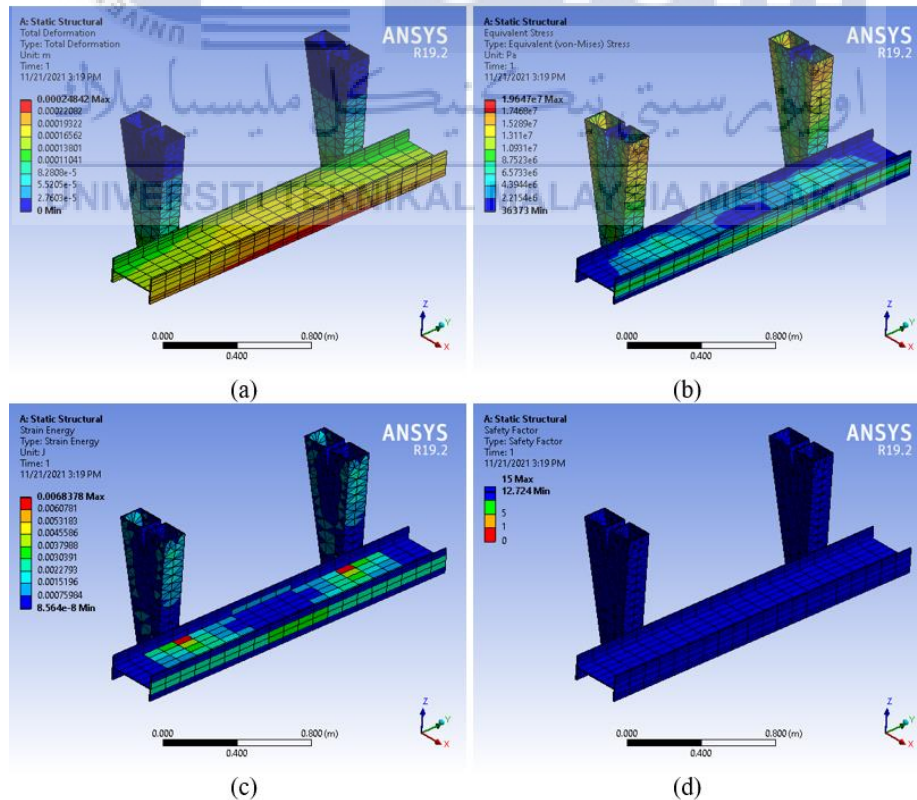


Figure 4.1. 36: Analysis P3 of W-beam with 15-degree angle (a) Total Deformation (b) Maximum Stress Von Mises (c) Strain Energy (d) Factor of Safety

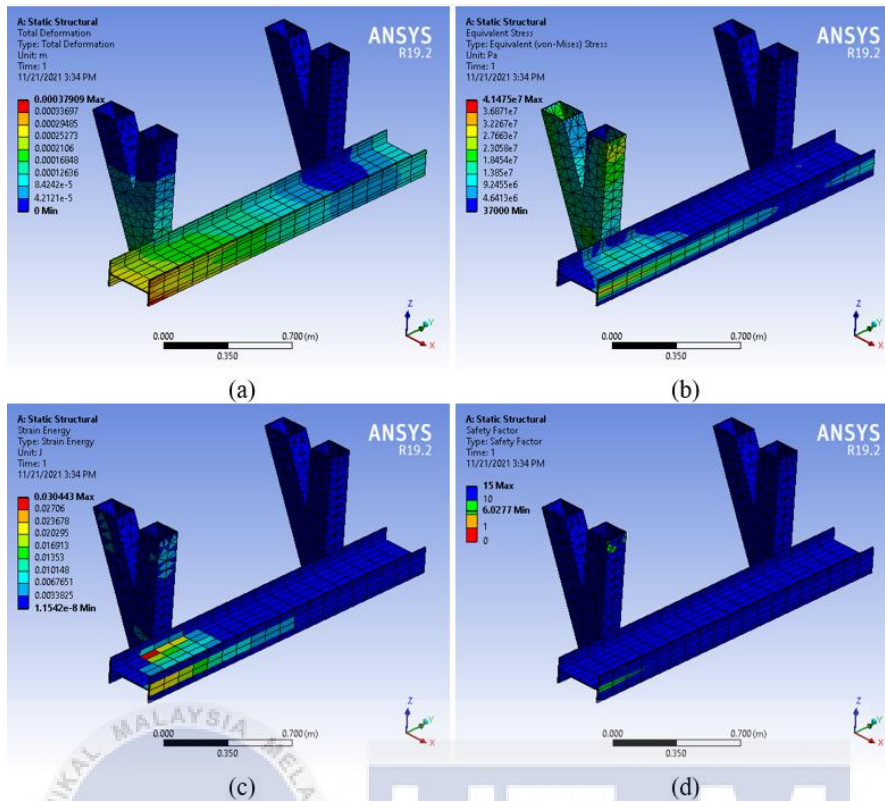


Figure 4.1. 37: Analysis P1 of W-beam with 25-degree angle (a) Total Deformation (b) Maximum Stress Von Mises (c) Strain Energy (d) Factor of Safety

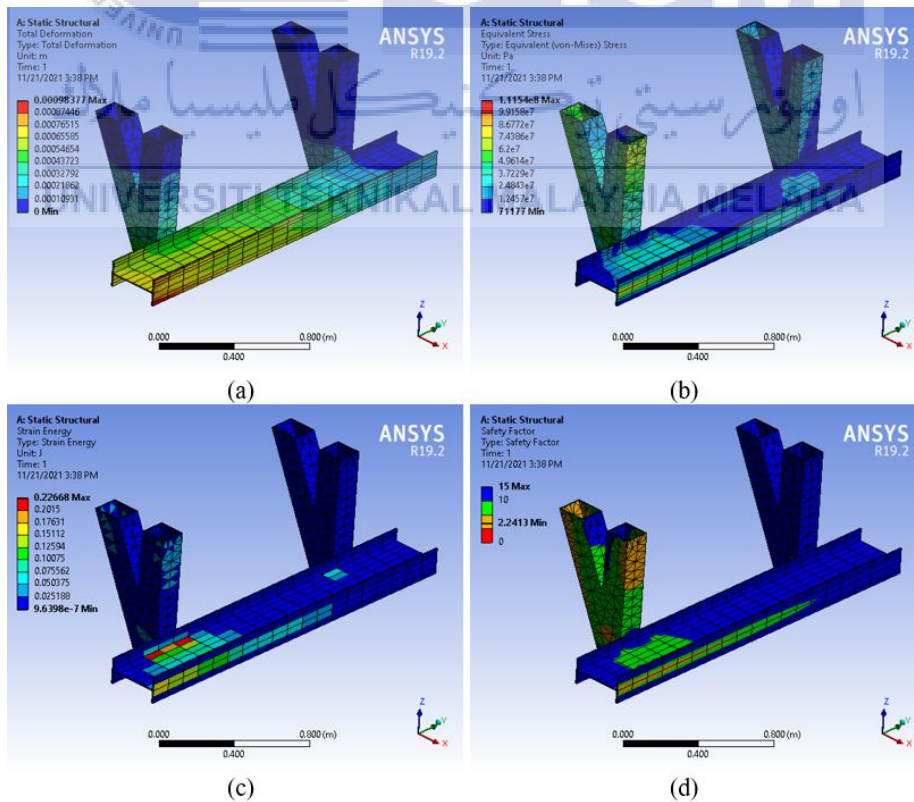


Figure 4.1. 38: Analysis P2 of W-beam with 25-degree angle (a) Total Deformation (b) Maximum Stress Von Mises (c) Strain Energy (d) Factor of Safety

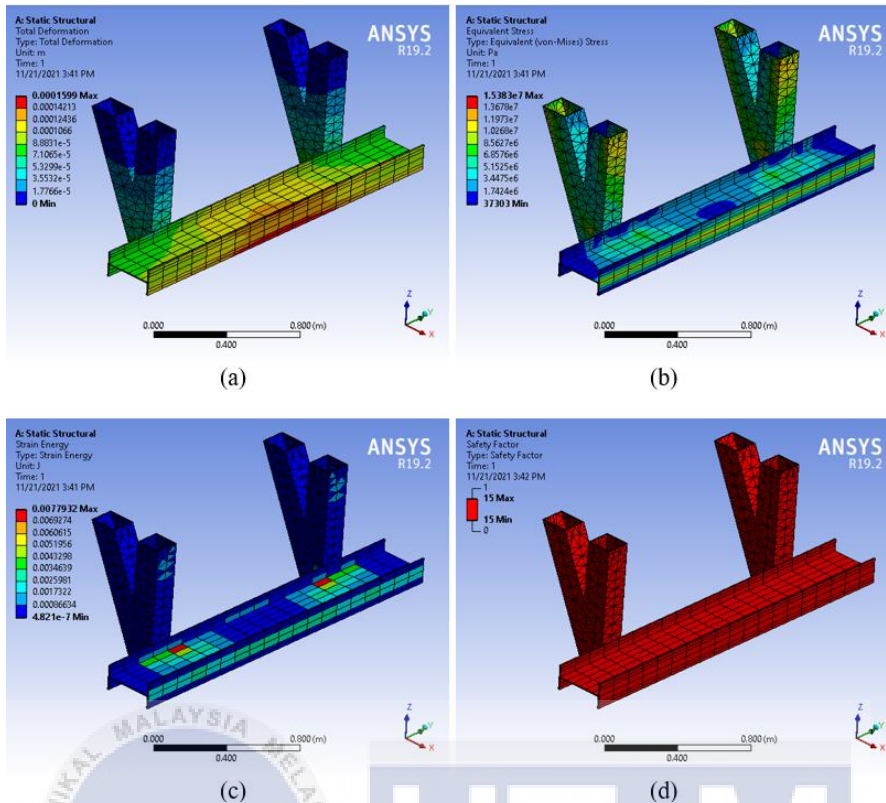


Figure 4.1. 39: Analysis P3 of W-beam with 25-degree angle (a) Total Deformation (b) Maximum Stress Von Mises (c) Strain Energy (d) Factor of Safety

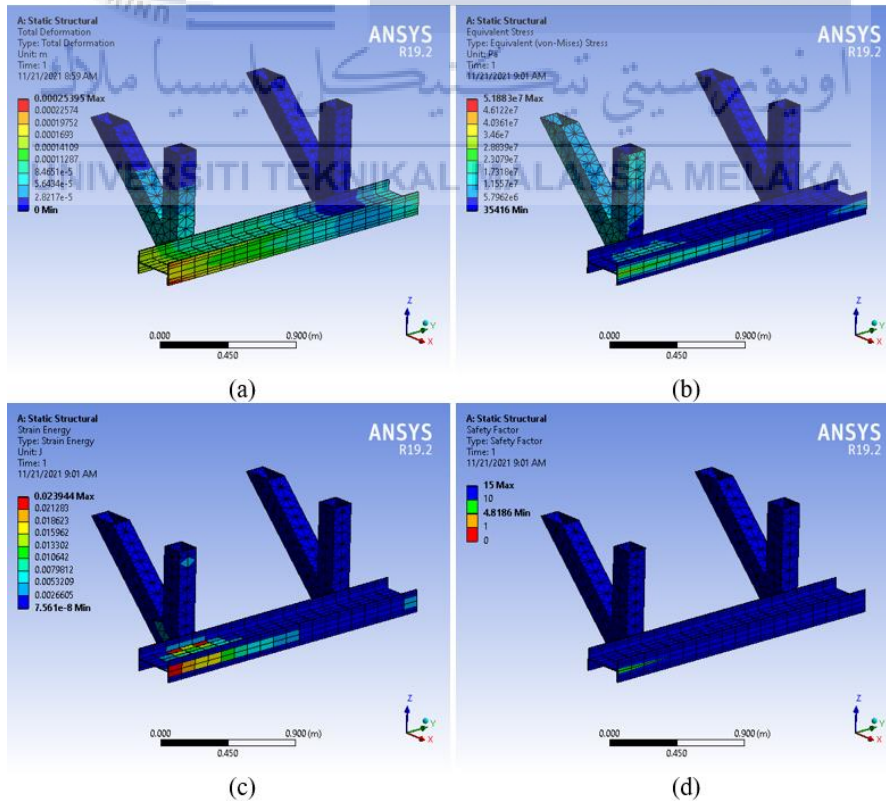


Figure 4.1. 40: Analysis P1 of W-beam with 45-degree angle (a) Total Deformation (b) Maximum Stress Von Mises (c) Strain Energy (d) Factor of Safety

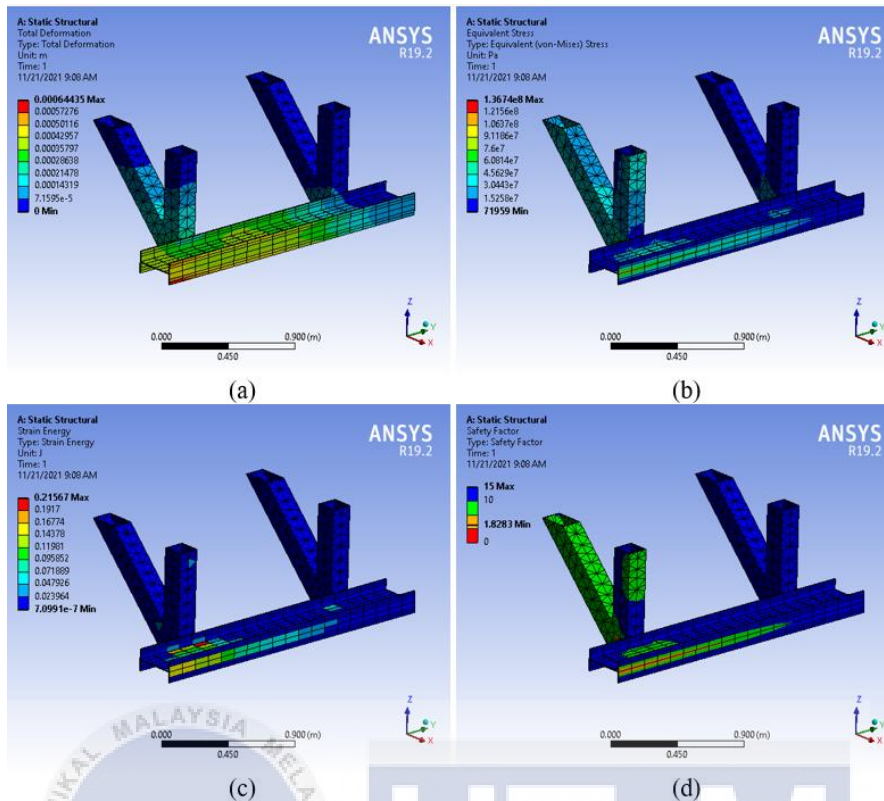


Figure 4.1. 41: Analysis P2 of W-beam with 45-degree angle (a) Total Deformation (b) Maximum Stress Von Mises (c) Strain Energy (d) Factor of Safety

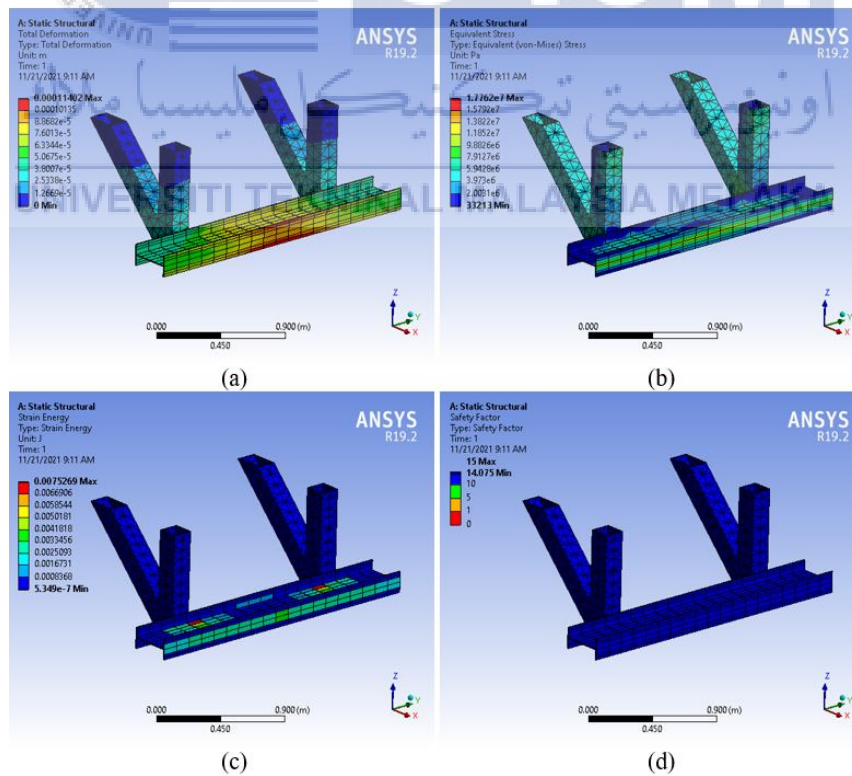


Figure 4.1. 42: Analysis P3 of W-beam with 45-degree angle (a) Total Deformation (b) Maximum Stress Von Mises (c) Strain Energy (d) Factor of Safety

4.1.2.3 Rectangular Hollow Beam with 15, 25 and 25 Degrees of Angle of Support

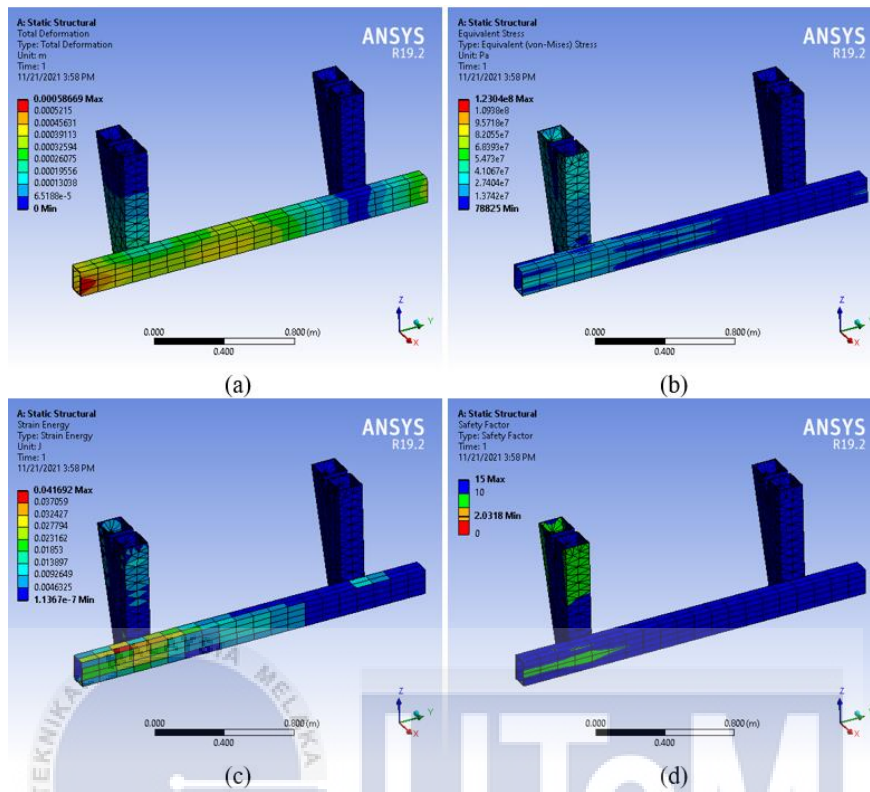


Figure 4.1. 43: Analysis P1 of Rectangular Hollow beam with 15-degree angle (a) Total Deformation (b) Maximum Stress Von Mises (c) Strain Energy (d) Factor of Safety

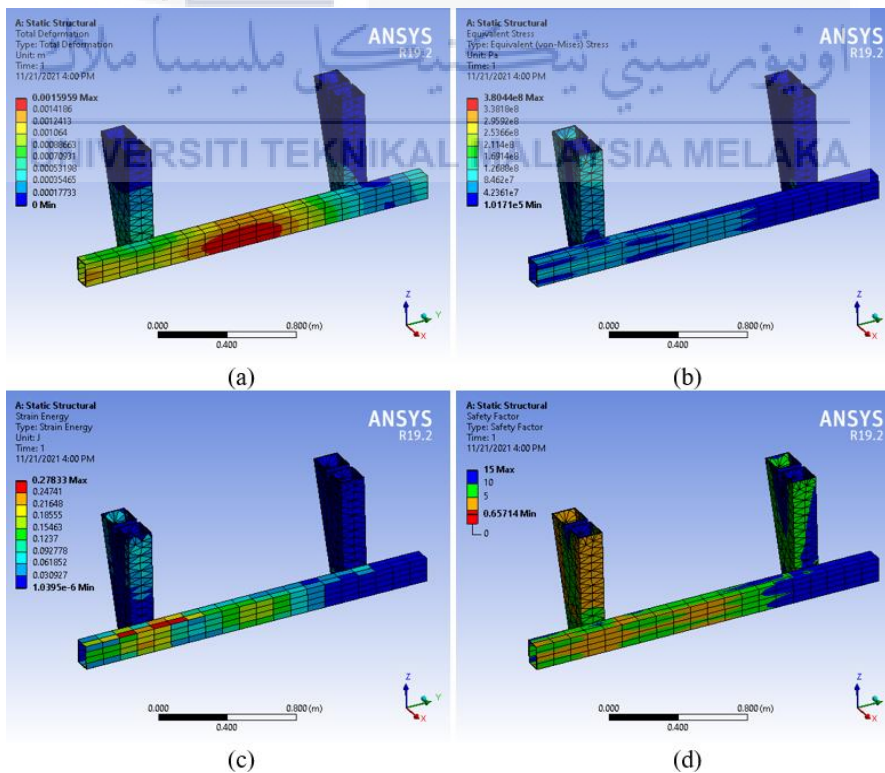


Figure 4.1. 44: Analysis P2 of Rectangular Hollow beam with 15-degree angle (a) Total Deformation (b) Maximum Stress Von Mises (c) Strain Energy (d) Factor of Safety

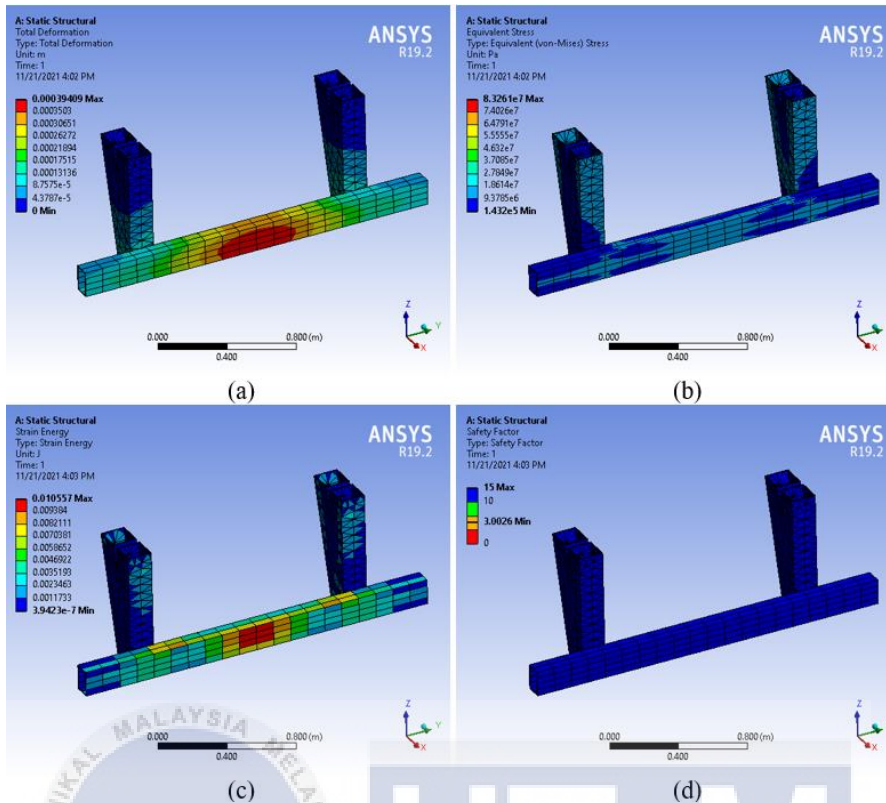


Figure 4.1. 45: Analysis P3 of Rectangular Hollow beam with 15-degree angle (a) Total Deformation (b) Maximum Stress Von Mises (c) Strain Energy (d) Factor of Safety

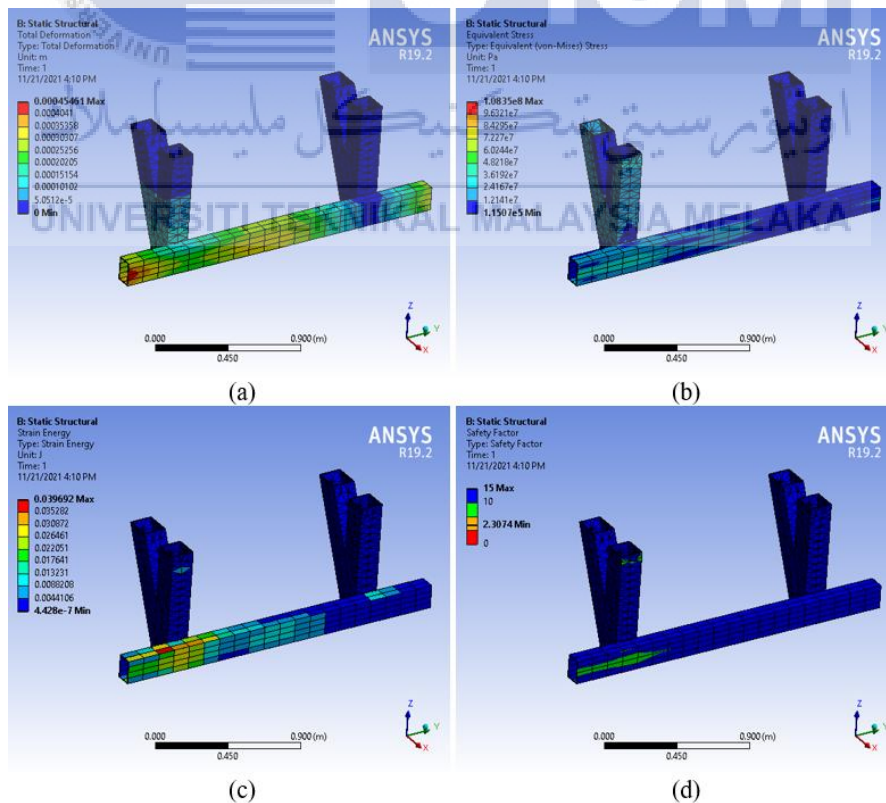


Figure 4.1. 46: Analysis P1 of Rectangular Hollow beam with 25-degree angle (a) Total Deformation (b) Maximum Stress Von Mises (c) Strain Energy (d) Factor of Safety

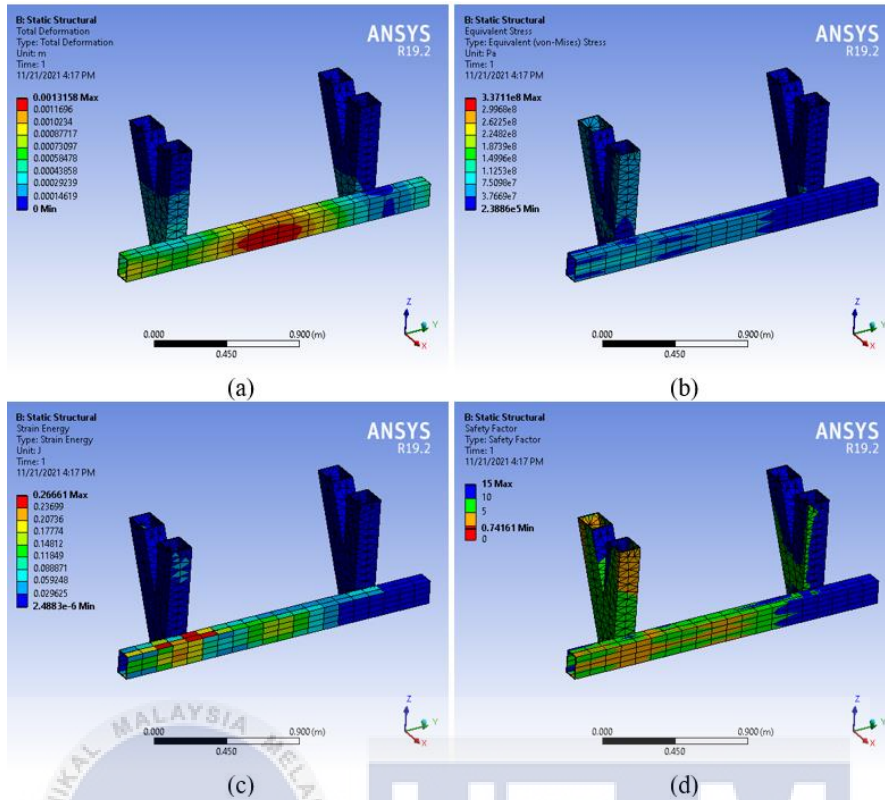


Figure 4.1. 47: Analysis P2 of Rectangular Hollow beam with 25-degree angle (a) Total Deformation (b) Maximum Stress Von Mises (c) Strain Energy (d) Factor of Safety

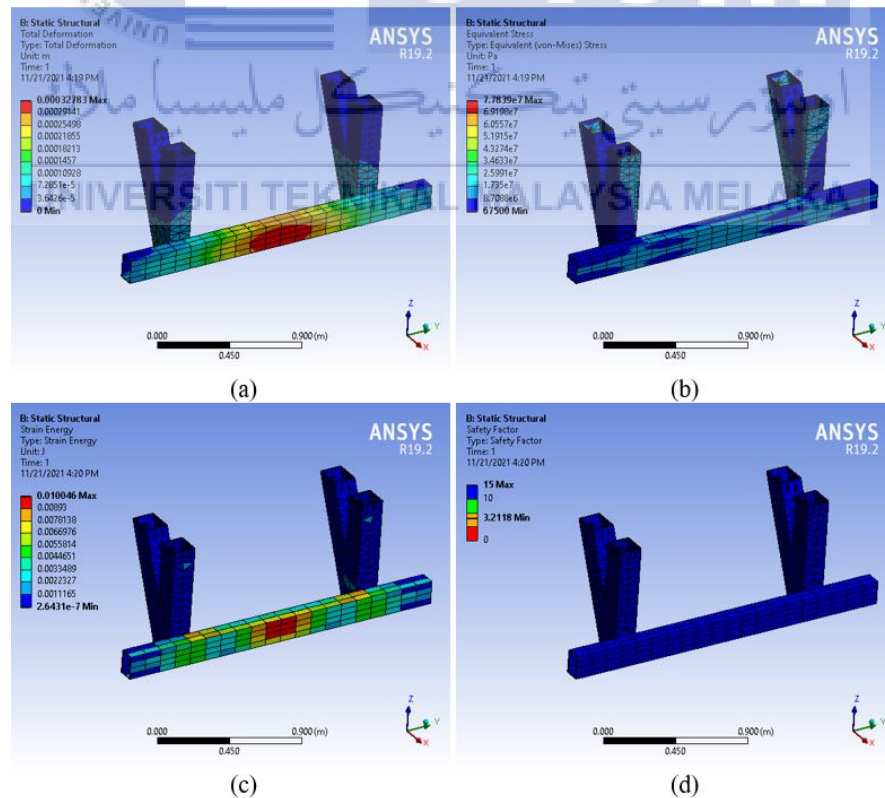


Figure 4.1. 48: Analysis P3 of Rectangular Hollow beam with 25-degree angle (a) Total Deformation (b) Maximum Stress Von Mises (c) Strain Energy (d) Factor of Safety

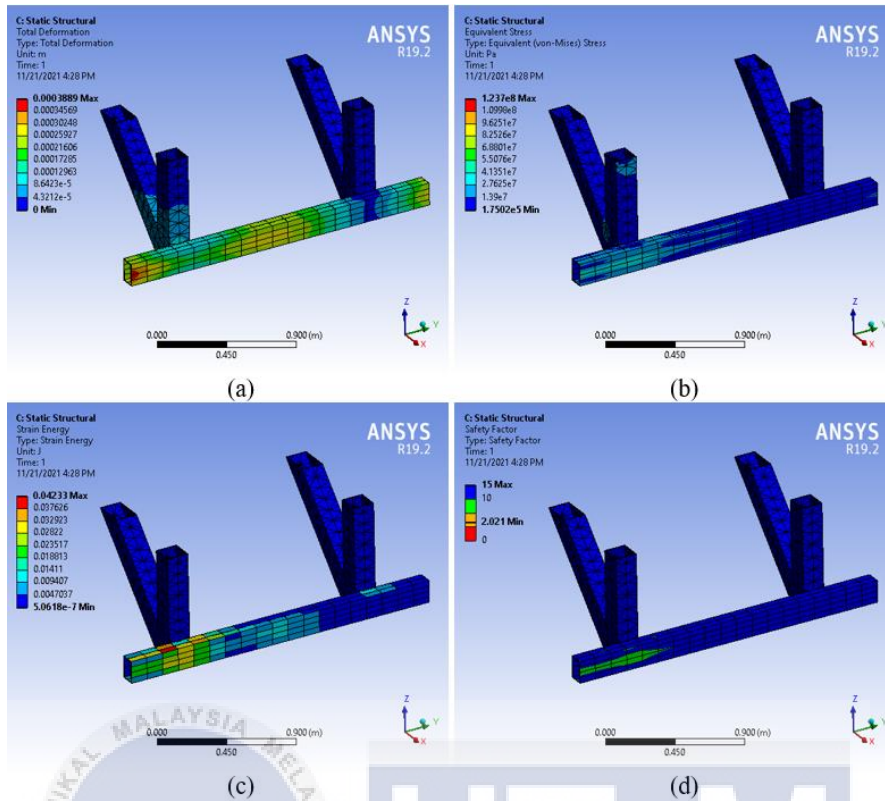


Figure 4.1. 49: Analysis P1 of Rectangular Hollow beam with 45-degree angle (a) Total Deformation (b) Maximum Stress Von Mises (c) Strain Energy (d) Factor of Safety

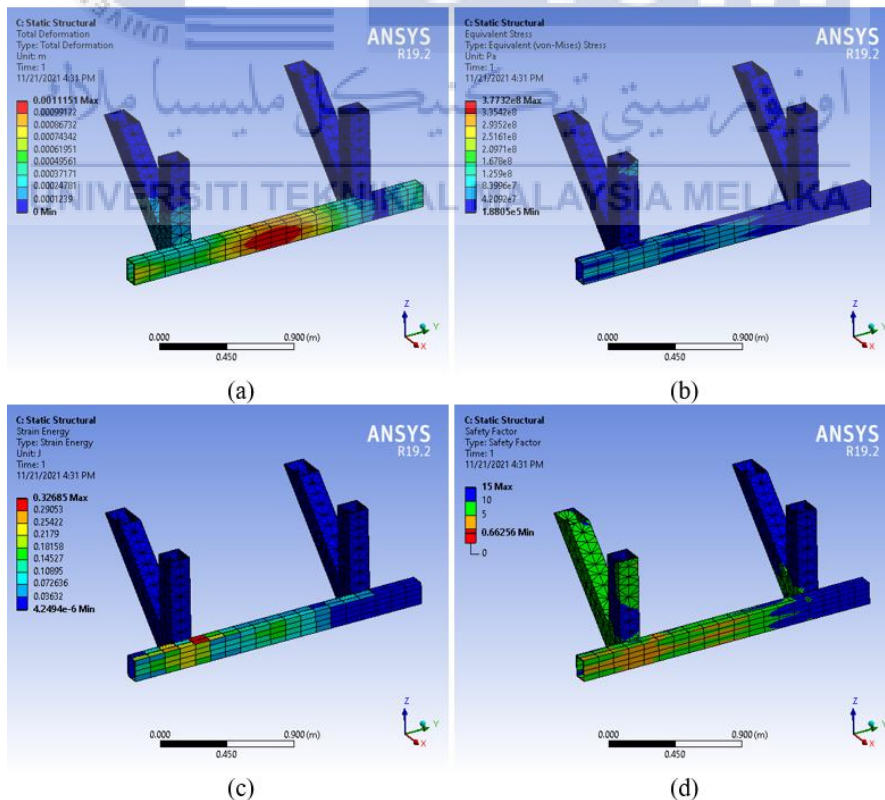


Figure 4.1. 50: Analysis P2 of Rectangular Hollow beam with 45-degree angle (a) Total Deformation (b) Maximum Stress Von Mises (c) Strain Energy (d) Factor of Safety

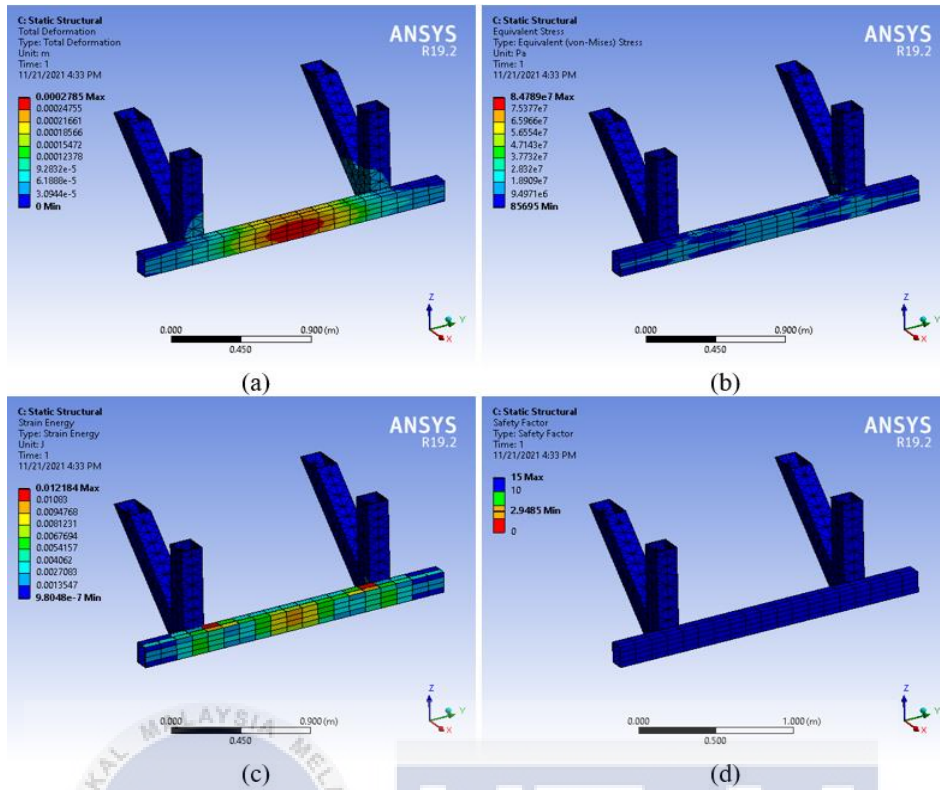


Figure 4.1. 51: Analysis P3 of Rectangular Hollow beam with 45-degree angle (a) Total Deformation (b) Maximum Stress Von Mises (c) Strain Energy (d) Factor of Safety

4.1.2.4 Square Hollow Beam with 15, 25 and 25 Degrees of Angle of Support

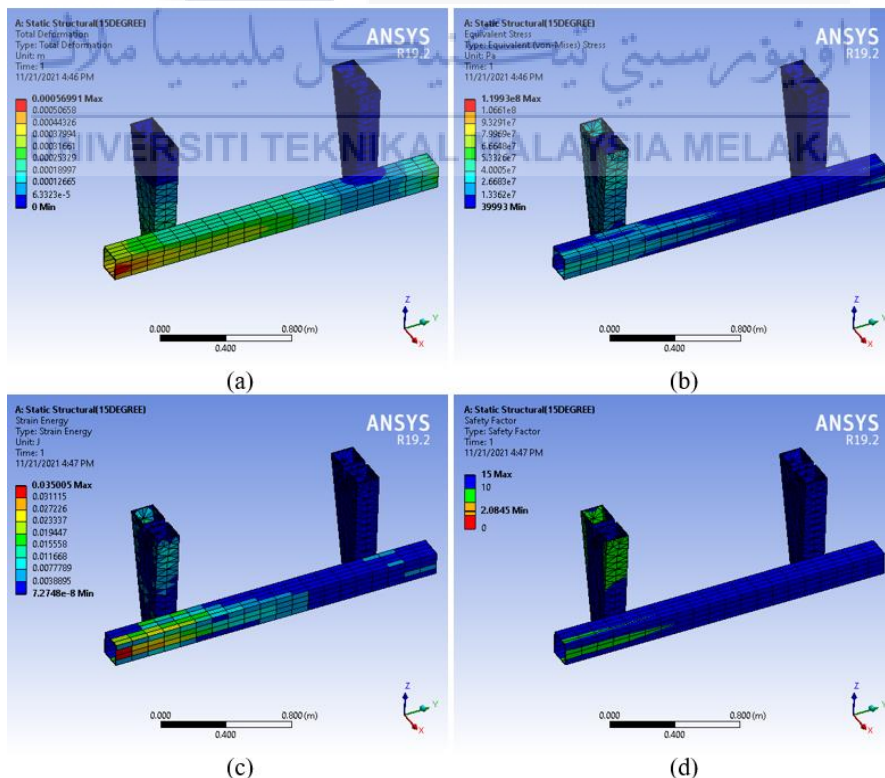


Figure 4.1. 52: Analysis P1 of Square Hollow beam with 15-degree angle (a) Total Deformation (b) Maximum Stress Von Mises (c) Strain Energy (d) Factor of Safety

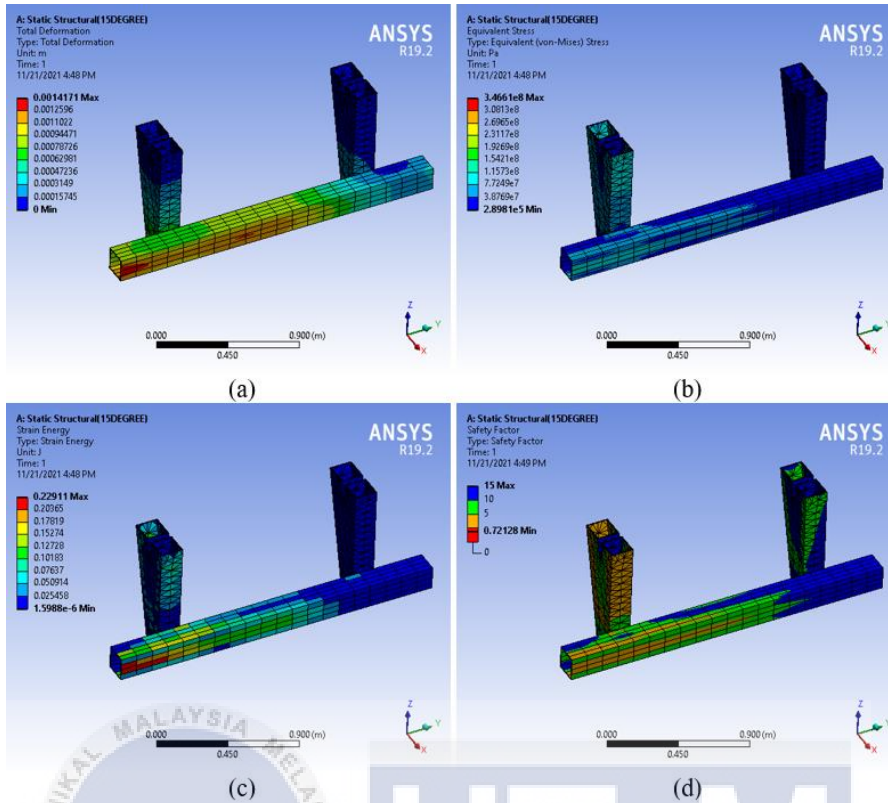


Figure 4.1. 53: Analysis P2 of Square Hollow beam with 15-degree angle (a) Total Deformation (b) Maximum Stress Von Mises (c) Strain Energy (d) Factor of Safety

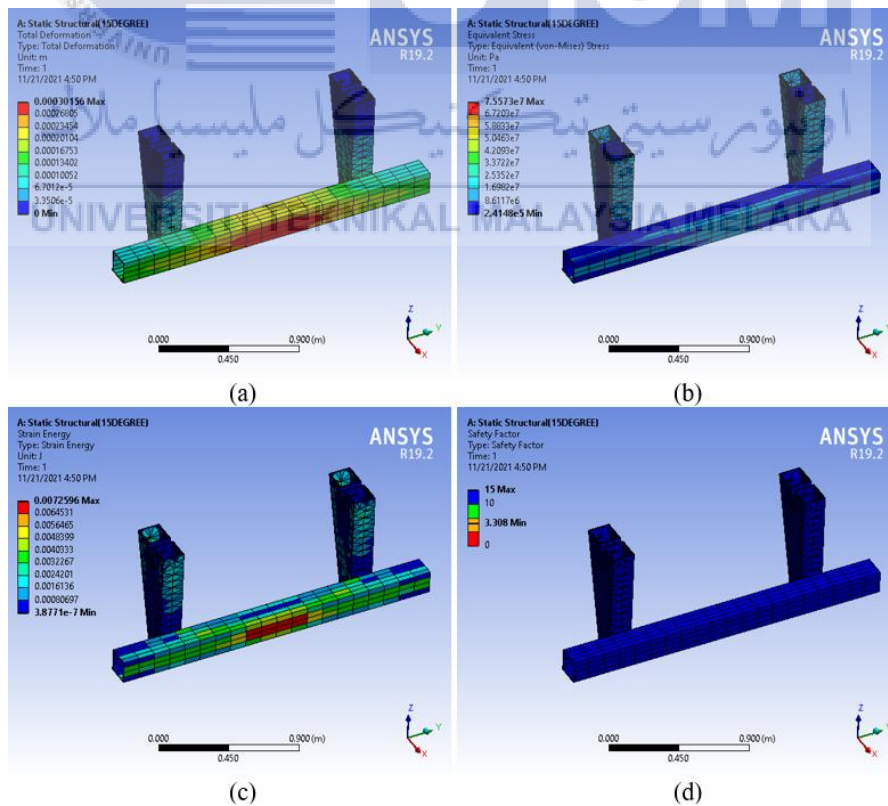


Figure 4.1. 54: Analysis P3 of Square Hollow beam with 15-degree angle (a) Total Deformation (b) Maximum Stress Von Mises (c) Strain Energy (d) Factor of Safety

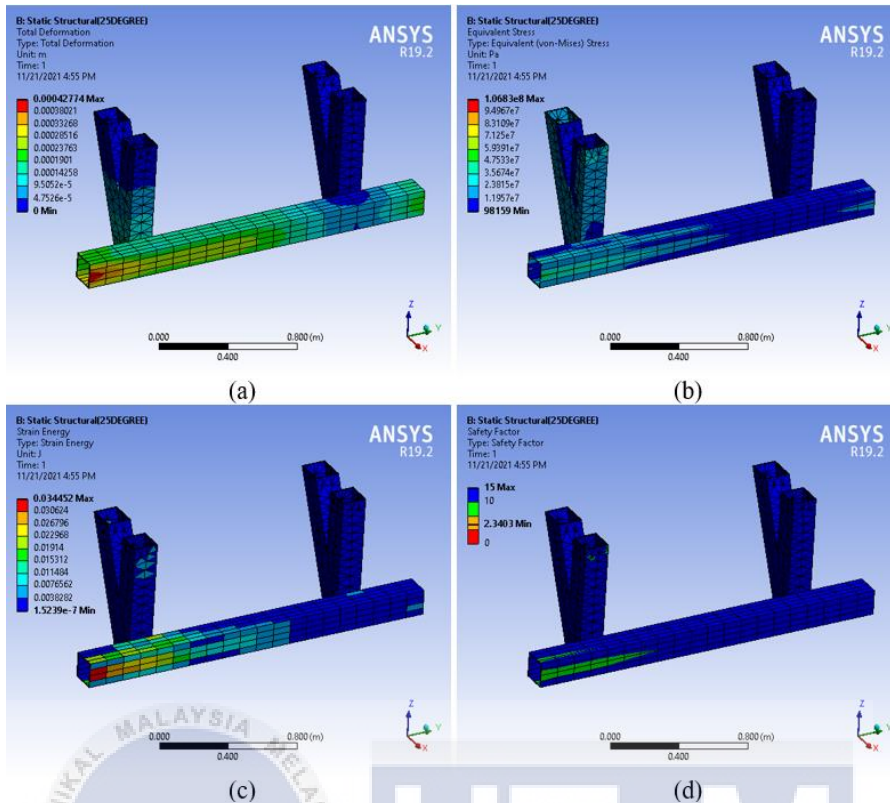


Figure 4.1. 55: Analysis P1 of Square Hollow beam with 25-degree angle (a) Total Deformation (b) Maximum Stress Von Mises (c) Strain Energy (d) Factor of Safety

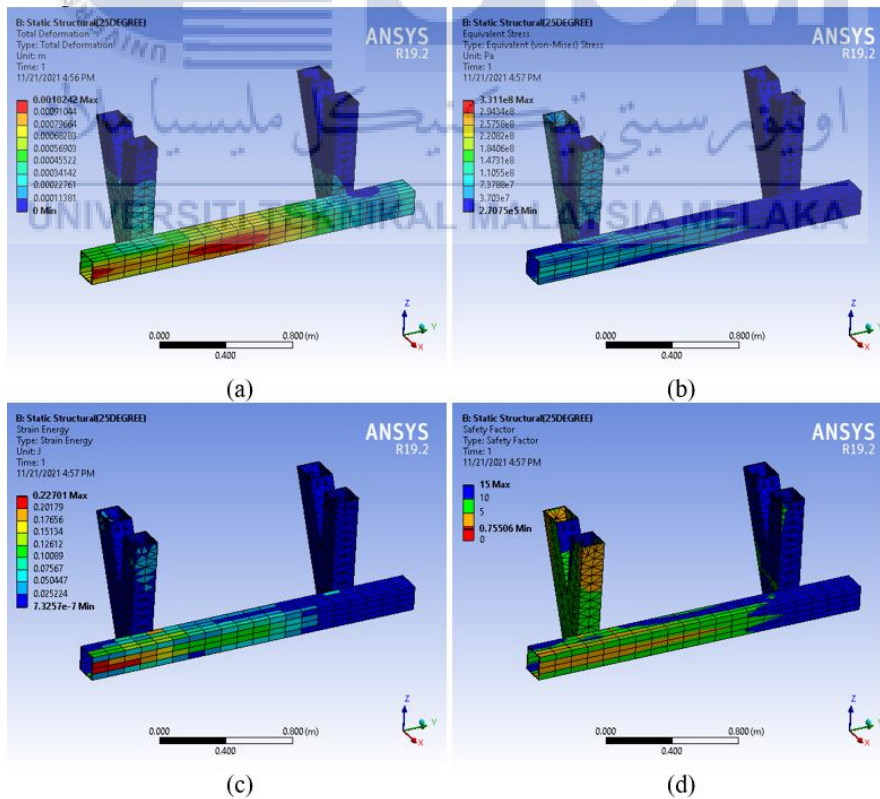


Figure 4.1. 56: Analysis P2 of Square Hollow beam with 25-degree angle (a) Total Deformation (b) Maximum Stress Von Mises (c) Strain Energy (d) Factor of Safety

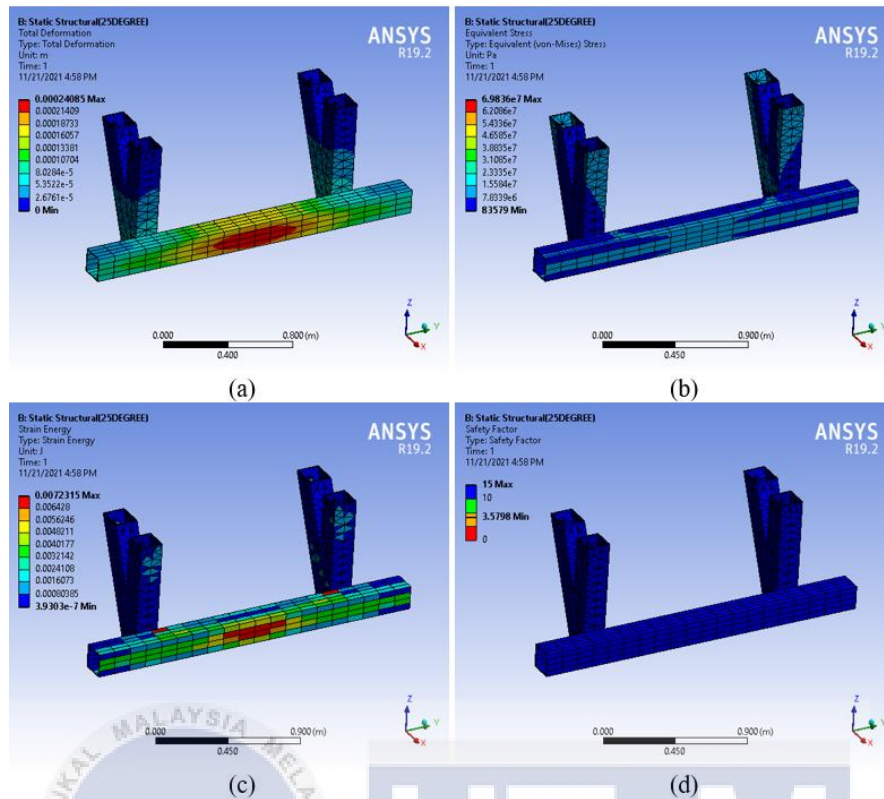


Figure 4.1. 57: Analysis P3 of Square Hollow beam with 25-degree angle (a) Total Deformation (b) Maximum Stress Von Mises (c) Strain Energy (d) Factor of Safety

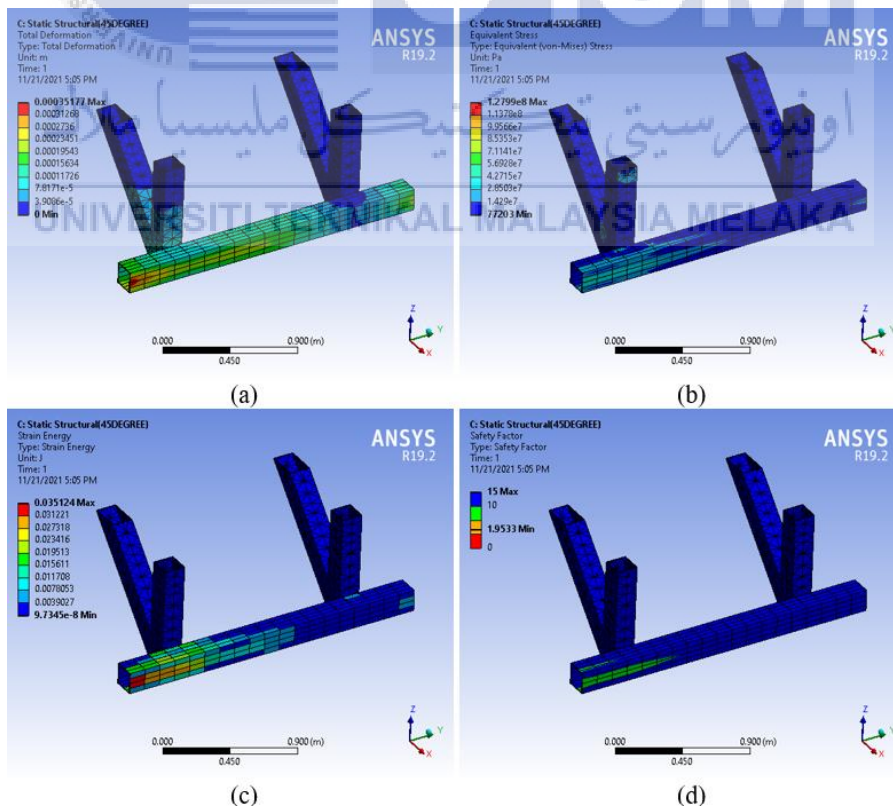


Figure 4.1. 58: Analysis P1 of Square Hollow beam with 45-degree angle (a) Total Deformation (b) Maximum Stress Von Mises (c) Strain Energy (d) Factor of Safety

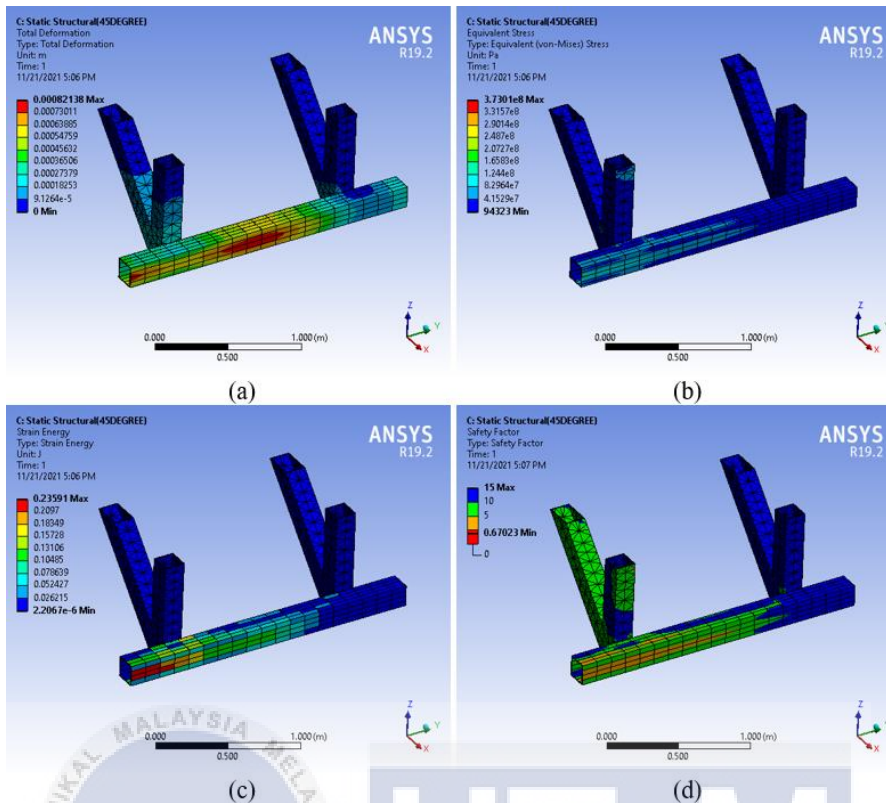


Figure 4.1. 59: Analysis P2 of Square Hollow beam with 45-degree angle (a) Total Deformation (b) Maximum Stress Von Mises (c) Strain Energy (d) Factor of Safety

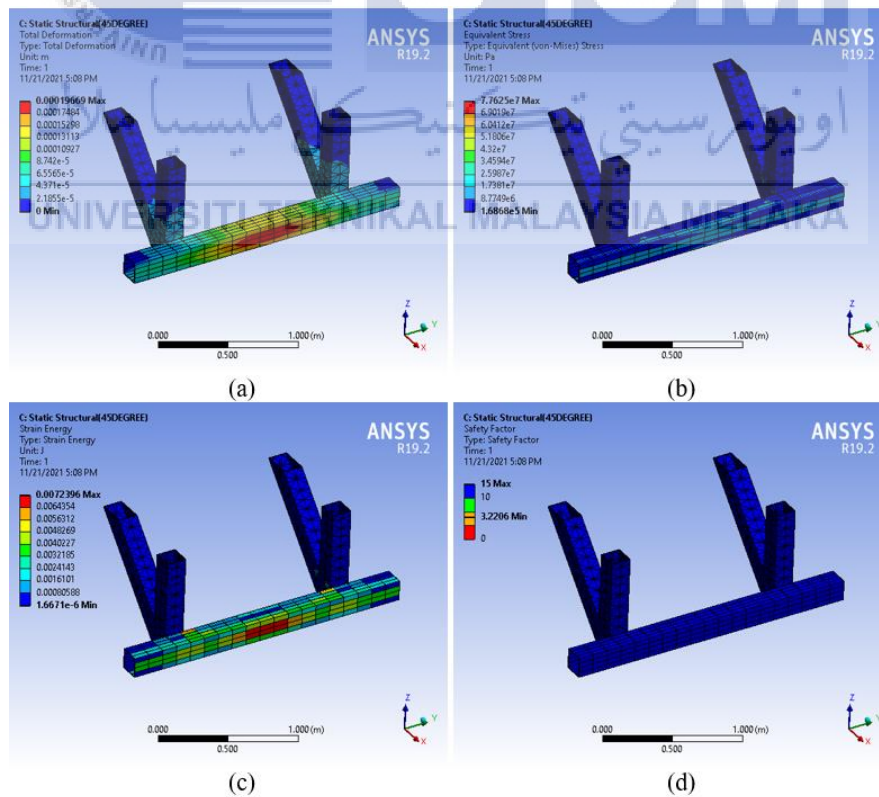


Figure 4.1. 60: Analysis P3 of Square Hollow beam with 45-degree angle (a) Total Deformation (b) Maximum Stress Von Mises (c) Strain Energy (d) Factor of Safety

All the support structure analyses provide a result analysis, as shown above. Only one data shown is incorrect: the safety factor of Figure 4.1. 39: Analysis P3 of W-beam with 25-degree angle. The figure shows that all red on the structure body means the results shown are incorrect, but it does not mean the result cannot be used. This result was obtained because of the limitation of boundary setup when using ANSYS software. This limitation refers to the limit of the safety factor; that is, the analysis will evaluate FS until the value of 15 only. Thus, as shown on the comparison of the data, W-Beam showed the highest strength among other beams, which means that the FS value of W-beam for the result is higher than 15. Other than that, all the other figures did not have any problem.

4.1.2.5 Data Comparison Analysis of Angle of Support Structure

Table 4.1. 4: Data Analysis of Support Structure by Using Circular Hollow Beam

Angle (°)	15			25			45		
Force (kN)	P1=25	P2=100	P3=25	P1=25	P2=100	P3=25	P1=25	P2=100	P3=25
δ_T (mm)	0.52104	1.3857	0.32426	0.41767	1.0977	0.27084	0.35694	0.95417	0.23631
σ_{VM} (Pa)	6.07E+07	2.30E+08	5.63E+07	6.65E+07	2.48E+08	5.77E+07	8.16E+07	3.04E+08	7.08E+07
U(J)	0.029188	0.24828	0.010481	0.02966	0.010239	0.010239	0.03146	0.2787	0.010673
FS	4.1178	1.089	4.4366	3.7596	4.3301	4.3301	3.0624	0.82272	3.5333

Table 4.1. 5: Data Analysis of Support Structure by Using W-Beam

Angle (°)	15			45			25		
Force (kN)	P1=25	P2=100	P3=25	P1=25	P2=100	P3=25	P1=25	P2=100	P3=25
δ_T (mm)	0.60463	1.6033	0.24842	0.37909	0.98377	0.1599	0.25395	0.64435	0.11402
σ_{VM} (Pa)	4.17E+07	1.21E+08	1.96E+07	4.15E+07	1.12E+08	1.54E+07	5.19E+07	1.37E+08	1.78E+07
U(J)	0.022199	0.19312	0.006838	0.030443	0.22668	0.007793	0.023944	0.21567	0.007527
FS	5.9983	2.0662	12.724	6.0277	2.2413	15	4.8186	1.8283	14.075

Table 4.1. 6: Data Analysis of Support Structure by Using Rectangular Hollow Beam

Angle (°)	15			25			45		
Force (kN)	P1=25	P2=100	P3=25	P1=25	P2=100	P3=25	P1=25	P2=100	P3=25
δ_T (mm)	0.58669	1.5959	0.39409	0.45461	1.3158	0.32783	0.3889	1.11151	0.2785
σ_{VM} (Pa)	1.23E+08	3.80E+08	8.33E+09	1.08E+08	3.37E+08	7.78E+07	1.24E+08	3.77E+08	8.48E+09
U(J)	0.041692	0.27833	0.010557	0.039692	0.26661	0.010046	0.04233	0.32685	0.012184
FS	2.0318	0.65714	3.0026	2.3074	0.74161	3.2118	2.021	0.66256	2.9485

Table 4.1. 7: Data Analysis of Support Structure by Using Square Hollow Beam

Angle (°)	15			25			45		
Force (kN)	P1=25	P2=100	P3=25	P1=25	P2=100	P3=25	P1=25	P2=100	P3=25
δ_T (mm)	0.56991	1.4171	0.30156	0.42774	1.0242	0.24085	0.35177	0.82138	0.19669
σ_{VM} (Pa)	1.20E+08	3.47E+08	7.56E+07	1.07E+08	3.31E+08	6.78E+07	1.28E+08	3.73E+08	7.76E+07
U(J)	0.035005	0.22911	0.00726	0.034452	0.22701	0.007232	0.035124	0.23591	0.00724
FS	2.0845	0.72128	3.308	2.3403	0.75506	3.5798	1.9533	0.67023	3.2206

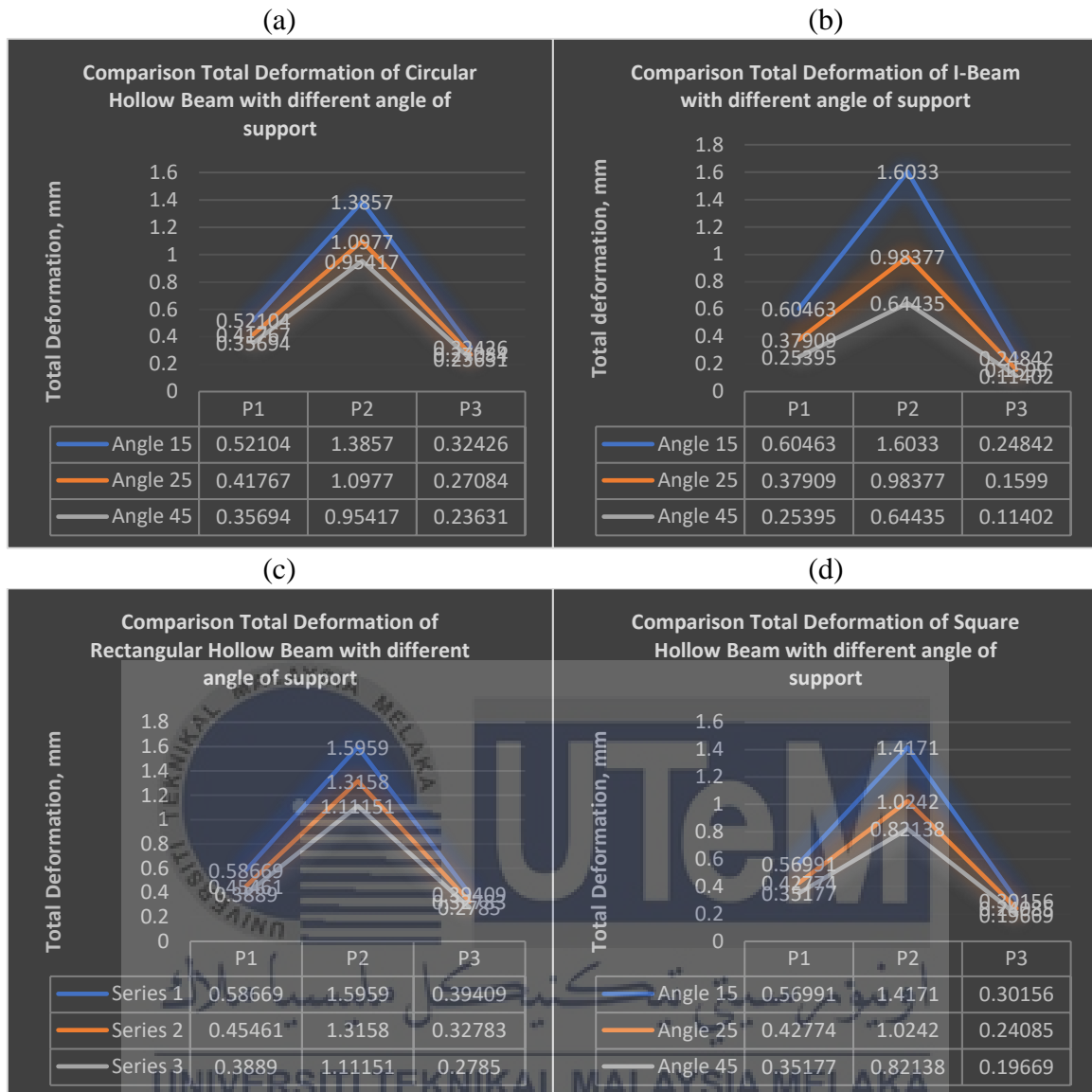


Figure 4.1. 61: Graph comparison total deformation vs angle of the support structure by using (a) Circular Hollow Beam (b) W-Beam (c) Rectangular Hollow Beam (d) Square Hollow Beam

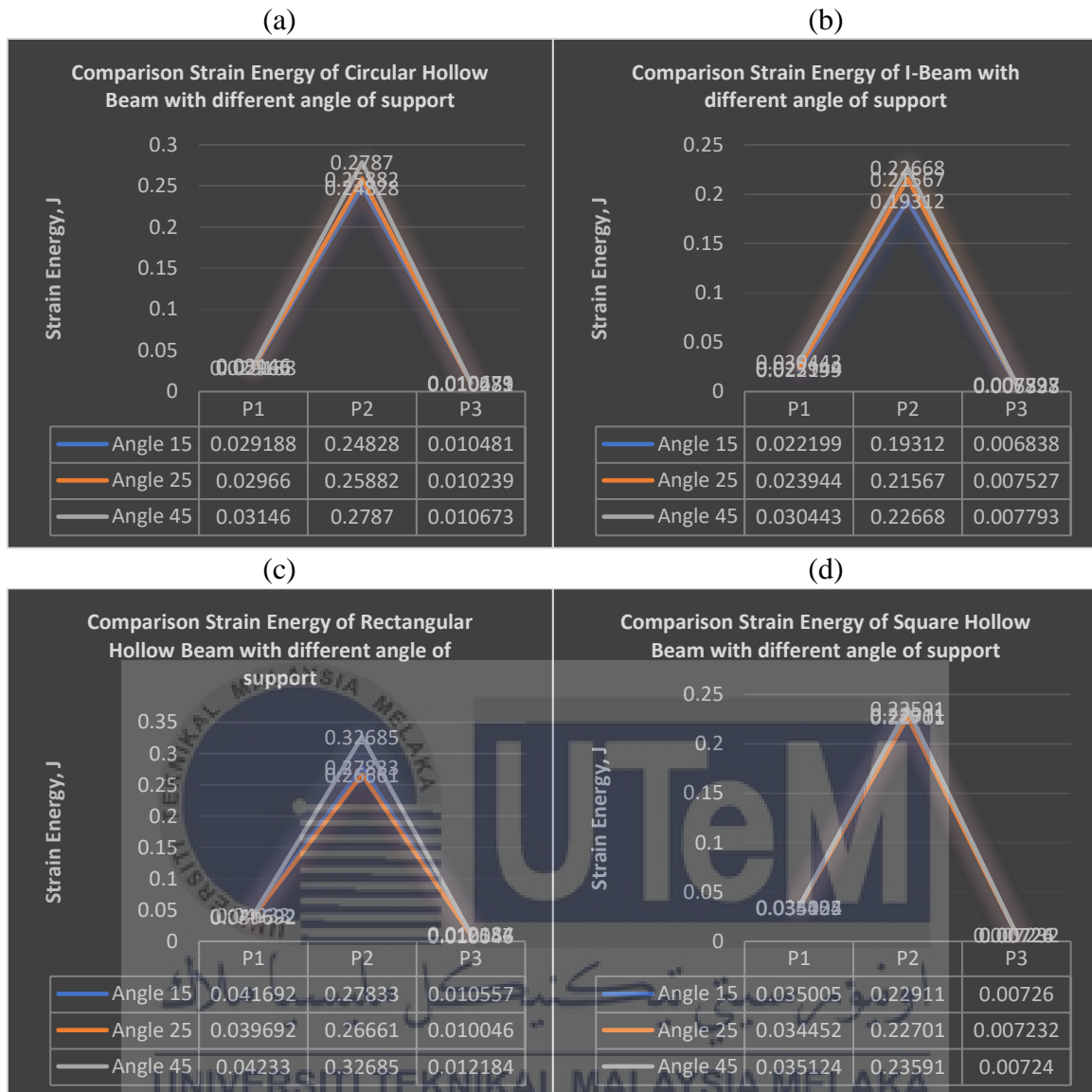


Figure 4.1. 62: Graph comparison strain energy vs angle of the support structure by using (a) Circular Hollow Beam (b) W-Beam (c) Rectangular Hollow Beam (d) Square Hollow Beam

Based on the data above, 45 degrees of support angle shown the best angle in receiving the impact load than 25 degrees and 15 degrees. The total deformation also proves that this angle did not exceed the standard of FMVSS. When the first analysis of the beam, the circular hollow beam is shown better output than other beams. However, when the beam assembly with the support, based on the data above, it demonstrated that a rectangular beam with 45 degrees of angle of support shows the best underide in receiving the impact load since it has the highest strain energy.

As shown on the data output, it validates the first analysis of support structure angle, where 45 degrees of angle of support is the best angle either it uses a different type of impact beam. The output with different impact beams shows that 45 degrees are the best angle for the support structure. By comparing the data output with the other journal (refer to Figure 2.2.5 (a)(b) and Figure 2.2.6 (a)(b), validate the data output since it is also shown the exact relation of energy absorption with the displacement. For the angle of the support structure, the higher the energy absorption, the lower the deformation of the structure. Thus, it verified the results trend since the shape of the data obtained was the same as the journal. This study found that the character of the angle of support structure also depends on the type of materials used.

4.1.3 Analysis Type of Beams Used for Support UPD

This section will analyse the UPD by letting the angle of 45 degrees for the angle of support and the rectangular beam used for the impact bar. The parameter that will be observed is the type of beams of support UPD.

4.1.3.1 Circular Hollow Beam of Support Structure

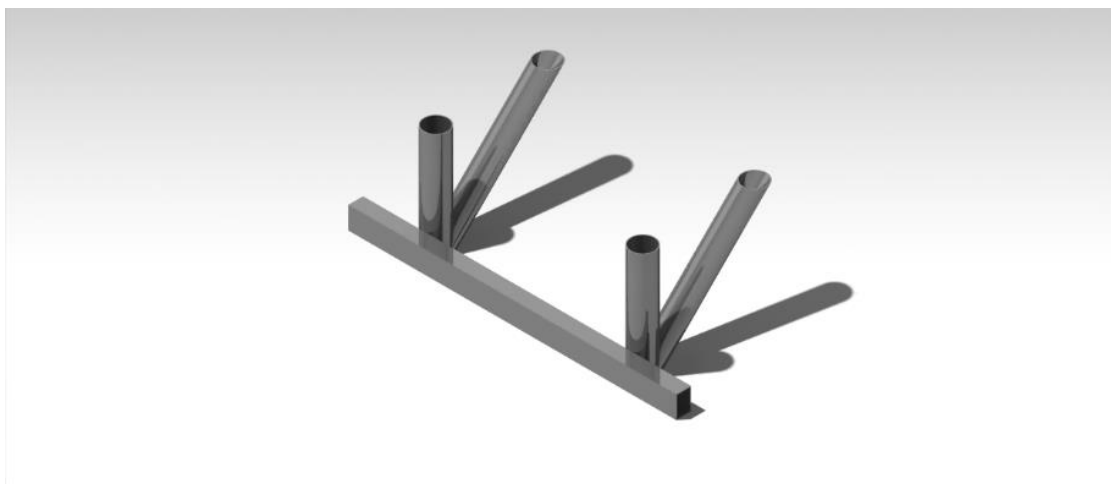


Figure 4.1. 63: Support structure using circular hollow beam

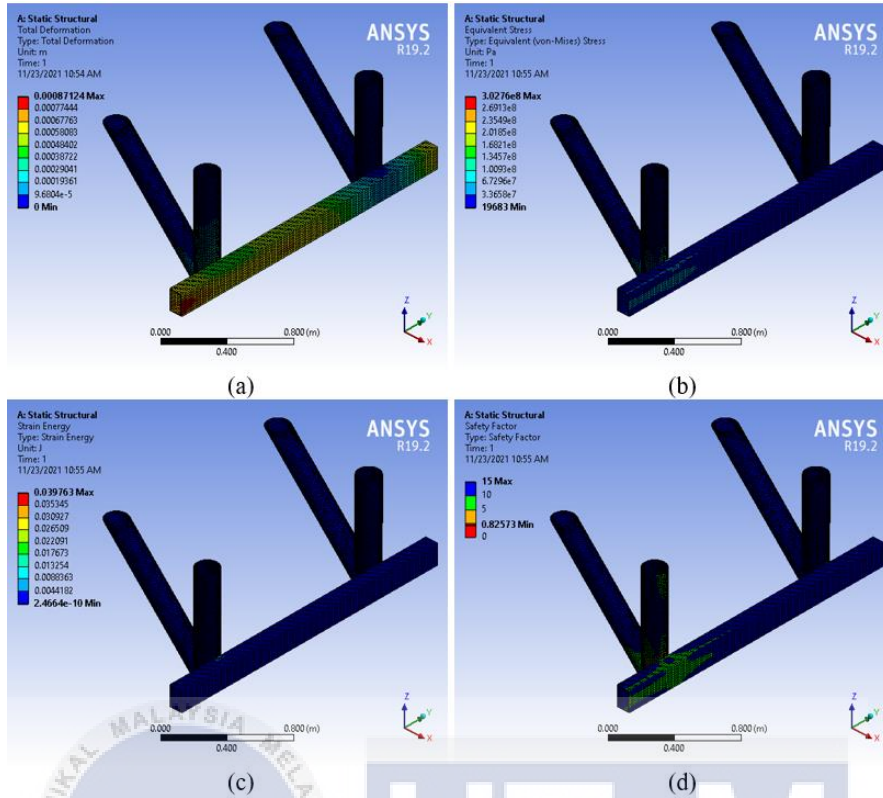


Figure 4.1. 64: P1 analysis angle of support structure using the circular hollow beam.

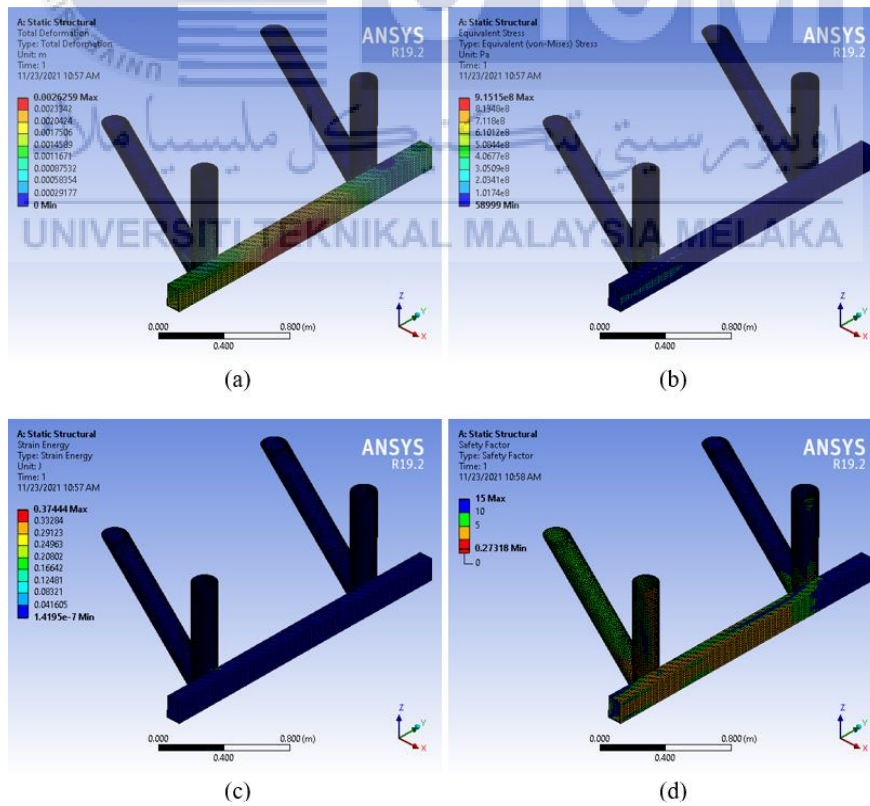


Figure 4.1. 65: P2 analysis angle of support structure using the circular hollow beam.

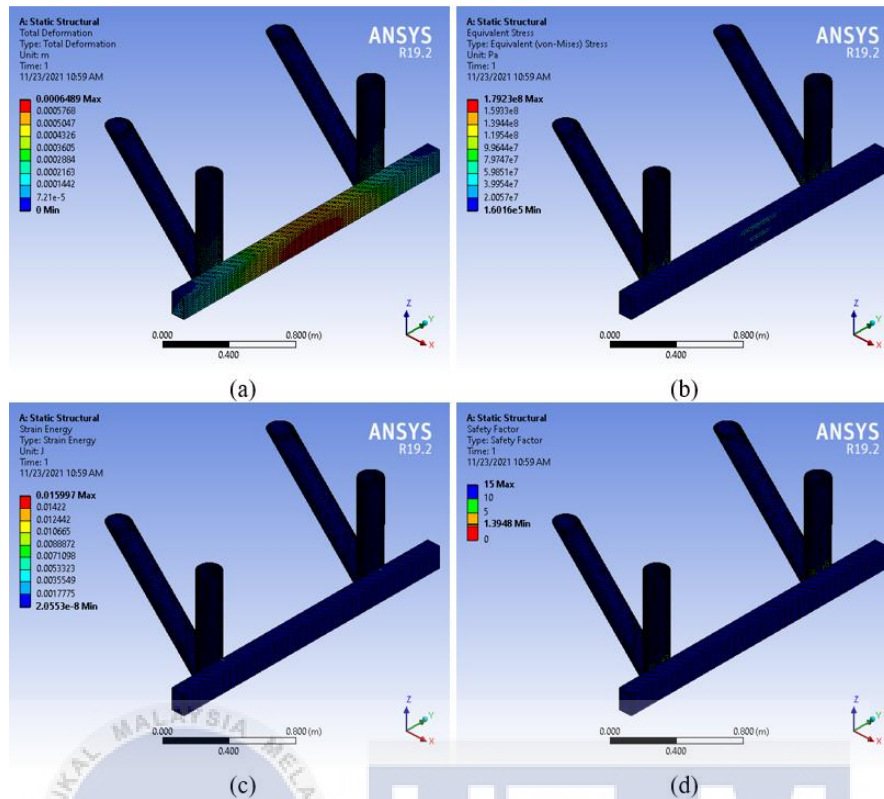


Figure 4.1. 66: P3 analysis angle of support structure using the circular hollow beam.

4.1.3.2 W-Beam of Support Structure

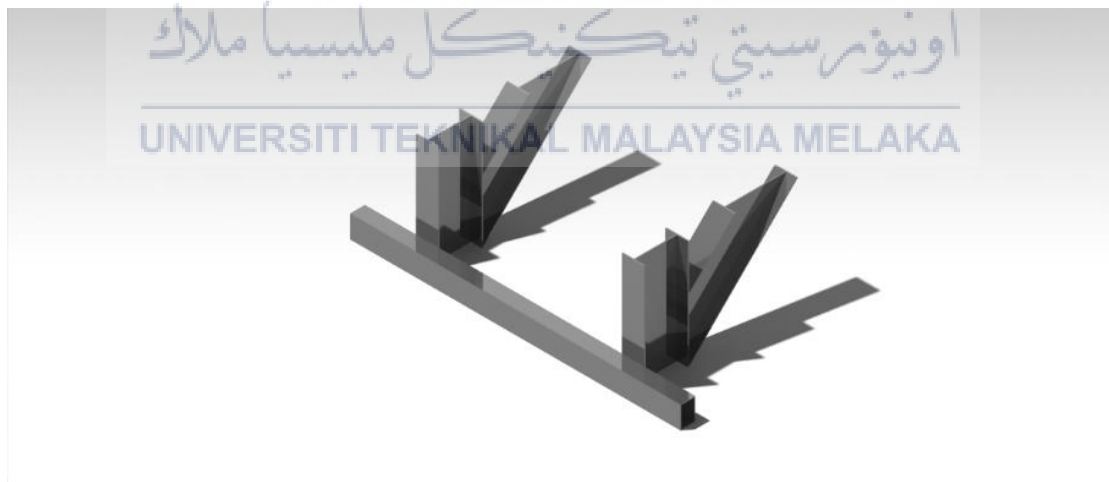


Figure 4.1. 67: Support structure using W-beam.

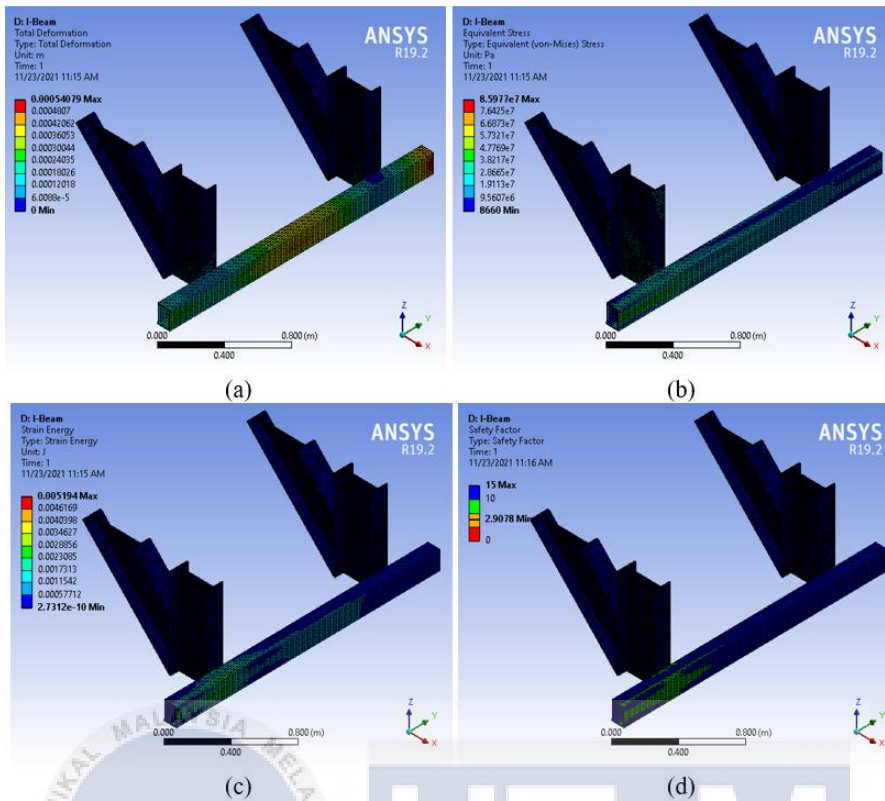


Figure 4.1. 68: P1 analysis angle of support structure using W-beam.

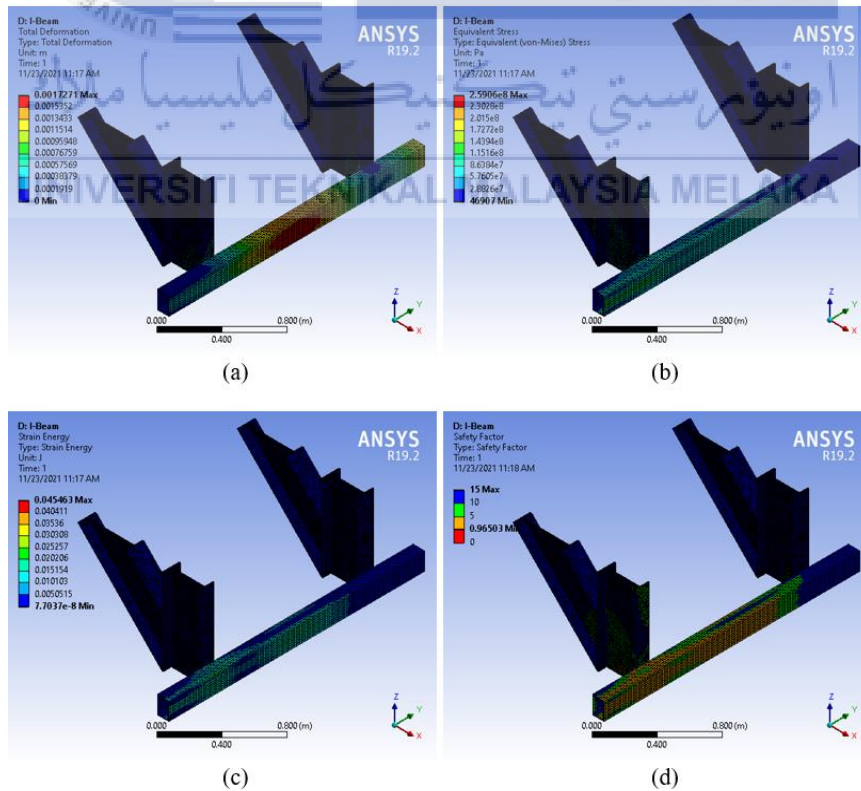


Figure 4.1. 69: P2 analysis angle of support structure using W-beam.

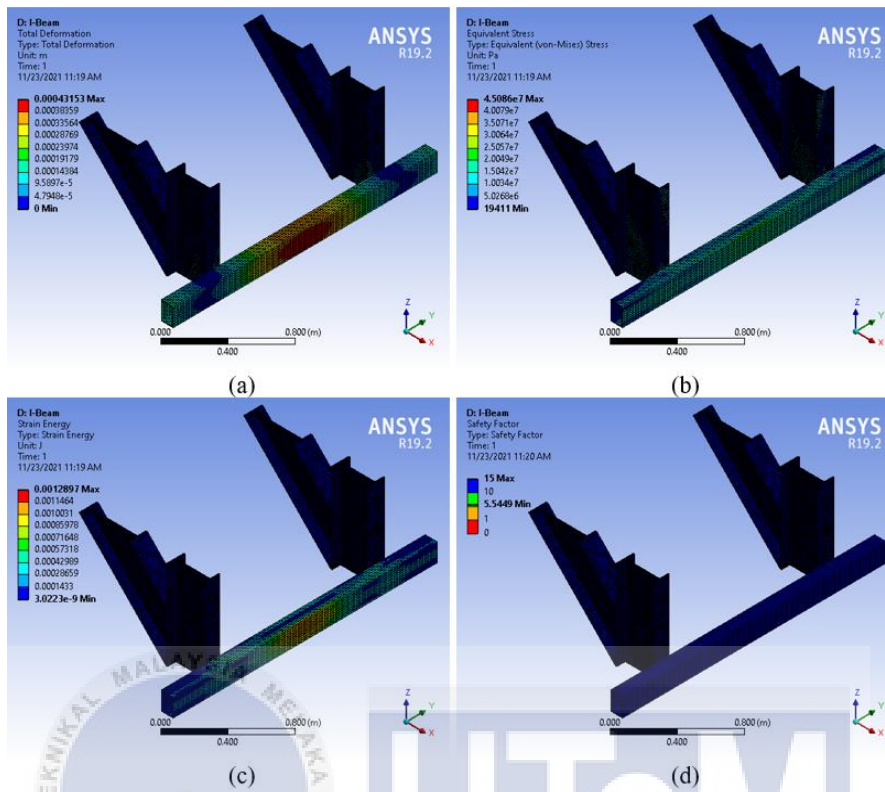


Figure 4.1. 70: P3 analysis angle of support structure using W-beam.

4.1.3.3 Rectangular Hollow Beam of Support Structure



Figure 4.1. 71: Support structure using the rectangular hollow beam.

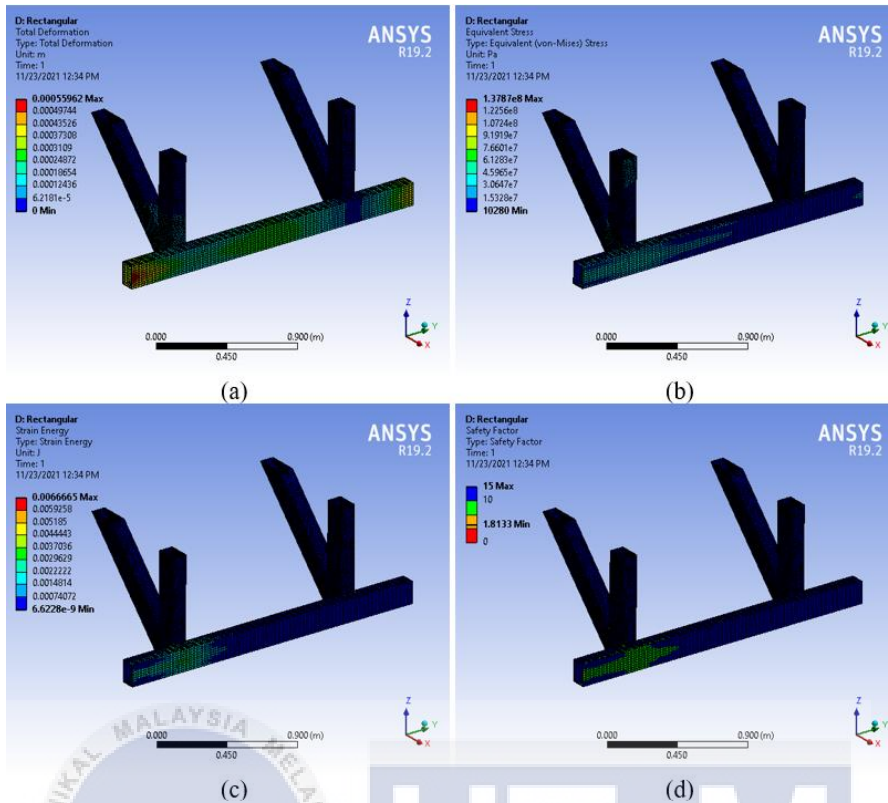


Figure 4.1. 72: P1 analysis angle of support structure using the rectangular hollow beam.

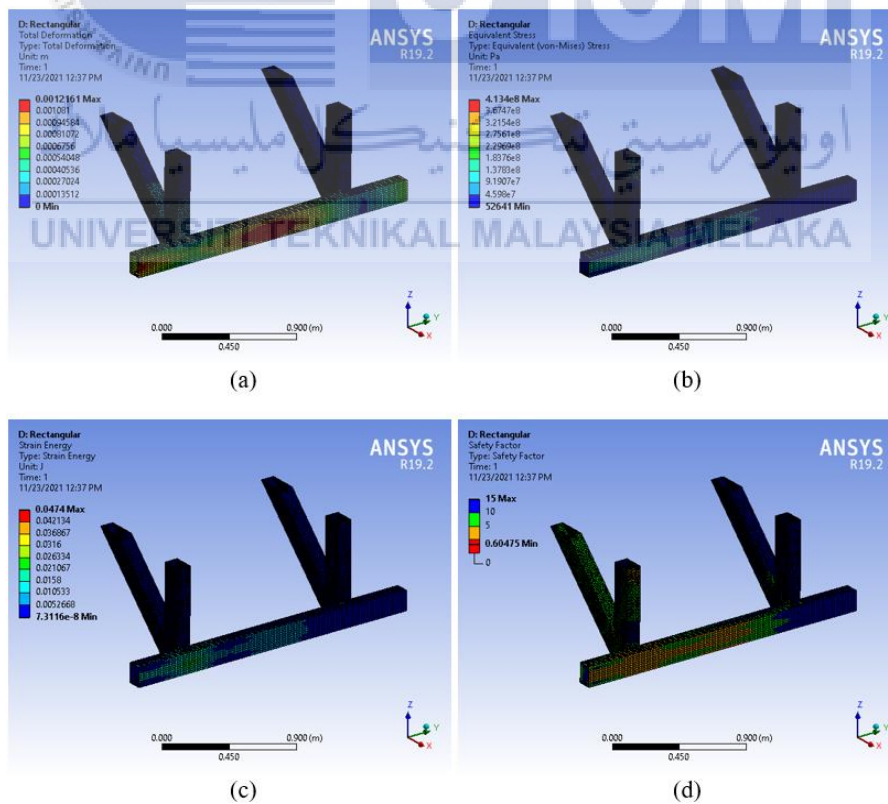


Figure 4.1. 73: P2 analysis angle of support structure using the rectangular hollow beam.

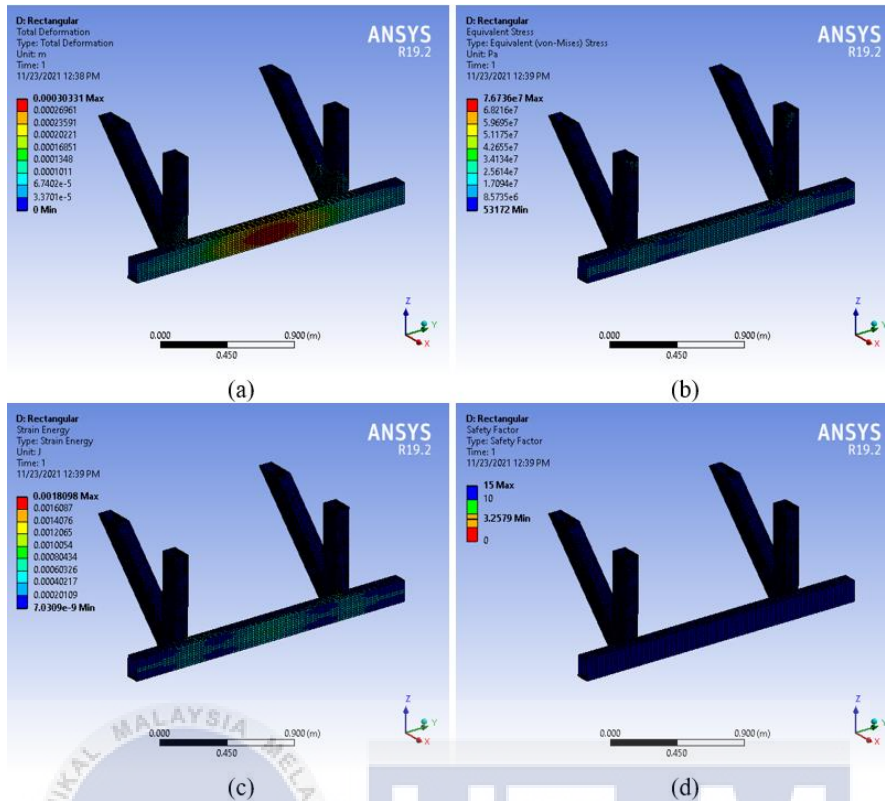


Figure 4.1. 74: P3 analysis angle of support structure using the rectangular hollow beam.

4.1.3.4 Square Hollow Beam of Support Structure

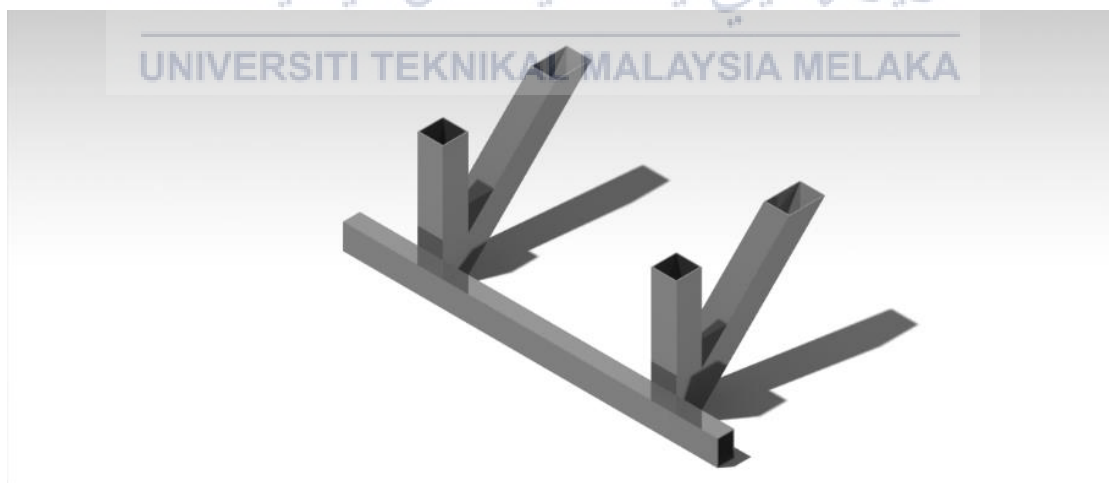


Figure 4.1. 75: Support structure using the square hollow beam.

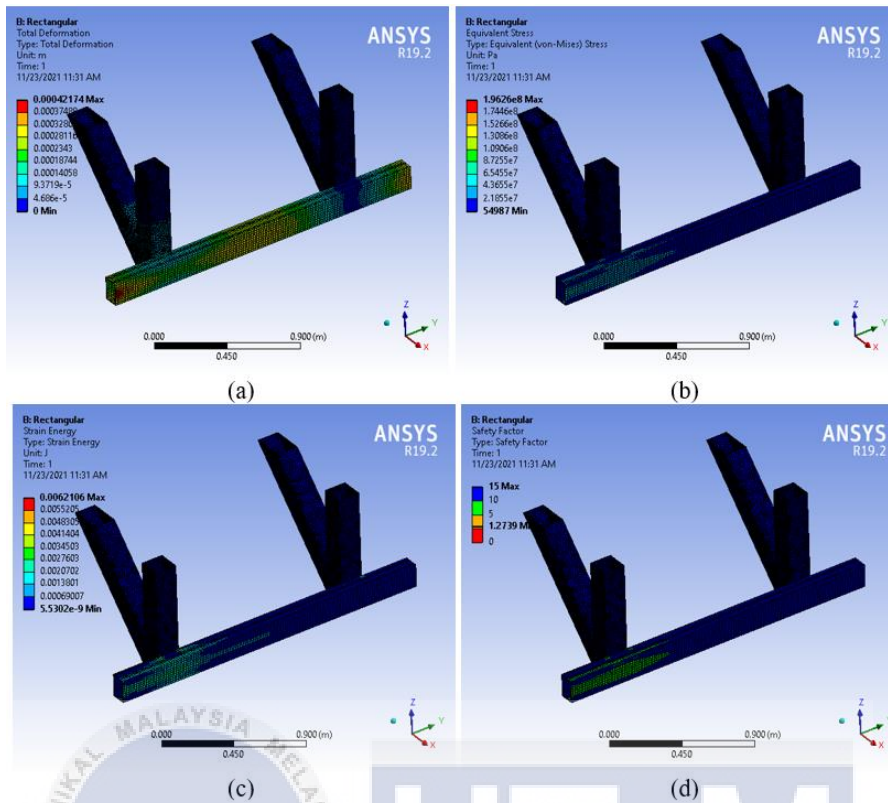


Figure 4.1. 76: P1 analysis angle of support structure using square hollow beam

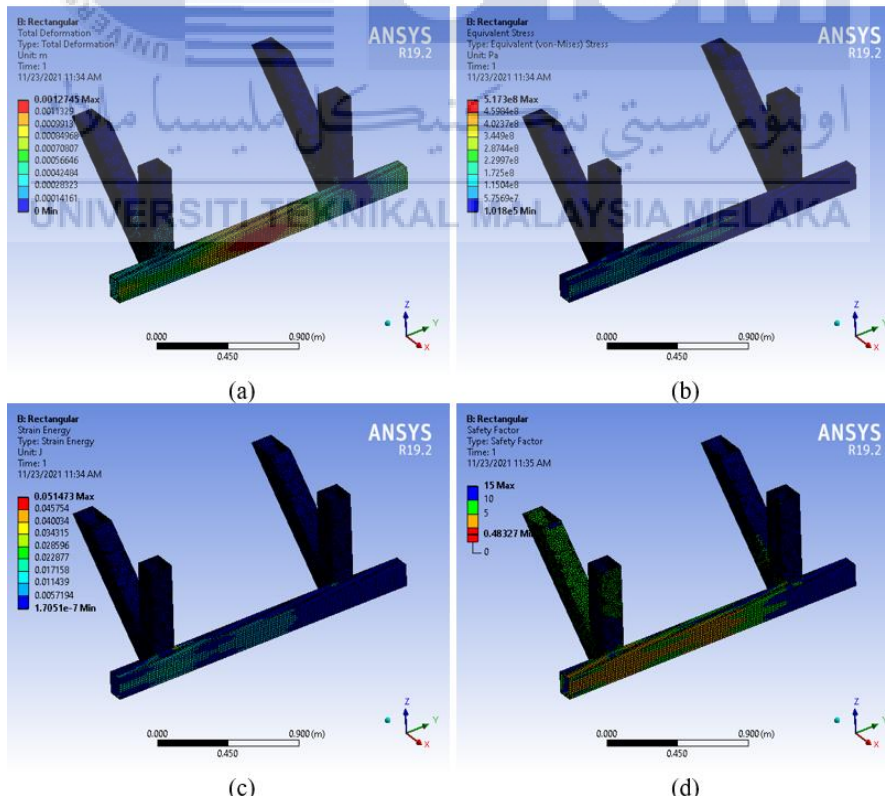


Figure 4.1. 77: P2 analysis angle of support structure using square hollow beam

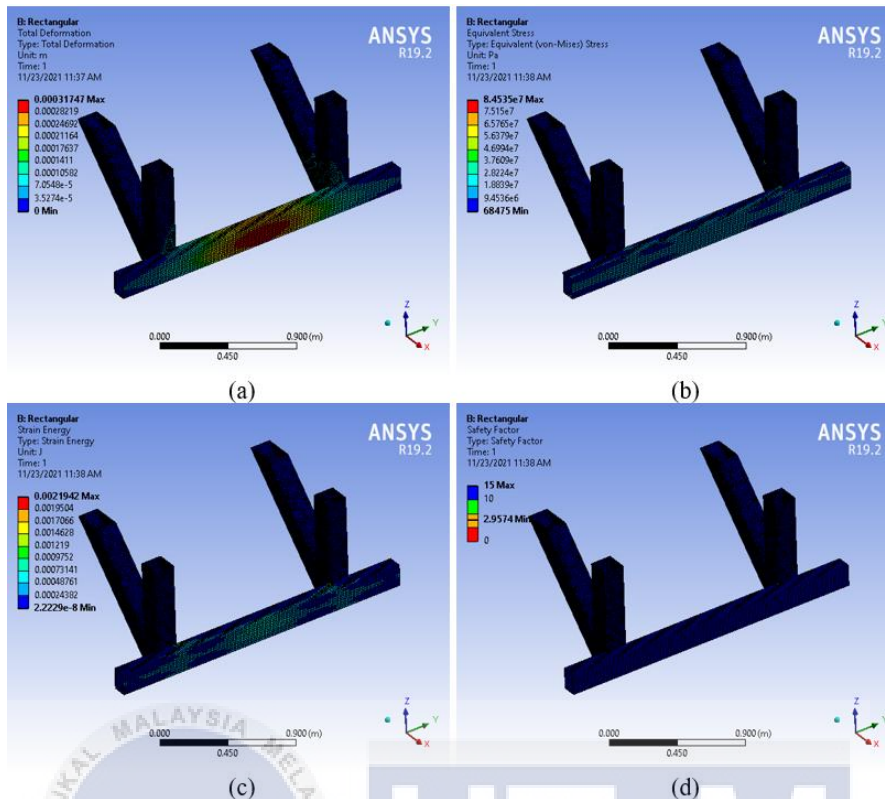


Figure 4.1. 78: P3 analysis angle of support structure using square hollow beam

4.1.3.5 Data Analysis Comparison for Type of Beam Used for RUPD

Table 4.1. 8: Comparison of total deformation type of beam used for RUPD

Force	Total Deformation			
	Circular	W-Beam	Rectangular	Square
P1	0.87124	0.54079	0.55962	0.42174
P2	2.6259	1.7271	1.2161	1.2745
P3	0.6489	0.43153	0.30331	0.31747

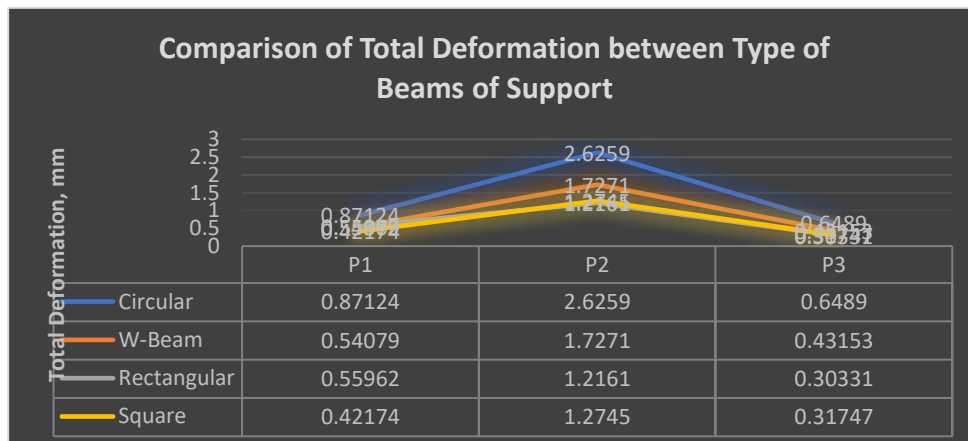


Figure 4.1. 79: Graph comparison of total deformation vs force for type of beam used for RUPD

Table 4.1. 9: Comparison data of maximum stress von Mises for the type of beam used for RUPD

Force	Maximum Stress Von Mises			
	Circular	W-Beam	Rectangular	Square
P1	3.03E+08	8.60E+07	1.38E+08	1.96E+08
P2	9.15E+08	2.59E+08	4.13E+08	5.17E+08
P3	1.79E+08	4.51E+07	7.67E+07	8.45E+07

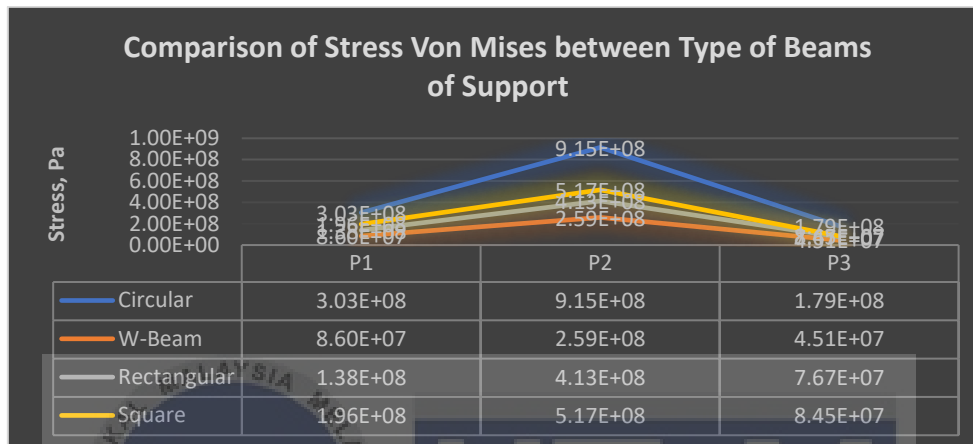


Figure 4.1. 80: Graph comparison of stress von Mises vs force for type of beam used for RUPD

Table 4.1. 10: Comparison data of strain energy for type of beam used for RUPD

Force	Strain Energy			
	Circular	W-Beam	Rectangular	Square
P1	0.03976	0.005194	0.0066665	0.0062106
P2	0.37444	0.045463	0.0474	0.051473
P3	0.015997	0.0012897	0.0018098	0.0021942

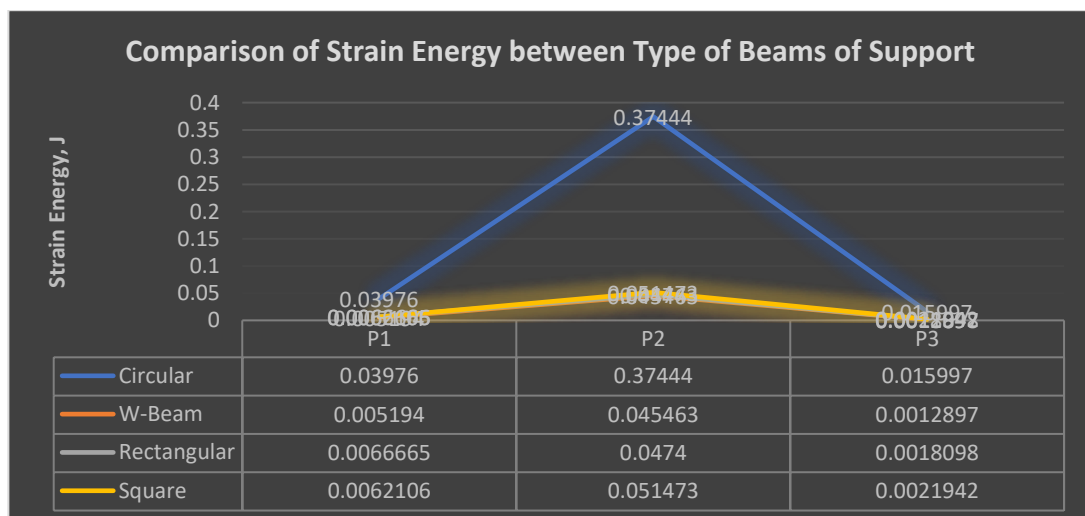


Figure 4.1. 81: Graph comparison of strain energy vs force for type of beam used for RUPD

This analysis examines which type of beam is better for the support structure. Based on the data above, a combination rectangular beam impact with circular beam support is the best design in receiving impact without exceeding the limitation of standard regulation. Thus, it chooses an angle of 45° of the support structure using a cylindrical hollow beam with a rectangular hollow beam as a beam impactor for support structure design.

4.2 Explicit Dynamic Analysis

This section will use explicit dynamics as a method of analysis in choosing the material for RUPD. This analysis will only use force impact of P2 with 0.2 s as the minimum time for the RUPD to hold the impact. So, the structure analysis will focus on point P3, whether it can receive impact without exceeding the standard deformation while absorbing at least 5630 J before it reaches 125 mm deformation.

4.2.1 Analysis Material of UPD

The material qualities of an exposed crashworthy element or system significantly impact its energy absorption capacity. The crashworthiness of a vehicle is highly dependent on the material. To save cost and minimise emissions, lighter materials are being developed to lower the weight of vehicles. Simultaneously, these lighter materials must ensure that the vehicle complies with applicable rules in terms of safety. As a result, this part will present an analysis of the UPD's materials. In this analysis part, the explicit dynamic will be applied in analysing the material used. Four types of material will be observed: Steel, aluminium, polyethylene, and magnesium.

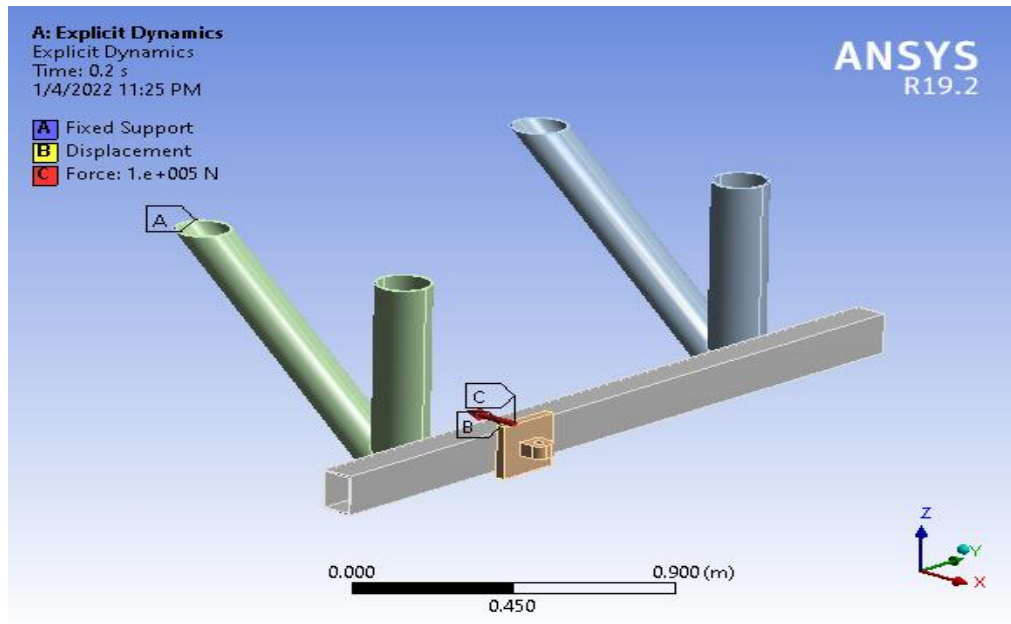


Figure 4.2. 1: Condition of RUPD for explicit dynamic analysis.



4.2.1.1 Steel

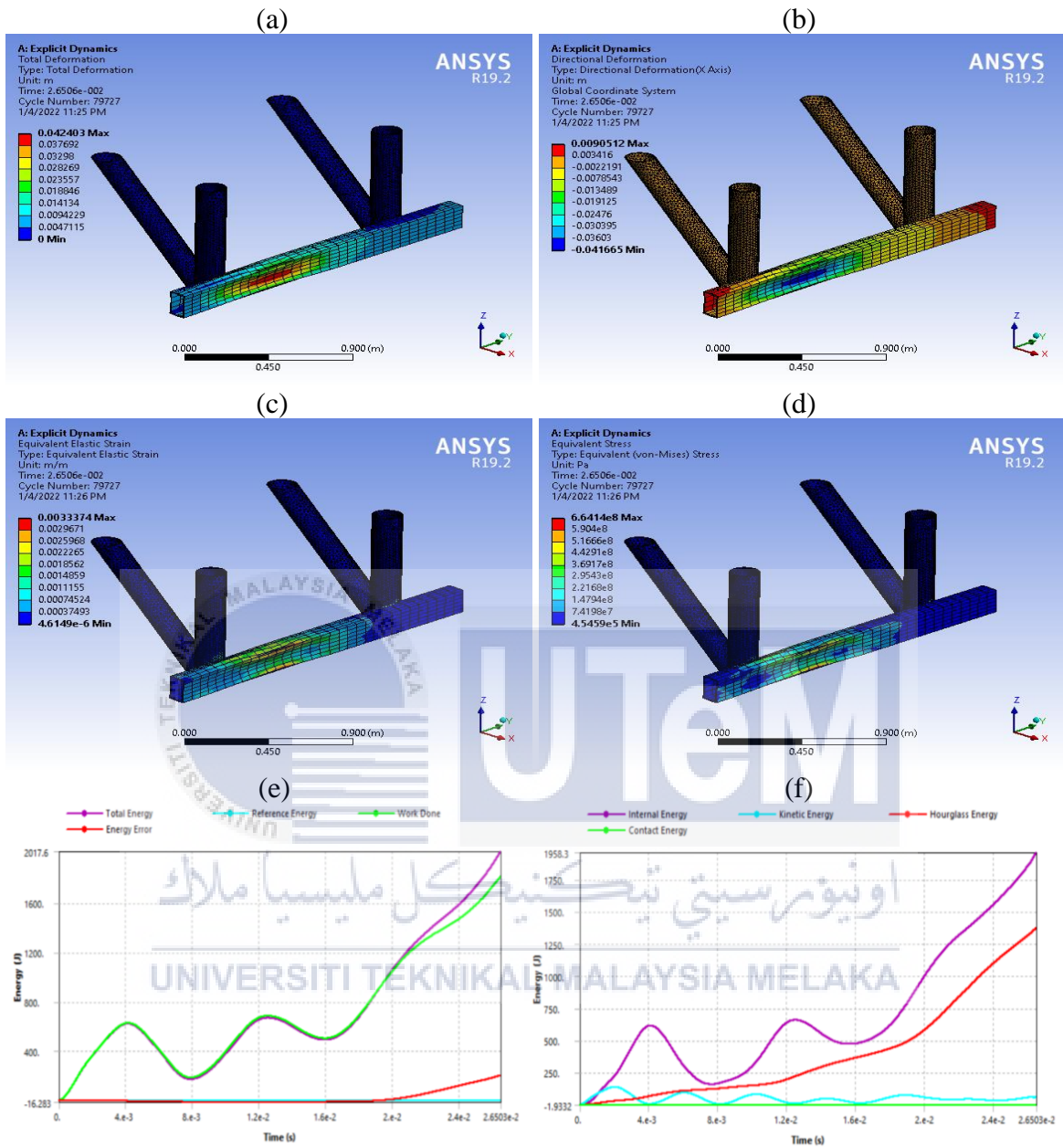


Figure 4.2. 2: Analysis results of RUPD for steel material (a) Total Deformation (b) Directional Deformation (c) Equivalent Elastic Strain (d) Equivalent Stress (e) Energy Conservation (f) Energy Summary

4.2.1.2 Aluminium

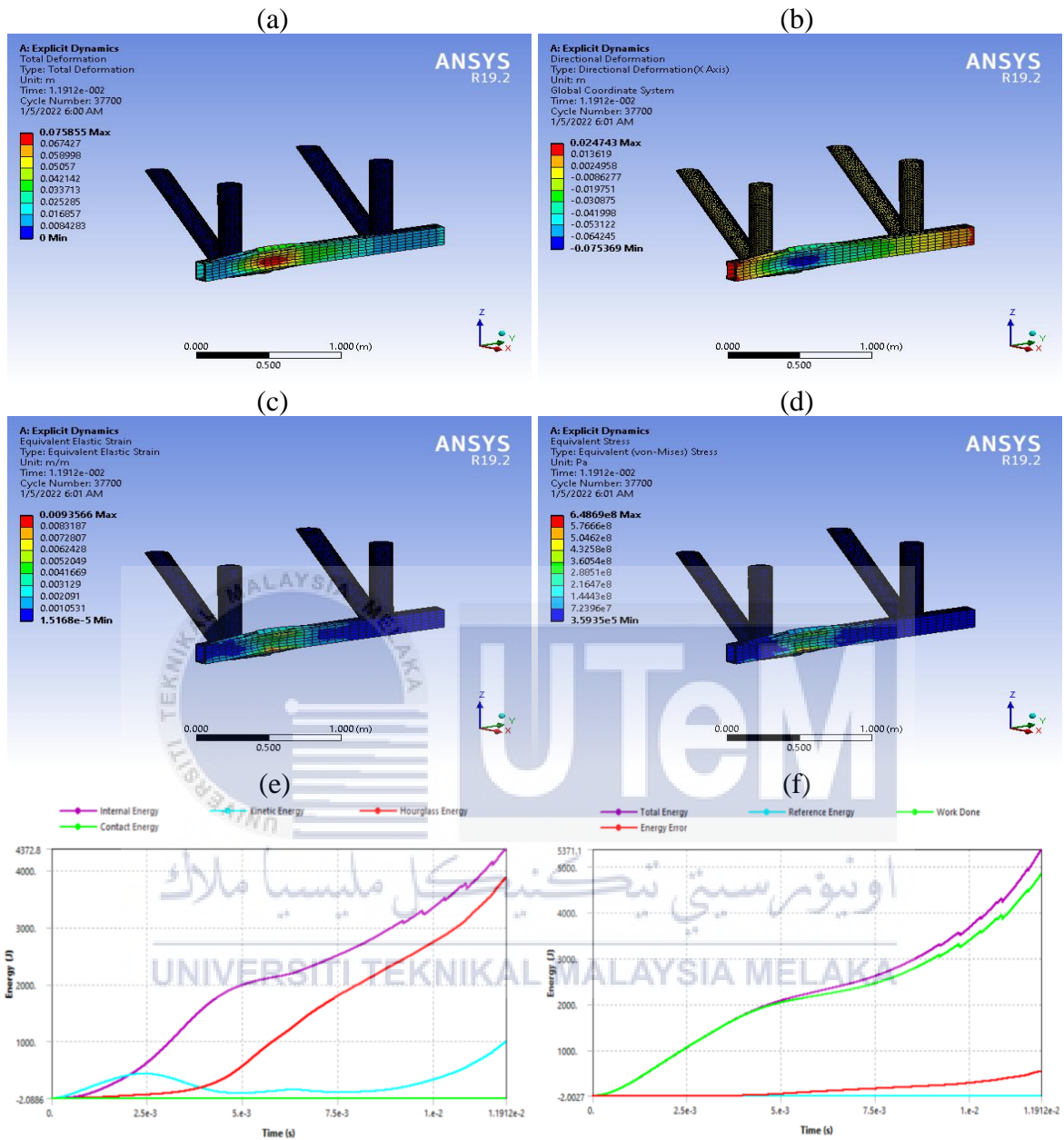


Figure 4.2. 3: Analysis results of RUPD for aluminium material (a) Total Deformation (b) Directional Deformation (c) Equivalent Elastic Strain (d) Equivalent Stress (e) Energy Conservation (f) Energy Summary

4.2.1.3 Magnesium

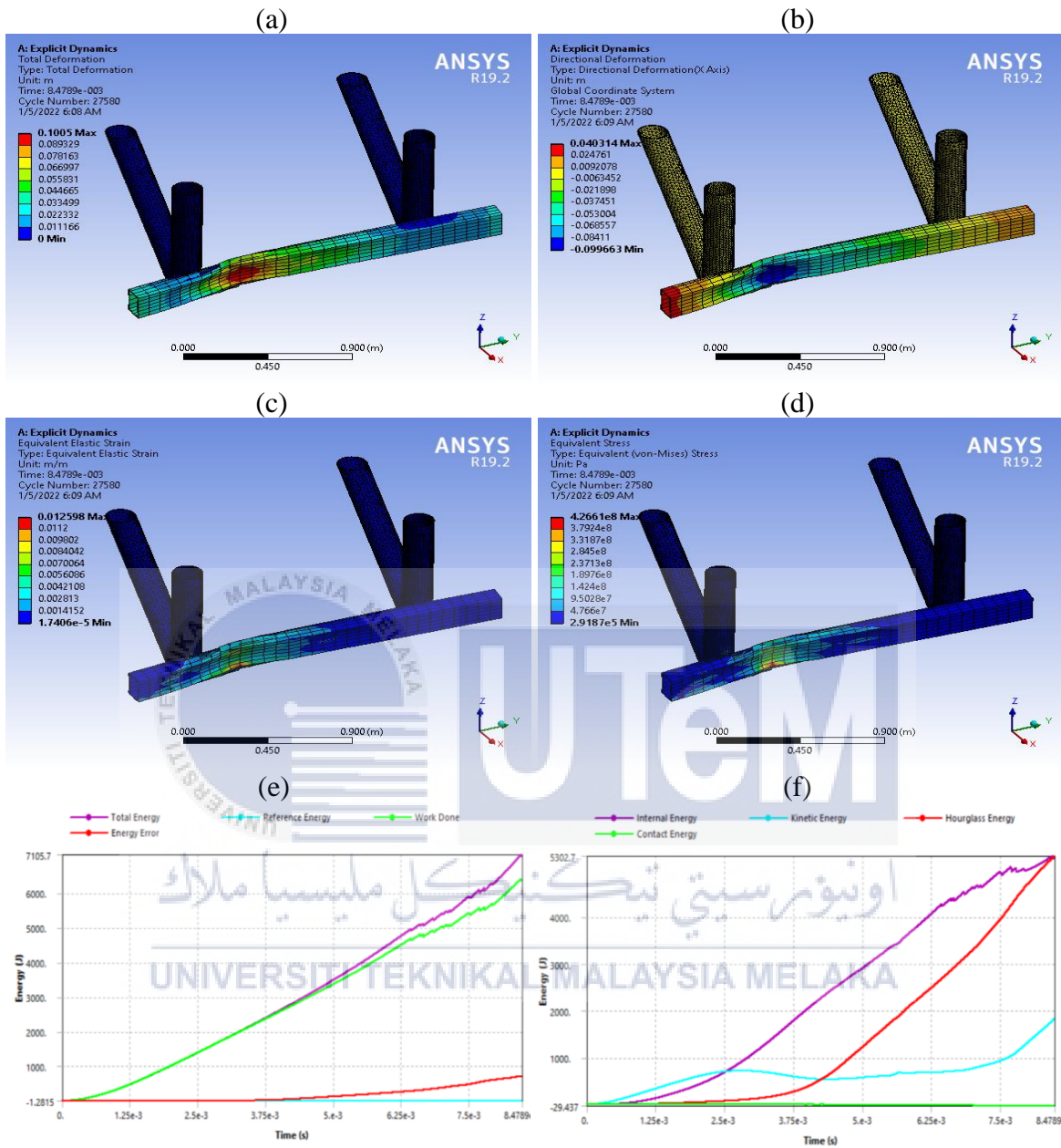


Figure 4.2. 4: Analysis results of RUPD for magnesium material (a) Total Deformation (b) Directional Deformation (c) Equivalent Elastic Strain (d) Equivalent Stress (e) Energy Conservation (f) Energy Summary

4.2.1.4 Polyethylene

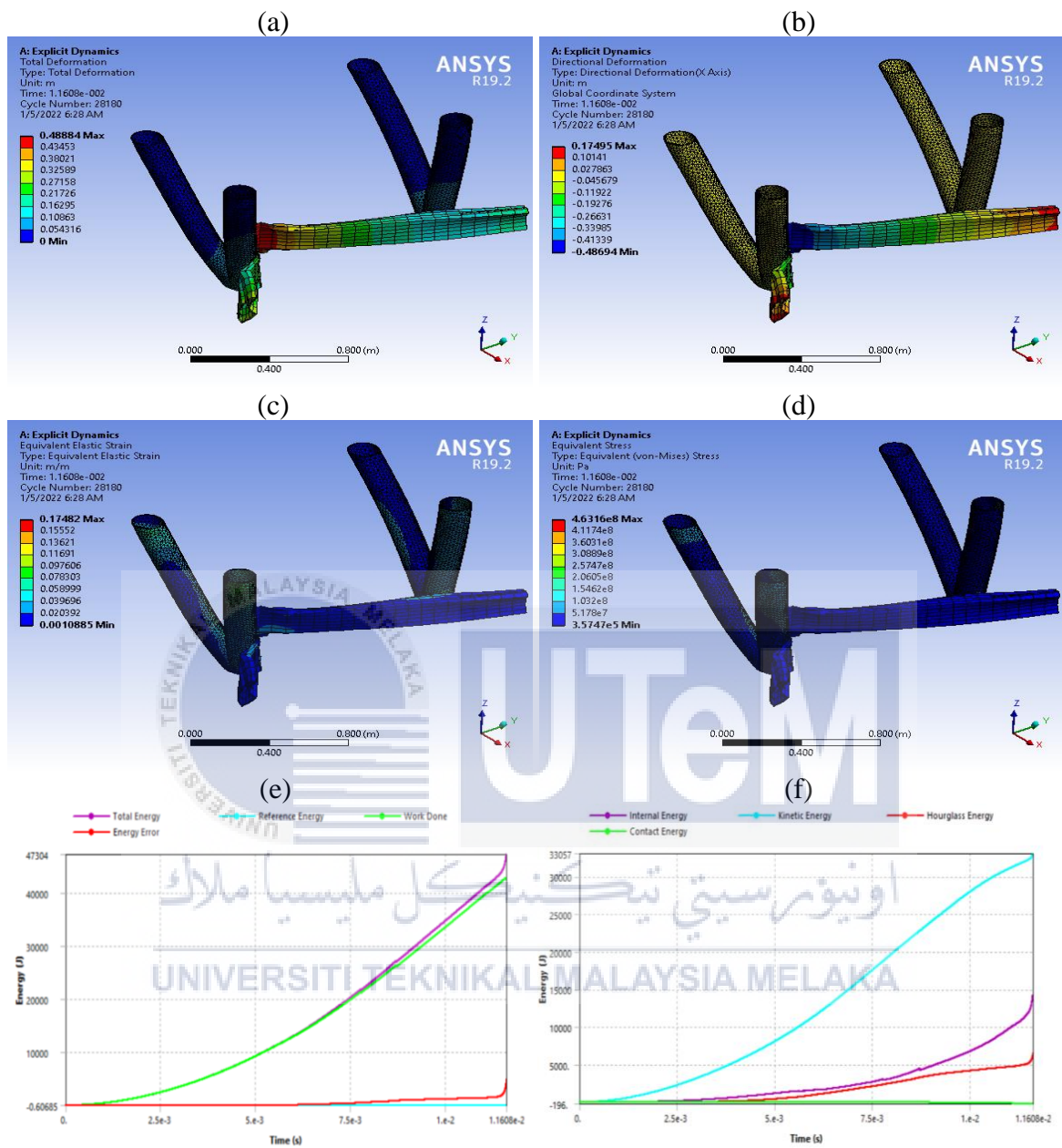


Figure 4.2. 5: Analysis results of RUPD for polyethylene material (a) Total Deformation (b) Directional Deformation (c) Equivalent Elastic Strain (d) Equivalent Stress (e) Energy Conservation (f) Energy Summary

4.2.2 Discussion on Material Analysis

For the material analysis, RUPD steel is the highest strength in terms of strength properties compared to aluminium, magnesium, and polyethene, which is the maximum stress of RUPD steel, aluminium alloy, magnesium alloy, and polyethene are 664 MPa, 648MPa, 426MPa and 463MPa respectively. The deformation is inverse with the material

stress, where the higher the stress, the lower the deformation. The material deformation does not exceed the standard of less than 125 mm except for material polyethene, 488.8 mm. The strain energy is also the same as internal energy, where the higher the strain energy of the material will have higher internal energy. The internal energy of Steel, aluminium, magnesium and polyethene is 2017 J, 5371 J, 33057 J, and 5302.7 J, respectively. At point 2 of impact, where the structure received 100kN from the impactor, the RUPD must absorb at less 5560 J before deforming 125mm. Thus, only material Steel did not acquire the standard of energy absorption, which only 2017 J. This analysis showed that the strength of material decreased with higher energy absorption.

4.3 Final Design

To summarise the result and discussion of this study, from the initial step until the final step, generate the final design for RUPD concerning the type of impact beam and support structure, angle of the support structure and the material of RUPD. For the type of impact beam, a rectangular hollow beam was chosen as the best impact beam with a support structure that used a circular hollow beam. While choosing 45 degrees as the angle of the support also increase the energy absorption of RUPD. Last, the material of RUPD showed that magnesium is the best material that absorbs impact from the crash. All the standard requirements in deformation and energy absorption have also been fulfilled for the final design.

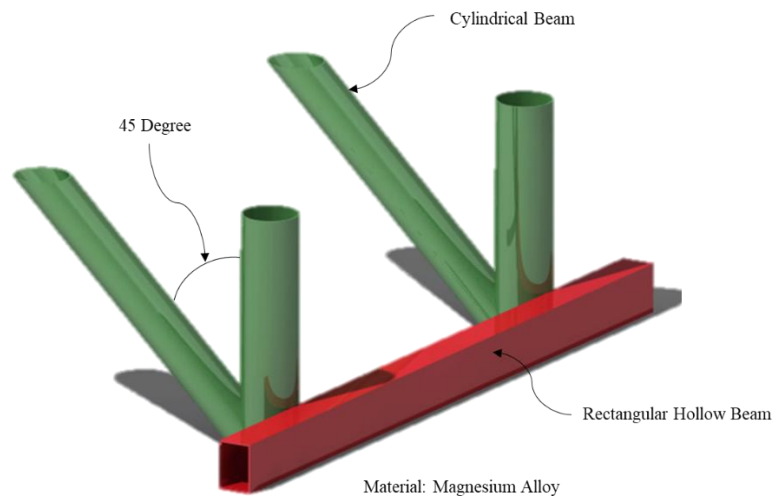


Figure 4.3. 1: Final Design of RUPD Structure



Figure 4.3. 2: Final Design of RUPD Structure on Lorry

CHAPTER 5

CONCLUSION AND RECOMMENDATION

5.1 Conclusion

RUPD assembly must conform with FMVSS 223 to satisfy the safety requirement for maintaining the underrunning of vehicles in many countries. This study aims to see how well a new RUPD on a large truck performs and if it conforms with the appropriate standards in the case of a collision with a car. This study analyses alternate designs of UPD guard bars intending to boost crashworthiness under impact to achieve the study's goal. During the simulation procedure, ANSYS software is utilised to analyse the performance. ANSYS is used to run the dynamic drop impact experiment using explicit dynamic. In addition, the guard was subjected to a quasi-static test to measure its strength and energy absorption capacity in the presence of applied forces.

The limited and boundary conditions in the research were all adequate. Two key design ideas guided the development of the Rear Underrun Protection Device: strength and energy absorption. The inquiry established the simulation approach and the modelling and analysis software parameters in great detail. It depicts how a basic RUPD design assembly absorbs energy and deforms under crush circumstances. The simulation results showed that RUPD designs meet FMVSS 223 requirements. The RUPD design with a rectangular hollow beam as the impact beam displayed improved energy absorption and displacement following the standard compared to the circular hollow beam, W-beam, and square hollow beam. The results show that the newly constructed RUPD can absorb a large amount of energy during

a collision. However, these results might be confirmed in the future via a real-world accident test.

The material utilised and the structural design are two essential factors influencing energy absorption during a collision and understanding the material's mechanical properties and failure during the impact. The construction of the RUPD was next examined using four different materials: Steel, aluminium, magnesium, and polyethene. According to the findings, magnesium outperforms other materials. The results were compared based on deformation, stress, and strain parameters. Magnesium is not subjected to the same stresses as other materials. As a result, this material's usage would help reduce crash impact, and it may also have a longer life than other materials due to its less severe damage. The energy-absorbing RUPDs would assist in reducing deaths caused by underrun cars and improve road safety. Additionally, the RUPDs would assist in avoiding damage to the heavier trucks as a result of such an underrun collision. The design presented in this article contributes to reducing impact force in accidental scenarios.

5.2 Recommendations

Experiments and appropriate production processes may be used to enhance this research. It is also possible to research the design and analysis of frontal underride safety measures for the frontal scenario. It is possible to design for weight loss. The research may be carried out using real moving and stationary vehicles, which is more realistic. For protection, more energy-absorbing models might be examined. A design technique based on RUPD design for a flexible range of load-carrying capability is required. Composites might be a promising future field for producing efficient RUPD. The optimising design also can be applied to the final design to produce the optimum design.

REFERENCES

- Abdul Manan, M. M., & Várhelyi, A. (2012). Motorcycle fatalities in Malaysia. *IATSS Research*, 36(1), 30–39. <https://doi.org/10.1016/j.iatssr.2012.02.005>
- Albahash, Z. F., & Ansari, M. N. M. (2017). A review on rear under-ride protection devices for trucks. *International Journal of Crashworthiness*, 22(1), 95–109. <https://doi.org/10.1080/13588265.2016.1228135>
- Allen, K. (2010). *The Effectiveness of Underride Guards for Heavy Trailers*. October.
- Atahan, A. O. (2007). A recommended specification for heavy vehicle rear underrun guards. *Accident Analysis and Prevention*, 39(4), 696–707. <https://doi.org/10.1016/j.aap.2006.10.016>
- Ayati, E., & Abbasi, E. (2011). Investigation on the role of traffic volume in accidents on urban highways. *Journal of Safety Research*, 42(3), 209–214. <https://doi.org/10.1016/j.jsr.2011.03.006>
- Berg, F. A., Rucker, P., Gartner, M., Konig, J., Grzebieta, R., & Zou, R. (2005). Motorcycle Impacts into Roadside Barriers – Real-World Accident Studies, Crash Tests and Simulations Carried Out in Germany and Australia. *Enhanced Safety of Vehicle*, 1–13.
- Biomechanics of Head-Neck Injuries In Heavy Truck Motor Vehicle Accidents*. (2006). 05, 2006.
- Björnstig, U., Björnstig, J., & Eriksson, A. (2008). Passenger car collision fatalities - with special emphasis on collisions with heavy vehicles. *Accident Analysis and Prevention*, 40(1), 158–166. <https://doi.org/10.1016/j.aap.2007.05.003>
- Bod, I. B., & Ip, O. P. S. (2011). *Patent Protection in Malaysia – a Basic Guide*. 691431, 1–47.
- Cebon, D. (1993). Interaction between heavy vehicles and roads. *SAE Technical Papers*. <https://doi.org/10.4271/930001>

Chen, C., & Tomizuka, M. (2010). *Vehicle System Dynamics : International Journal of Vehicle Mechanics and Mobility Lateral Control of Commercial Heavy Vehicles*. October 2014, 37–41. [https://doi.org/10.1076/0042-3114\(200006\)33](https://doi.org/10.1076/0042-3114(200006)33)

Dailidonis, D., & Griskevicius, P. (2010). *Crashworthiness Simulations of Side Underrun Protection Devices*. 2–5.

Dieter, G. E., & Schmidt, L. C. (2013). *Engineering Design 5th Edition* (Vol. 5).

Durand, E., Macpherson, J. M., Holmes, M. B., Llp, S., & Powers, M. A. (2016). (12) *United States Patent (45) Date of Patent : Primary Examiner*. 1(12).

Elvik, R. (2013). Risk of road accident associated with drugs: A systematic review and meta-analysis of evidence from epidemiological studies. *Accident Analysis and Prevention*, 60, 254–267. <https://doi.org/10.1016/j.aap.2012.06.017>

Evgenikos, P., Yannis, G., Folla, K., Bauer, R., MacHata, K., & Brandstaetter, C. (2016). Characteristics and Causes of Heavy Goods Vehicles and Buses Accidents in Europe. *Transportation Research Procedia*, 14, 2158–2167. <https://doi.org/10.1016/j.trpro.2016.05.231>

Galipeau-Bélaïr, P. (2014). *Design and Development of Side Underride Protection Devices (Supd) for Heavy Vehicles*. April.

Galipeau-Bélaïr, P., El-Gindy, M., Ghantae, S., Critchley, D., & Ramachandra, S. (2013). A review of side underride statistics and protection device literature and designs. *International Journal of Heavy Vehicle Systems*, 20(4), 361–374. <https://doi.org/10.1504/IJHVS.2013.056813>

Galipeau-Belair, P., Ghantae, S., Critchley, D., Ramachandra, S., & El-Gindy, M. (2014). Optimised rigid side underride protection device designs for tractor-trailers and straight trucks. *SAE Technical Papers*, 1. <https://doi.org/10.4271/2014-01-0565>

Goud, B. N., & Pachori, A. (2017). Investigation of Vehicle Rear Under Run Protection Device (RUPD) Using Aluminium Foam. *IOP Conference Series: Materials Science and Engineering*, 225(1). <https://doi.org/10.1088/1757-899X/225/1/012289>

Hamidun, R., Wah Hoong, A. P., Roslan, A., Shabadin, A., & Jamil, H. (2019). Characteristics of heavy goods vehicles (HGV) accidents in Malaysia. *IOP Conference Series: Materials Science and Engineering*, 512(1). <https://doi.org/10.1088/1757-899X/512/1/012021>

Iqbal, J., & Quadri, S. M. K. (2011). Software Reliability Simulation: Process, Approaches and Methodology. *Global Journal of Computer Science and Technology*, 11(8).

Jacobs, G., & Astrop, A. (1999). *Estimating global road fatalities*. December.

Joseph, G., Shinde, D., & Patil, G. (2013). Design and Optimisation of the Rear Under-Run Protection Device Using LS-DYNA. *International Journal Of Engineering Research And Applications*, 3(4), 152–162.

Joshi, K., Jadhav, T. A., & Joshi, A. (2012). Finite Element Analysis of Rear Under-Run Protection Device (RUPD) for Impact Loading. *International Journal of Engineering Research and Development*, 1(7), 19–26. www.ijerd.com

Kaygisiz, Ö., Yildiz, A., & Düzgün, Ş. (2015). Spatio-temporal pedestrian accident analysis to improve urban pedestrian safety: The case of the eskişehir motorway. *Gazi University Journal of Science*, 28(4), 623–630.

Knight, I., & Report, U. P. (n.d.). *Review of side and underrun guard regulations and exemptions by T L Smith and I Knight UNPUBLISHED PROJECT REPORT by T L Smith and I Knight (TRL Limited) Prepared for Project Record :*

Kual, A., Sinha, U. S., Pathak, Y. K., Singh, A., Kapoor, A. K., Sharma, S., & Singh, S. (2005). Fatal road traffic accidents, a study of distribution, nature and type of injury. *Journal of Indian Academy of Forensic Medicine*, 27(2), 71–76.

<http://www.indianjournals.com/ijor.aspx?target=ijor:jiafm&volume=27&issue=2&article=001>

Kumar, B. P., & Kumar, P. P. (2017). Design and Structural Analysis of Truck Rear Under Run Protection Device with Rapid Prototype. *International Journal & Magazine of Engineering, Technology, Management & Research*, 4(6), 124–129.

Lambert, J., & Rechnitzer, G. (2002). *REVIEW OF TRUCK SAFETY: STAGE 1: FRONTAL, SIDE AND REAR UNDERRUN PROTECTION*. 194.

Liu, H. F., Tao, P., Xu, H. G., Tan, L. D., & Su, L. L. (2010). Research on the intelligent rear under-run protection system for trucks. *Proceedings of the World Congress on Intelligent Control and Automation (WCICA)*, 5274–5278.

<https://doi.org/10.1109/WCICA.2010.5554843>

MacDonald, T., El-Gindy, M., Ghantae, S., Ramachandra, S., & Critchley, D. (2013). Rigid front underride protection device (FUPD): Compatibility and development via optimisation. *Proceedings of the ASME Design Engineering Technical Conference*, 1, 1–11.
<https://doi.org/10.1115/DETC2013-12009>

Mattos, G., Friedman, K., Kiefer, A., & Ponder, P. (2021). Protecting Passenger Vehicles from Side Underride with Heavy Trucks. *SAE Technical Paper Series*, 1, 1–12.
<https://doi.org/10.4271/2021-01-0288>

Mi, A. J. P. (2000). *Development of Active Anti-Roll Control for Heavy Vehicles*.

Mohammed, A. A., Ambak, K., Mosa, A. M., & Syamsunur, D. (2019). A Review of the Traffic Accidents and Related Practices Worldwide. *The Open Transportation Journal*, 13(1), 65–83. <https://doi.org/10.2174/1874447801913010065>

Mohod, R. P. (2017). Crashing Analysis of Rear Under Run Protection Device (RUPD). *International Journal of Emerging Technologies in Engineering Research (IJETER)*, 4(6), 8–12.

Mohod, R. P., Joseph, G., Shinde, D., & Patil, G. (2017). Design and Optimisation of the Rear Under-Run Protection Device Using LS-DYNA. *International Journal Of Engineering Research And Applications*, 4(4), 152–162.

Odero, W., Garner, P., & Zwi, A. (1997). *Road traffic injuries in developing countries : a comprehensive review of epidemiological studies*. 1997(5), 445–460.

Pachocki, L., Bruski, D., Burzyński, S., Chróscielewski, J., Wilde, K., & Witkowski, W. (2018). On the influence of the acceleration recording time on the calculation of impact severity indexes. *MATEC Web of Conferences*, 219, 0–7.

<https://doi.org/10.1051/mateconf/201821903010>

Pooudom, S., Chanthanumataporn, S., Koetnियom, S., & Carmai, J. (2019). Design and Development of Truck Rear Underrun Protection Device. *IOP Conference Series: Materials Science and Engineering*, 501(1).

<https://doi.org/10.1088/1757-899X/501/1/012017>

PROTECTION PROTECTIONS • Quick Action Triple position settings. (n.d.). 3950.

Raftery, S. J., Grigo, J. A. L., & Woolley, J. E. (2011). *Heavy vehicle road safety : Research scan Report documentation*. July.

UNIVERSITI TEKNIKAL MALAYSIA MELAKA
REAR AND SIDE UNDERCARRIAGE SAFETY BARS FOR MALAYSIA HEAVY VEHICLES 2016 UTeM. (n.d.).

Series, I. O. P. C., & Science, M. (2018). *Design and development of rear underride protection device (RUPD) with improved energy absorption using ANSYS Design and development of rear underride protection device (RUPD) with improved energy absorption using ANSYS*. <https://doi.org/10.1088/1757-899X/402/1/012169>

States, U., & Accountability, G. (2019). *TRUCK UNDERRIDE GUARDS Improved Data Collection, Inspections, and Research Needed*. March.

THE INJURY CHART BOOK A graphical overview of the global burden of injuries
Department of Injuries and Violence Prevention Noncommunicable Diseases and Mental
Health Cluster World Health Organization. (2002).

Thongtip, T. (2020). *Crashworthiness Investigation of Multi-stage Structures Designed for
Underrun Protection Devices*. 1–10. <https://doi.org/10.14416/j.asep.2020.10.003>

United Nations Regulations. (2017). *Addendum 78: UN Regulation 79. 1958(November)*, 1–
40.

Vivoli, R., Bergomi, M., Rovesti, S., Bussetti, P., & Guaitoli, G. M. (2006). Biological and
behavioural factors are affecting driving safety. *Journal of Preventive Medicine and
Hygiene*, 47(2), 69–73. <https://doi.org/10.15167/2421-4248/jpmh2006.47.2.47>



APPENDICES

Appendix A: Details Drawing of Final Design of RUPD

